Comparative study of neural network-based models for fatigue crack growth predictions of small cracks

Sara Himmiche

A Thesis
In
the Department
of
Mechanical Engineering

Presented in Partial Fulfillment of the Requirements
for the Degree of Master of Applied Science at
Concordia University

Montreal, Quebec, Canada

December 2020

CONCORDIA UNIVERSITY

School of Graduate Studies

This is to certify that the thesis prepared

By: Sara Himmiche

Entitled: Comparative study of neural network-based models for fatigue crack growth predictions of small cracks

And submitted in partial fulfillment of the requirements for the degree of

Master of Applied Science

complies with the regulations of the University and meets the accepted standards with respect to originality and quality. Signed by the final Examining Committee:

_____ Chair

Ion Stiharu

_____Examiner

James C. Newman, Jr.

_____Examiner

Biao Li

_____ Supervisor

Ayhan Ince

Approved by _____

Martin D. Pugh

_____2020 _____

Mourad Debbabi

ABSTRACT

Comparative study of neural network-based models for fatigue crack growth predictions of small cracks

Sara Himmiche

The behavior of small cracks (less than 1 mm in length) have been shown to be quite different than large cracks for a variety of materials. In the past two decades, the large-crack test procedure (load shedding) has been shown to cause a load-history effect in the low-rate regime, generating elevated thresholds, and slower rates than steady-state behavior, which caused a large part of these differences. The literature has shown that small-crack data is more appropriate for damage tolerance and fatigue analyses. The objective of this work was to validate the development of artificial neural network (ANN) methods in fatigue crack growth predictions of small cracks. Two ANNs were developed: extreme learning machine (ELM) and radial basis function network (RBFN) to predict fatigue crack growth of small cracks for various materials. A wide range in stress ratio R and stress levels were considered for selected materials. The two ANNs were compared with each other in terms of mean squared error achieved and performance. The ELM method showed a superior interpolation and extrapolation ability compared to the RBFN method.

DEDICATION

The author devotes this study to her family members in Morocco, and her friends. This thesis is the fruit of continuous support, love and encouragement throughout the years. The author also dedicates this work to her supervisor, Ayhan Ince, who helped her reach her objective to obtain a Master's degree in Mechanical Engineering from Concordia University through constant support.

ACKNOWLEDGEMENTS

The author wishes to express gratefulness to her supervisor, Ayhan Ince for his continuous engagement throughout the progress of this thesis. Furthermore, the author expresses her sincere gratitude to Professor James C. Newman, Jr. for providing helpful resources and data from his previous works. Special thanks go to everyone from the Mechanical Engineering Department in Concordia University, who helped accomplish this work. Huge indebtedness goes to the author's parents, uncle, and her beloved sisters and brothers: Ghania Karbal, Abdesalam Himmiche, Ahmed Himmiche, Imane Himmiche, Latifa Himmiche, Karim Himmiche and Saad Himmiche, for always putting their trust in her, encouraging her and loving her for who she is. Lastly, sincere appreciation is given to the committee members: James C. Newman, Jr., Dr. I. Stiharu, and Dr. Biao Li, who have put the time and effort into reviewing this thesis.

TABLE OF CONTENTS

LIST OF TABLES

LIST OF FIGURES

NOMENCLATURE

ANN	Artificial neural network
AGARD	Advisory Group for Aerospace Research and Development
a	Small surface-crack depth
B	Specimen thickness
b	Fatigue strength exponent
c	Surface crack half-length
da/dN	Fatigue crack growth rate
E	Modulus of elasticity
ELM	Extreme learning machine
EPFM	Elastic-plastic fracture mechanics
FBNN	Feed backward neural networks
FCG	Fatigue crack growth
FEM	Finite element method
FFNN	Feedforward neural networks
LEFM	Linear elastic fracture mechanics
l_o	El Haddad's correction term
MSE	Mean squared error
NN	Neural network
n_n	Number of neurons
PDF	Probability density functions
R	Stress ratio
RBF-NN	Radial basis neural network function

SENT	Single-edge-notch-tension
SLFN	Single-hidden layer feed-forward neural network
S_{max}	Maximum applied stress level
S_{min}	Minimum applied stress level
S_O	Crack-opening stress
U	Elber parameter
W	Specimen width
ΔK	Stress intensity range ΔK
ΔK_{eff}	Effective stress intensity range
ΔS	Stress range
σ_f'	Fatigue strength coefficient
σ_u	Ultimate tensile strength
σ_{ys}	Tensile yield strength

CHAPTER I

INTRODUCTION

Predicting fatigue life of components and structures used in critical applications is a serious challenge. The presence of cracks can significantly reduce the lifetime and reliable predictive models of lifetime estimations are a necessity to prevent fatigue failures. The problem of aging civil infrastructure and aircraft have been the subject of research for many years [1],[2]. The damage tolerance approach founded on the principles of fracture mechanics is based on the assumption that flaws are pre-existing in structures [3]. A continuous maintenance program is implemented to estimate the initial size of the existing crack. This approach has been adopted by the nuclear and aerospace industries and crack growth models based on the damage tolerance of a structure results in considerably successful fatigue life predictions [4]–[6]. Continuous research and different approaches are needed for safety critical structures during the design phase. The accurate predictions of fatigue crack growth rates necessitate starting from the initiation phase to the final fracture phase since those pre-existing defects are implicit in engineering components and most importantly a significant fraction of a component lifetime is spent during crack initiation (i.e., before the smallest crack is obtained from a reliable non-destructive evaluation (NDE) technique).

Researchers have shown the importance of small cracks in fatigue analysis [7]. These small cracks initiating from micro defects (i.e., voids) are critical since a big portion

of the fatigue life is spent at that stage as can be seen in Figure 1. Detecting these small cracks (smaller than the non-destructive inspection (NDI) limit) can be a serious issue while predicting the life of a component.

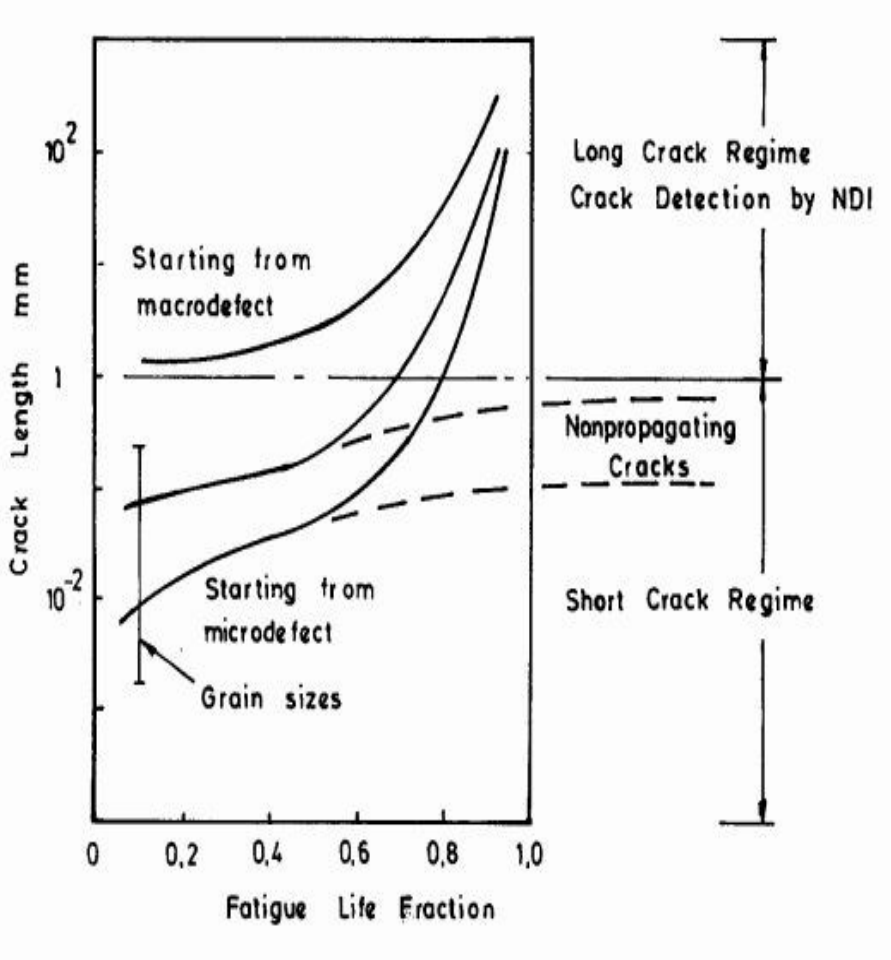

Figure 1 Illustration showing that a large portion of the fatigue life is spent while the crack is smaller than the NDI limit [7]

Linear elastic fracture mechanics (LEFM) approaches can be applied for damage tolerance, fatigue durability analyses [8], and for long cracks. In fact, design using LEFM for long cracks (of size greater than 1 mm) based in similitude concept. This latter concept states that cracks with the same crack tip conditions propagate at the same rate. This method

usually delivers good fatigue life predictions. Numerous researchers reviewing the behavior of crack growth have pointed out that small cracks propagate anomalously faster than corresponding long cracks under identical nominal driving force, as illustrated in Figure 2 [3], [8]–[11]. When LEFM is extended to small cracks behavior study, non-conservative estimates (over predictions) of components lifetime result. The propagation rate of small cracks deviates from long crack ones and exhibits large scatter [12]. Hence, LEFM based on similitude concepts do not properly address the abnormal behavior of small cracks [13]–[15]. These findings are especially important for safety reasons when designing components where fatigue life is mainly dominated by small crack growth.

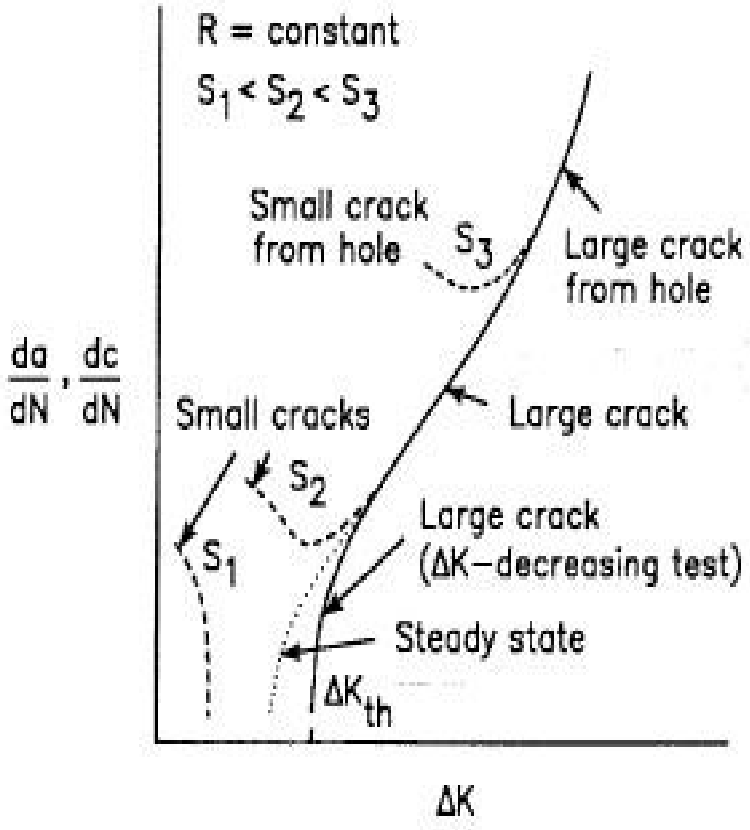

Figure 2 Characteristic fatigue crack growth (FCG) rate data for small and large cracks under constant amplitude loading [16]

According to Ritchie and Lankford [17] and Ritchie and Suresh [3], small cracks can be categorized into:

(i) Microstructurally-small cracks: cracks with length less or equal to the microstructural scale, usually between 1 and 50 μm.

(ii) Mechanically-small cracks: cracks with length less or equal to the local plasticity zone scale, usually between 0.01 to 1 mm.

(iii) Physically-small cracks: cracks with length less or equal to that at which crack closure is entirely developed, usually between 0.5 and 1 mm.

To analyze and explain small fatigue crack growth behavior, non-linear fracture mechanics methods such as notch plasticity and crack closure have been proposed. In a study to determine the significance of fatigue crack closure, Elber [18] introduced the plasticity induced crack closure concept and developed the effective stress intensity range (ΔK_{eff}) approach. His approach states that the fatigue crack growth rate *da/dN* is strongly related to the effective stress intensity factor range. Elber [18] used the crack closure approach to explain the stress-ratio (R) effects on crack growth. He related the linear-elastic stress-intensity factor range (ΔK) to the effective stress intensity range using the parameter U. U is the ratio of the effective stress range (S_{max}-S_o) to the full stress range (S_{max}-S_{min}) where S_o is the crack-opening stress. Consequently, the effective stress intensity range (ΔK_{eff}) is computed to account for the effect of the closure on advancing cracks from these LEFM equations [16]. The closure behavior is induced by residual plastic deformation caused by an advancing crack (i.e., plasticity-induced crack closure)[18]. The crack closure behavior may also occur due to surface roughness (i.e., roughness-induced crack closure) and oxide debris (i.e., debris-induced crack closure) [16],[19]. Today, some existing finite

element software packages used to predict the lives of structures only account for plasticity-induced crack closure in an inert environment, whereas roughness or oxide induced crack closure are the major source of crack-shielding mechanisms [20][21].

While the lack of similitude between small cracks and long cracks, many studies used the crack closure effect regardless to explain the small-crack effect [9], [22]–[24]. Small cracks aren't necessarily closed during the loading cycle as much a larger crack is, such is the case for cracks initiating from voids for example. Additionally, the plasticity in the wake of a rising crack is not fully developed for inducing crack closure. Lindley and Richards [25] established that as for pure plane strain conditions, crack closure is not of great importance in fatigue crack growth. Yet, fatigue failure generally initiates at the free surface of a body where the material is under "plane stress" conditions where crack closure is very dominant [6]. For years, researchers have successfully predicted small crack growth under constant-amplitude and spectrum loading using crack-closure theory [6]. Regardless of many studies supporting the crack closure concept, there are several studies [10], [26]–[28] that expressed uncertainties on whether this concept can explain the abnormal behavior of small cracks. Small cracks have a transient period to stabilize the crack-opening stress, but the main issue is that the test methods for "large" cracks has been flawed, i.e., test method (load shedding) induces a load-history effect [6].

El Haddad et al. [29] explained the small crack behavior by the J integral concept. He modified elastic-plastic fracture mechanics (EPFM) existing solutions to include the J integral and the intensity factors to estimate the fatigue crack growth rate of small cracks. For that purpose, he introduced an effective crack length to EPFM solutions (equal to the crack length added to a correction term l_o) to correlate small crack data to

long crack ones. EL Haddad's correction term, l_o, is yet unknown for cracks originating from smooth surfaces. According to McEvily [30], previous researches have shown that the use of elastic-plastic J-integral range, ΔJ, as a correlating parameter between small cracks and long cracks results in more scatter in the S/N curve of aluminum alloys.

Numerous attempts in apprehending and modeling the small crack behavior have been proposed to account for the growth of small fatigue cracks [31], [32]. These models have been used by the US Air Force and aerospace industries to design safe aircraft or structures for many decades. According to Newman [6], improvements need to be made in the generation of crack growth data (da/dN) in the very low propagation rate of large and small crack regimes. In the past two decades, a large amount of the "large" crack test data has been shown to be flawed, due to a load-history effect caused by the load-shedding test method [33][24]. Thus, the large-crack data in the low-rate regime is the anomaly, and more small-crack data should be generated for a variety of materials and environments.

Artificial neural network (ANN) is a system inspired by the biological neural system [34] which is widely used because of its fast-adaptive learning of complex data. The machine learning approach established on ANN methods were shown by previous studies to address the nonlinearities of crack growth behavior of long cracks [35].

Machine learning methods based on ANN were established to be one of the most effective predictive modeling approaches for predicting mechanical properties, fatigue behaviors, and effects of environmental factors on materials because of their tremendous flexibility and ability of classification and prediction [35],[36]. Fahad et al. [37] proposed using Radial Basis Function Neural Network (RBF-NN) as an efficient and low-cost method to detect corrosion of commercial pipes. Mohanty et al. [38] developed a subset of

machine learning called genetic programming (GP) to predict fatigue crack growth of large cracks for 2024-T3 aluminum alloy under various loading conditions. The authors then compared the results with a previously proposed ANN model. The authors showed that GP and ANN can successfully predict the long fatigue crack growth rate for 2024-T3 aluminum alloy. Zhang et al. [39] employed RBF-NN to model the fatigue crack growth for various aluminum alloys. Their results showed good agreements with experimental data for different materials: Al7075-T6, Al2024-T315, and D16 Aluminum alloy. Wang et al. [40] presented a paper that compared three different ANNs for fatigue crack growth calculation. RBF-NN, Extreme Learning Machine (ELM), and Genetic Algorithm optimized Back Propagation algorithms (GABP) were used for predicting fatigue crack growth for 2024-T351, 6013-T65, 7050-T745, D16 aluminum alloys as well as for Ti6Al4V titanium alloy and ADB610 steel. The results were compared to each other and to the classical K* approach. The classical K* approach is an alternative of the effective stress intensity factor ΔK_{eff} in Elber's model and has been known to be superior to other analytical formulas. The classical K* parameter correlates R ratio to the fatigue crack growth rate, da/dN and is able to describe the three regions in Paris curve with no limitation on *R* ratio [40]. According to Wang et al. [40] results, the three MLA's algorithms were more accurate than K* approach for predicting the fatigue crack growth of long cracks. The best mean squared error (MSE) achieved was with ELM. Bin Younis et al. [41] used RBF-NN technique to predict fatigue crack growth rate in different aircraft aluminum alloys including 2324-T39, 6014-T651, and 7075-T7511. Their results agreed with the experimental data. Moratazavi and Ince [42] predicted the FCG behavior of small and large cracks for three different alloys (2024-T3 aluminum alloy, 7075-T6 aluminum alloy, and

Ti-6Al-4V titanium alloy) using an RBFNN model. The authors validated the interpolation ability of RBFNN for both crack growth regimes. Their study showed poor extrapolation ability of RBFNN in terms of predicting small crack growth.

The behavior of long cracks is therefore well described by ANN. Small cracks, on the other hand, exhibit more complex behavior and scatter due to microstructural features, specimen geometry, and load history. The question is: Can the short or small fatigue crack behavior be predicted using these machine-learning algorithms?

ANN techniques were utilized in this work to predict fatigue crack growth of small cracks for various materials. Data-driven methods such as machine learning based on ANN can find relationships between the system input(s) and output(s) with little knowledge of the systems' behavior. ANNs based methods were proposed in this work to address the complex nature of small cracks by detecting relevant relationships.

Five materials widely used in the aerospace industry were chosen for this work because their small crack data sets were available. 2024-T3, 7075-T6, 2090-TBE41, LC9cs aluminum and Ti-6Al-4V titanium alloys were used to assert the importance of using ANN in addressing complex behavior of crack propagation. Experimental data from various stress levels in the small crack regime were retrieved from previous research works.

Since safety is one of the most critical factors in the aerospace industry, engineers must perform accurate fatigue and fracture analysis to prevent any risk of structural failure. This work delivers, therefore, a thorough study on the behavior of small cracks for different materials: 2024-T3 [9], 7075-T6 [43][8], 2090-TBE41[43], LC9cs aluminum [8] and Ti-6Al-4V titanium[43][32] alloys under various loading conditions, and evaluates the use of

two ANN algorithms: RBFN and ELM for predicting and correlating fatigue crack growth of small cracks.

CHAPTER II

EXPERIMENTAL FATIGUE CRACK GROWTH DATA

Small-crack test data from five materials: 2024-T3 [9], 7075-T6 [43][8], 2090-TBE41[43], LC9cs aluminum [8] and Ti-6Al-4V titanium [43][32] alloys were used to train the ANNs.

2024-T3 aluminum alloy sheet (2.3 mm thick) and Ti-6Al-4V titanium alloy sheet (1.5 mm thick) and 2090-TBE41 aluminum-lithium alloy sheet (2.15 mm thick) were used in AGARD R-732 [9] to generate small fatigue crack growth data on single-edge-notch-tension (SENT) specimens at room temperature under different constant amplitude loading conditions with stress ratios varying from R= -2 to R= 0.5. The large negative stress ratios were used because the small crack behavior is more prominent under compressive loading conditions [9]. At each R ratio, several stress levels were applied. To measure the crack growth of small cracks, a non-destructive method called “plastic-replica” that allows the examination of the microstructure of materials and crack detection was used at the notch root.

7075-T6 aluminum alloy and LC9cs clad (2 mm thick) sheets were used in the Advisory Group for Aerospace Research and Development (AGAD) report R-767 [43] and NASA RP-1309 [8] to study crack growth of small cracks. Fatigue testing was performed on SENT specimens at room temperature under constant amplitude loading (R= -1, 0, and 0.5). Two stress levels were employed in each experimental test series.

Ti-6Al-4V titanium alloy fatigue test data were retrieved from AGARD R-767 [43] and Bang et al. [32]. The test data was generated on single-edge-notch tensile specimens at room temperature under constant-amplitude loading at only R=0.1 and R=-1. Due to

limitations of experiments, limited data sets could be retrieved for the above material. This remains a serious challenge for training ANNs.

The experimental FCG data sets for all five materials are shown in this section.

1. FATIGUE CRACK GROWTH DATA

As already mentioned, five different materials were chosen for this work because of their use in critical applications such as for aerospace industry. Experimental crack growth data presented above were retrieved from different reliable sources. To use these data, extraction by means of digitizing was performed. This process allowed replotting clearer figures by digitizing each data point off of the original figures. These extracted numerical values were then saved to files and used to train the ANN models.

1.1. Aluminum alloy 2024-T3

The 2024-T3 aluminum alloy is mainly composed of aluminum (90.7 - 94.7 %) with minor percentages of other chemical constituents such as: copper, magnesium, and manganese, etc [9]. The 2024-T3 aluminum alloy is used for a large range of applications such as aircraft fittings, gears and shafts, computer parts, and missile parts, etc. The mechanical properties are summarized in Table 1.

Table 1 Aluminum alloy 2024-T3 material properties [9]

E (MPa)	72000
σ_{ys} (MPa)	355
σ_{u} (MPa)	495

Figure 3 displays the digitized fatigue crack growth data for 2024-T3 aluminum alloy with different stress ratios R (-2, -1, 0, and 0.5) as a function of the stress intensity factor range, ΔK.

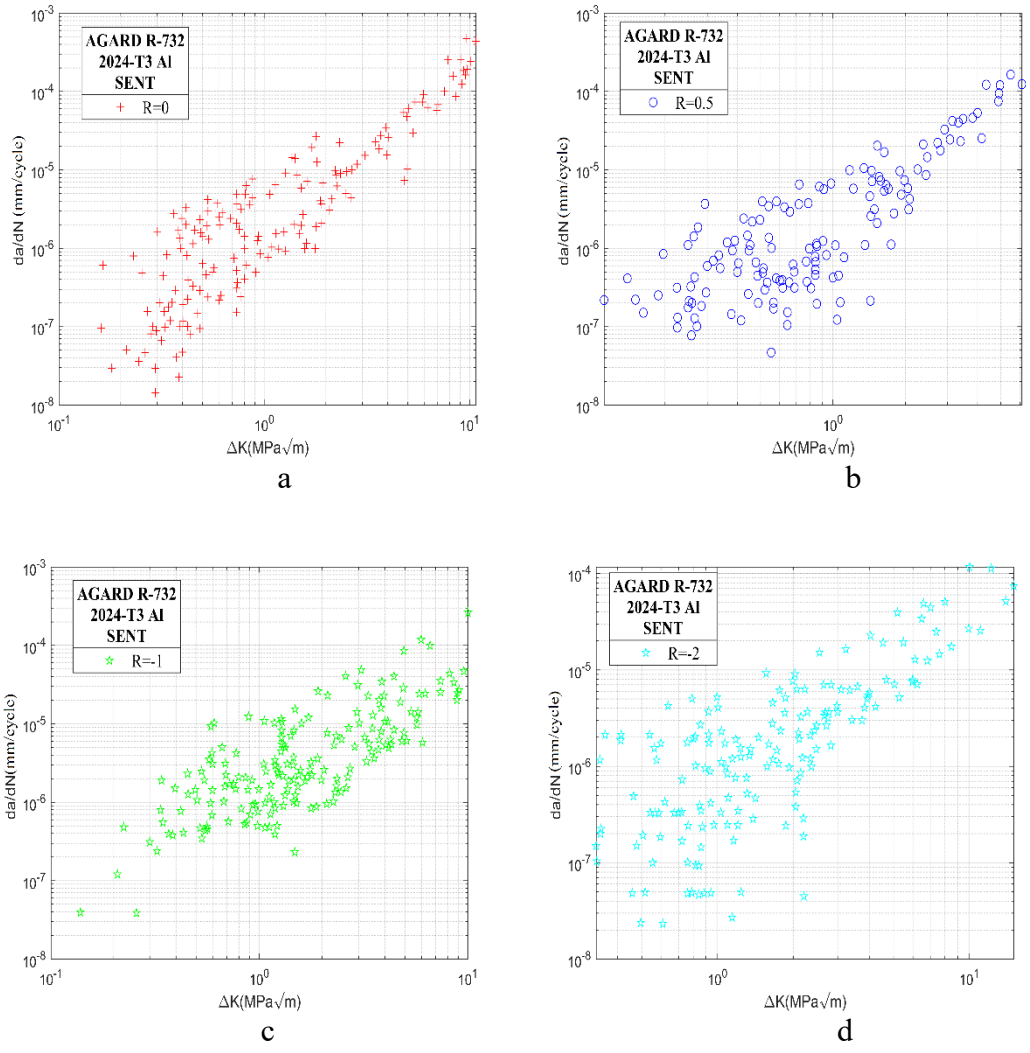

Figure 3 Digitized fatigue crack growth data for 2024-T3 aluminum alloy: (a) R=0, (b) R=0.5, (c) R=-1, (d) R=-2 [9]

As mentioned previously, test data were collected from Newman and Edwards [9] for 2024-T3 aluminum alloy with four stress ratio (R = 0, 0.5, -1 and -2) and over a fairly

wide range of stress levels, S_{max}. The AGARD test program (R-732) on the growth of small cracks conducted tests on single-edge-notch specimens of 2024-T3 aluminum alloy under constant-amplitude loading conditions and spectrum loading conditions.

Figure 4 represents crack growth data sets at four different R ratios (R = -2, R = -1, R = 0, and R = 0.5) employed in training the model.

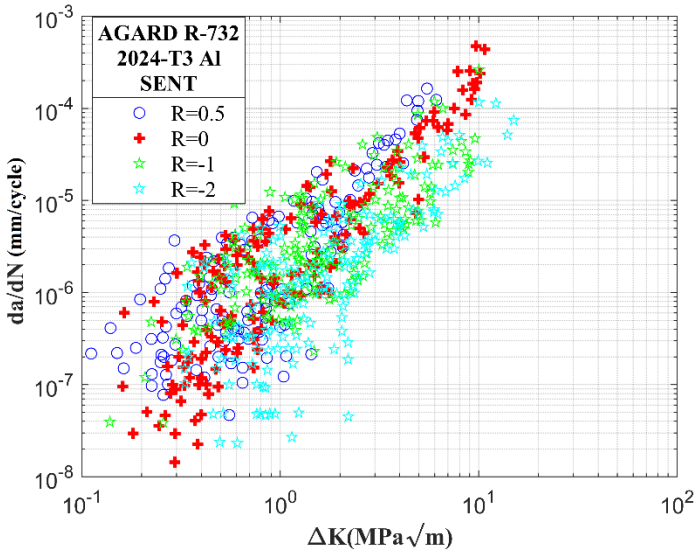

Figure 4 Fatigue crack growth data for 2024-T3 aluminum alloy at different stress ratios [9]

1.2. Aluminum alloy 7075-T6

The 7075-T6 aluminum alloy is primarily comprised of aluminum (87.1 - 91.4%) with percentages of copper, magnesium, manganese, and other chemical constituents [43][8]. This alloy is used for a wide range of applications that requires materials of high strength for highly stressed structural components such as aircraft fittings. The mechanical properties of 7075-T6 aluminum alloy are displayed in Table 2.

Table 2 Aluminum alloy 7075-T6 material properties [43][8]

E (MPa)	71700
σ_{ys} (MPa)	520

Figure 5 presents the digitized FCG data for 7075-T6 at different stress ratios R (R = -1, R = 0, and R = 0.5) as a function of the stress intensity factor range, ΔK.

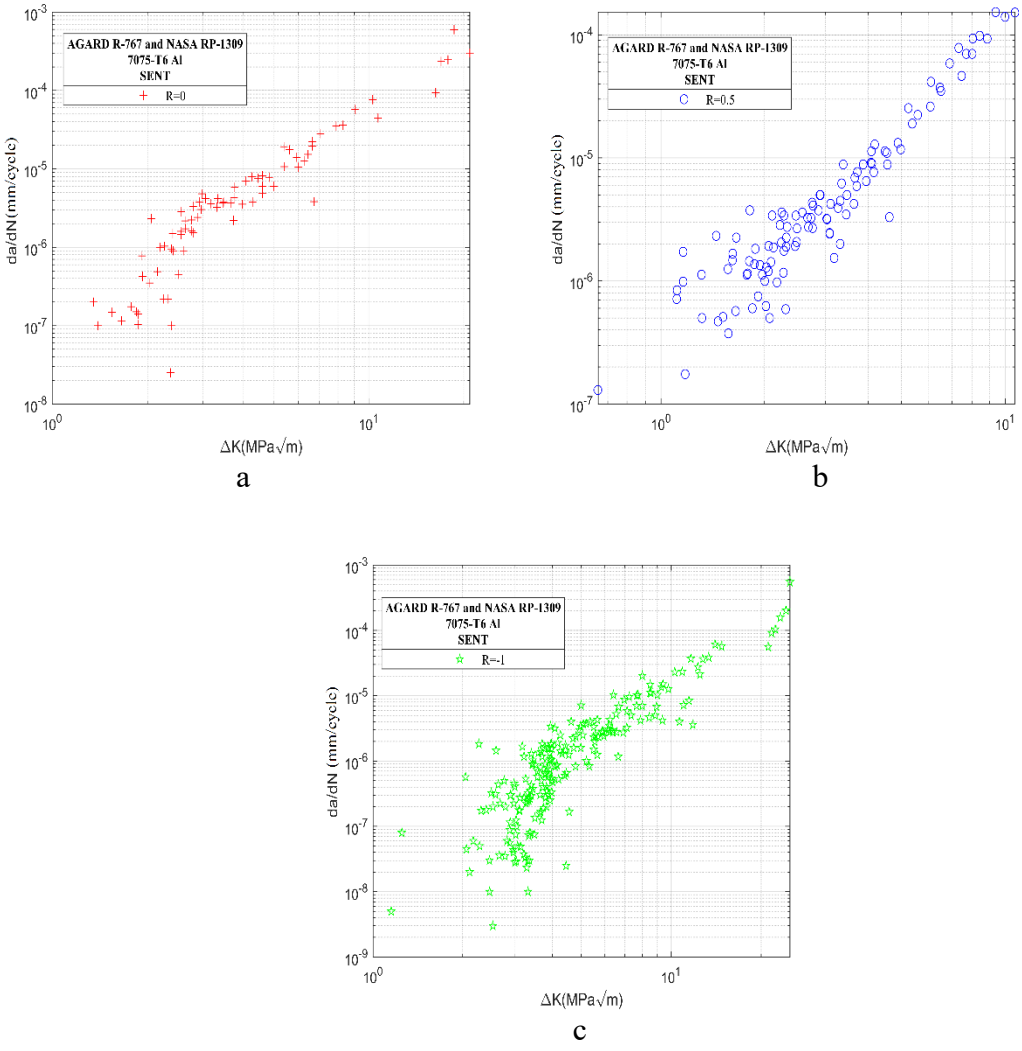

Figure 5 Digitized fatigue crack growth data for 7075-T6 aluminum alloy: (a) R=0, (b) R=0.5, (c) R=-1 [43][8]

Figure 6 is a representation of crack growth data sets at the three stress ratios (R= - 1, R= 0, and R= 0.5).

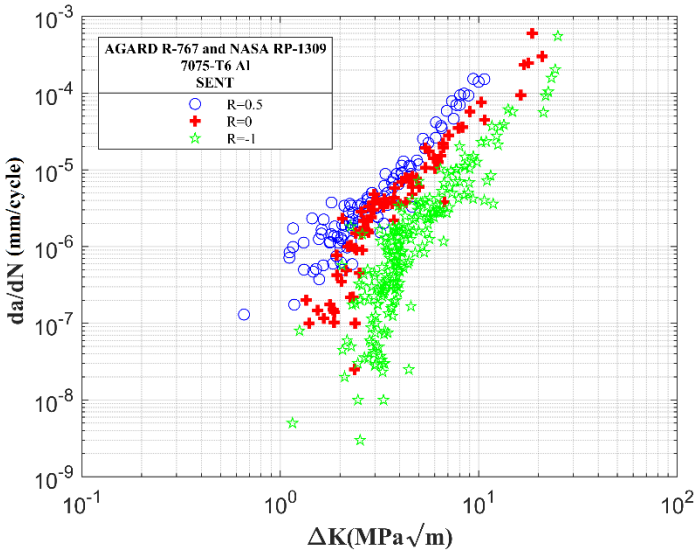

Figure 6 Fatigue crack growth data for 7075-T6 aluminum alloy at different stress ratios [43][8]

1.3. Aluminum-lithium alloy 2090-TBE41

The 2090-TBE41 aluminum-lithium alloy is mainly constituted of aluminum (93.2 -95.6 %) and percentages of copper, lithium, magnesium, and titanium, etc. [43]. The 2090-TBE41 aluminum-lithium alloy is mainly used in aircraft floor bulkhead stiffeners. The mechanical and fatigue properties are summarized in Table 3.

Table 3 Aluminum-lithium alloy 2090-TBE41 material properties [43]

E (MPa)	78200
σ_{ys} (MPa)	525
σ_u (MPa)	580

Figure 7 displays the FCG data for 2090-TBE41 with different stress ratios as a function of an equivalent stress intensity factor range, ΔK_{eq}. The aluminum-lithium alloy produced small cracks that initiated and grew at a severe angle on the single-edge notch surface, so an equivalent stress-intensity factor range (mixed mode) was calculated. Thus, these small crack data are complex during to the cracks growing at about 60 deg to the loading direction. This high strength alloy is comparable to 7075-T6 aluminum alloy.

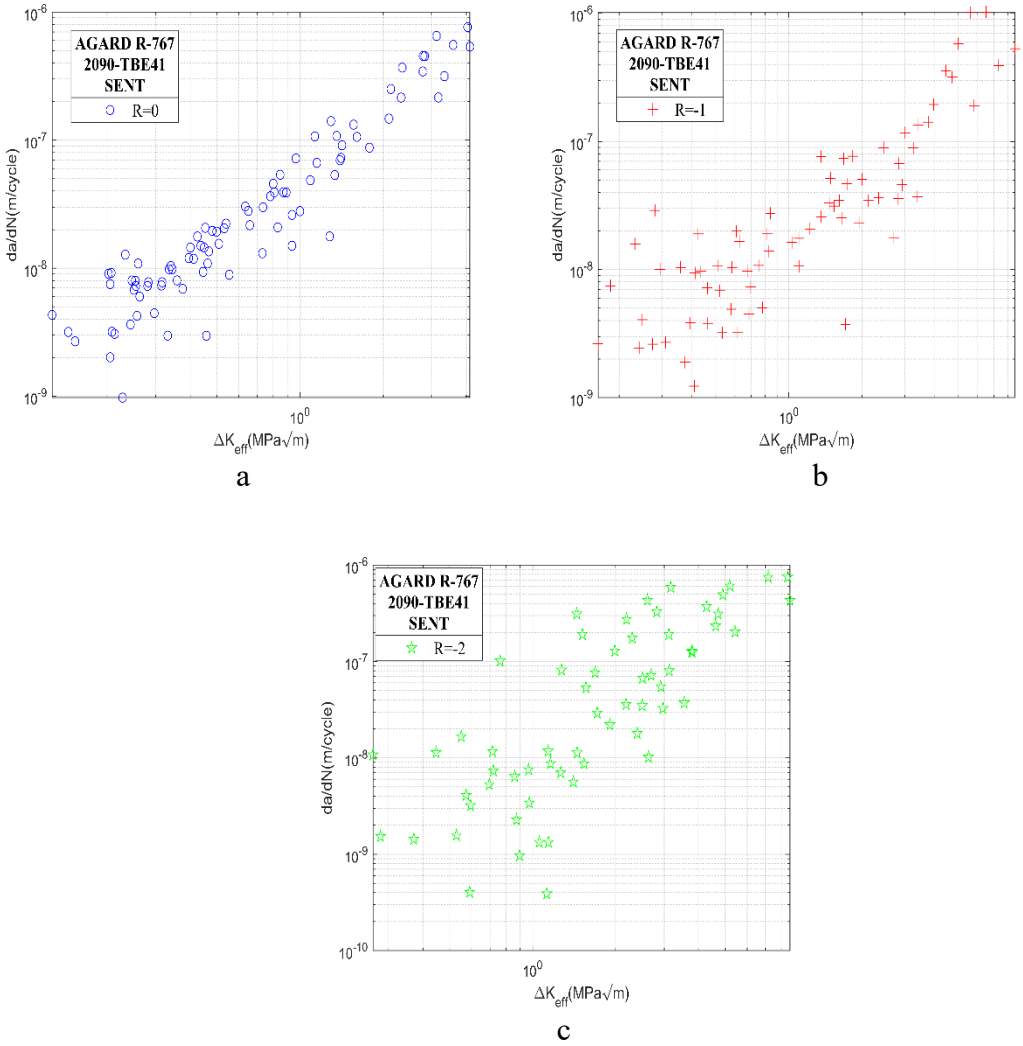

Figure 7 Digitized fatigue crack growth data for 2090-TBE41 aluminum-lithium alloy: (a) R=0, (b) R=-1, (c) R=-2 [43]

Test data were collected from AGARD R-767 [43] for 2090-TBE41 aluminum-lithium alloy at three stress ratio (R = 0, -1 and -2) and over a fairly wide range of maximum stress levels, S_{max}. The crack growth data sets at the three R ratios (R = -2, R = -1, and R = 0) are shown in Figure 8.

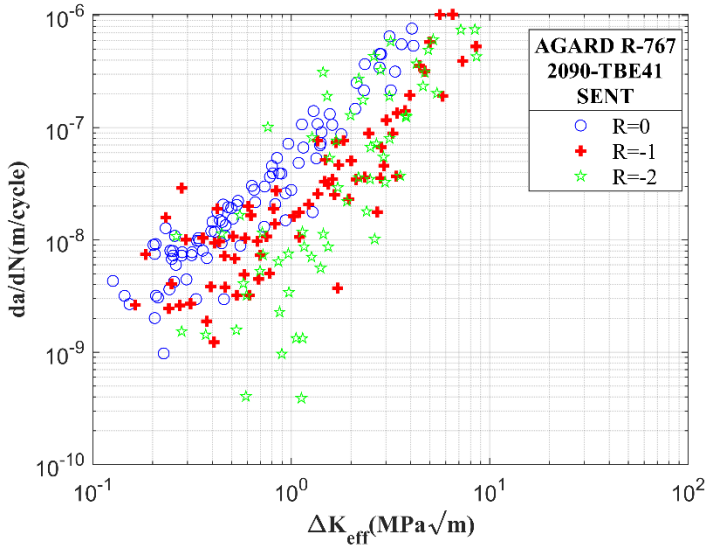

Figure 8 Fatigue crack growth data for 7075-T6 aluminum alloy at different stress ratios [43]

1.4. Aluminum alloy LC9cs

The LC9cs clad alloy is a corrosion resistant aluminum comparable to 7075-T6 aluminum alloy in chemical composition. This material is used expansively in the aerospace industry as an aviation-grade material and in the construction sector. The mechanical and fatigue properties are summarized in Table 4.

Table 4 Aluminum alloy LC9cs material properties [8]

E (MPa)	66400
σ_{ys} (MPa)	514

Test data were obtained from NASA RP-1309 [8] for LC9cs aluminum alloy at three stress ratio (R = 0, 0.5 and -1). Figure 9 displays the fatigue crack growth data for LC9cs at different stress ratios as a function of the stress intensity factor range, ΔK. Figure 10 represents the experimental data at the three different R ratios.

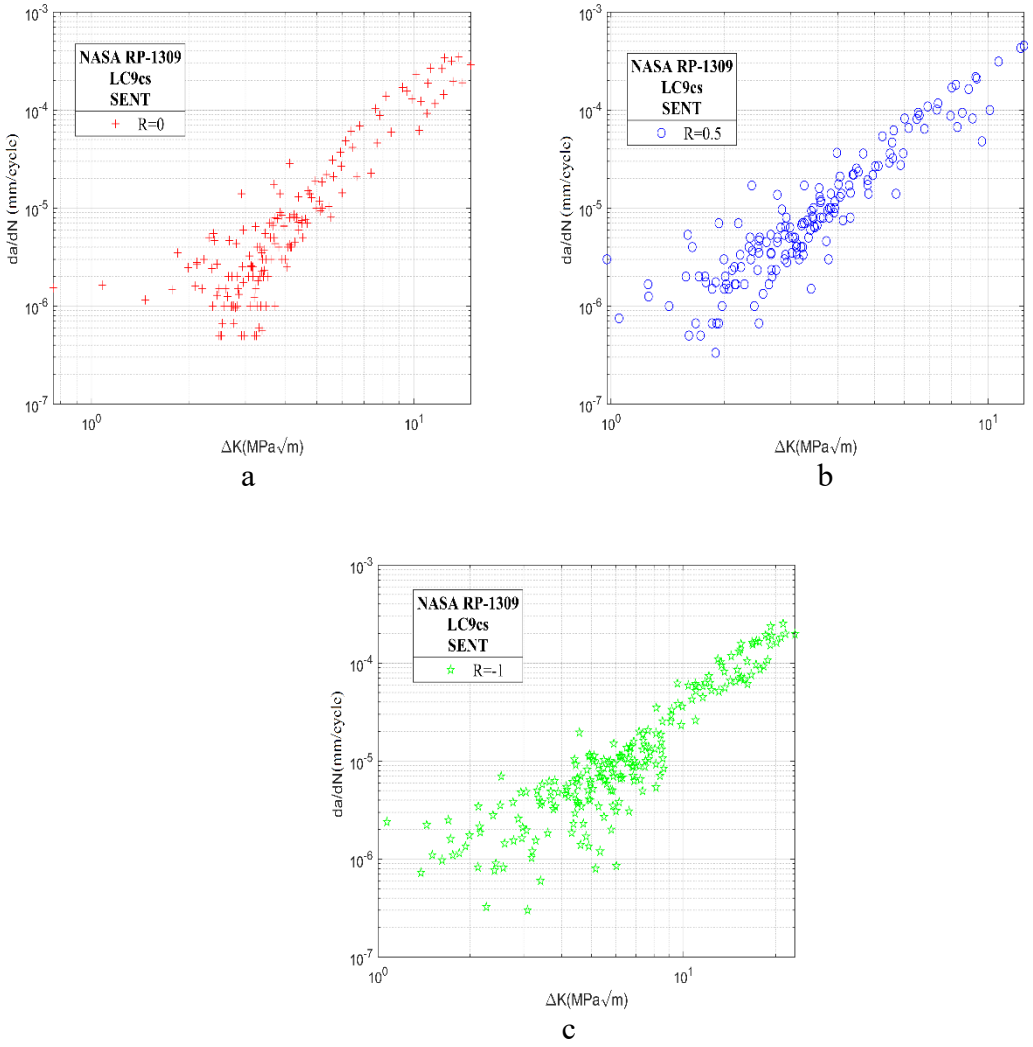

Figure 9 Digitized fatigue crack growth data for LC9cs aluminum alloy: (a) R=0, (b) R=0.5, (c) R=-1[8]

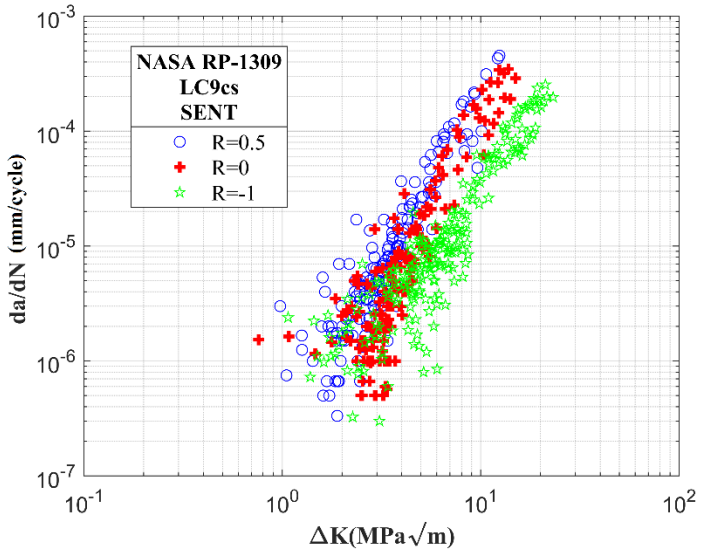

Figure 10 Fatigue crack growth data for LC9cs aluminum alloy at different stress ratios [8]

1.5. Titanium alloy Ti-6Al-4V

The Ti-6Al-4V titanium alloy is composed of titanium (90 %) with small percentages of other chemical constituents (e.g., aluminum, vanadium, and iron, etc.). This material is used for high strength-to-weight ratio applications where excellent corrosion resistance is also essential, such as implants and gas turbines. The mechanical and fatigue properties are summarized in Table 5.

Table 5 Aluminum alloy Ti-6Al-4V material properties [43] [32]

E (GPa)	117
σ_{ys} (MPa)	1185
σ_f' (MPa)	2030
b	-0.104

Ti-6Al-4V titanium alloy data sets were retrieved from AGARD R-767 [43] and Bang et al. [32] at two stress ratio and a wide range of stress levels. Figure 11 displays the

FCG data for Ti-6Al-4V as a function of the stress intensity factor range, ΔK. Figure 12 presents the FCG data sets at two stress ratios (R = 0.1, and R= -1).

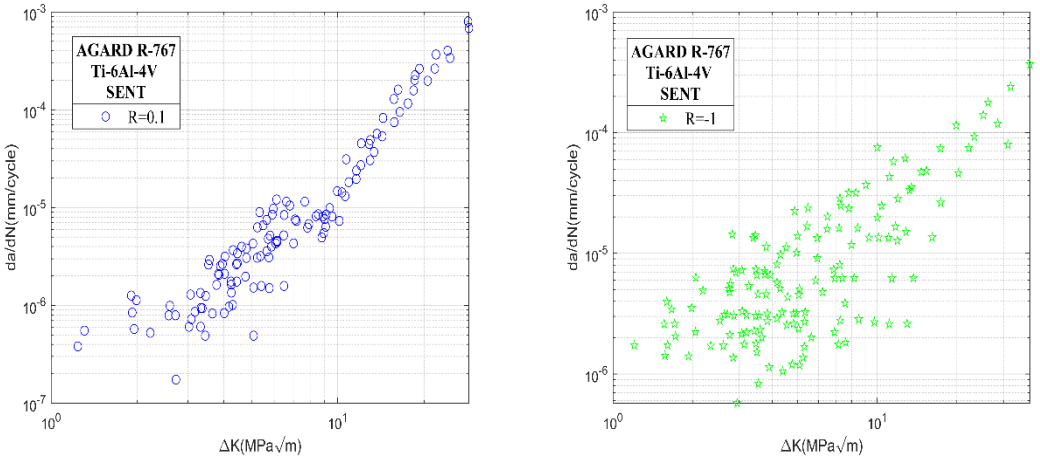

Figure 11 Digitized fatigue crack growth data for Ti-6Al-4V titanium alloy: (a) R=0.1, (b) R=-1[43][32]

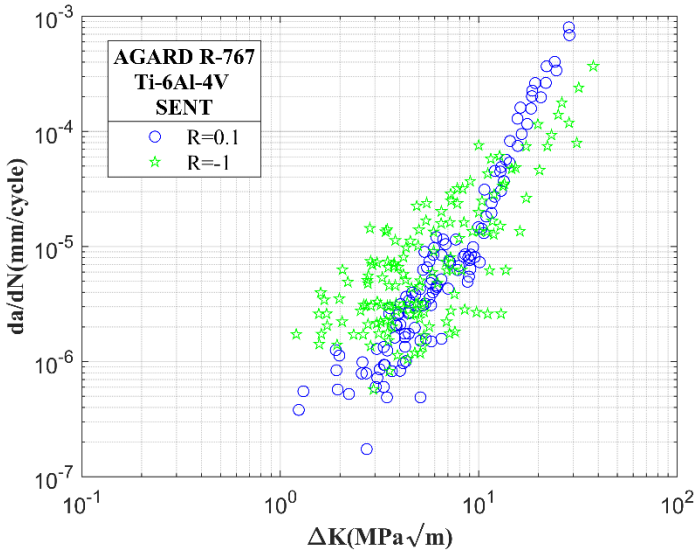

Figure 12 Fatigue crack growth data for Ti-6Al-4V titanium alloy at different stress ratios [43][32]

CHAPTER III

DESIGN OF ANNS AND METHODOLY

1. Artificial Neural Network

Artificial neural networks, ANNs, are one of the forms of machine learning (ML). These artificial intelligence (neural network, deep learning, robotic) tools have long been used for classification, clustering, pattern recognition and regression problems in many areas.

Neural network is an information-processing paradigm mimicking the human brain that consists of communicating neurons. This communication is in the form of a mathematical equation that collects inputs to produce outputs. ANNs have been known since the 1950s, but it was not until the 1980s that these connectionist mathematical representations became revolutionary and widely used.

From a biological point of view, for information-processing, the communication between the hundred billion nerve cells in the mammalian brain is done via electrical signals called spikes. These biological neurons are constituted of: dendrites, cell body (soma) and the axon [36] as illustrated in Figure 13. The first step of information-processing in this complex organism is when one of the neurons in the dendrite fires after an electric charge is received. The strengths of these charges are added together through spatial summation (i.e., numerous weak signals are transformed into a single signal) and temporal summation (i.e., various rapid weak pulses are translated to a single signal). The second step is when the input is passed to the soma and the neuron fires (when the input is larger than the axon threshold value). Finally, the output signal is communicated to the axon.

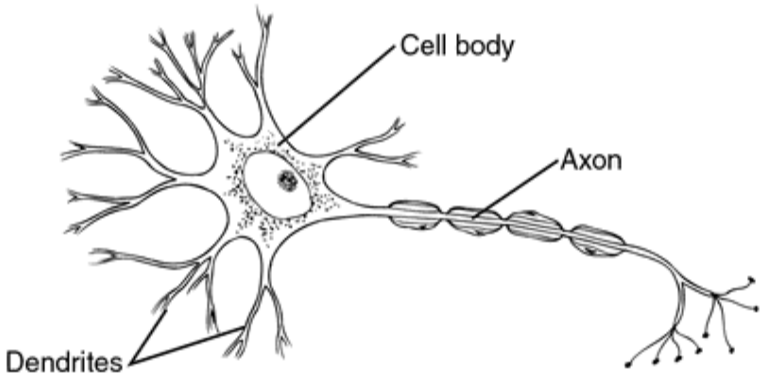

Figure 13 Illustration of the three principal components of a biological neuron [44]

ANNs mimic the properties of this biological parallel learning system. Similar in some ways to the human brain, ANNs are capable of recognizing some operational tasks (i.e., language processing, object recognition, speech recognition, etc.). This makes ANNs a powerful tool that can learn like humans do.

One of the most noticeable advantages of ANN is its ability to model data without prior knowledge of any mathematical distribution that results in misleading information, contrary to other analytical models where data is assumed to fit a mathematical distribution that could be erroneous [45].

1.1. Structure of ANN

Likewise human brains, ANNs algorithms consists of neurons tied together with weighted links and a transfer function [36]. As can be seen in Figure 14, a typical neural network has three layers (i.e., an input layer, a hidden layer, and an output layer). The input layer has input neurons specified by users and the output layer has output neuron(s) (depending whether the output layer is a single output or multiple output). Parameters like the number of neurons and layers in the hidden layer(s) are chosen by users and depend on the application and the particular model. Each connection between neurons in the neural

network has weight coefficients at each synapse. The number of neurons in a specific layer are referred to as bias nodes that are set to 1. When the neural network is used for classification problems, the input and output nodes have similar properties as inputs and output classes, however, for regression problems, the neural network has an input and an output node. At each neuron in the layer, the outputs of all synapses coming to that neuron and a bias are summed up and an activation function is applied to the weighted sum. Each output of the activation is the input for the next synapse layer, and the results of all synapses are added together and passed into a linear function to reach the final output(s).

The activation function is a link between the input signals feeding the neuron and its outputs which helps the neural network learn complex data from any function and provide accurate predictions. There are numerous types of activation functions and the most frequently used ones are:

Linear function:

$$f(x) = ax \tag{1}$$

Sigmoid function:

$$f(x) = \frac{1}{1+e^{-x}} \tag{2}$$

Tanh:

$$f(x) = \frac{2}{1+e^{-x}} - 1 \tag{3}$$

Rectified linear unit (ReLu) functions:

$$f(x) = \begin{cases} 0, & x < 0 \\ x, & x \geq 0 \end{cases} \tag{4}$$

The selection of activation function is a crucial step when designing and training a model. The process is mostly a trial and error process where the user experiments with different activation functions to attain good results.

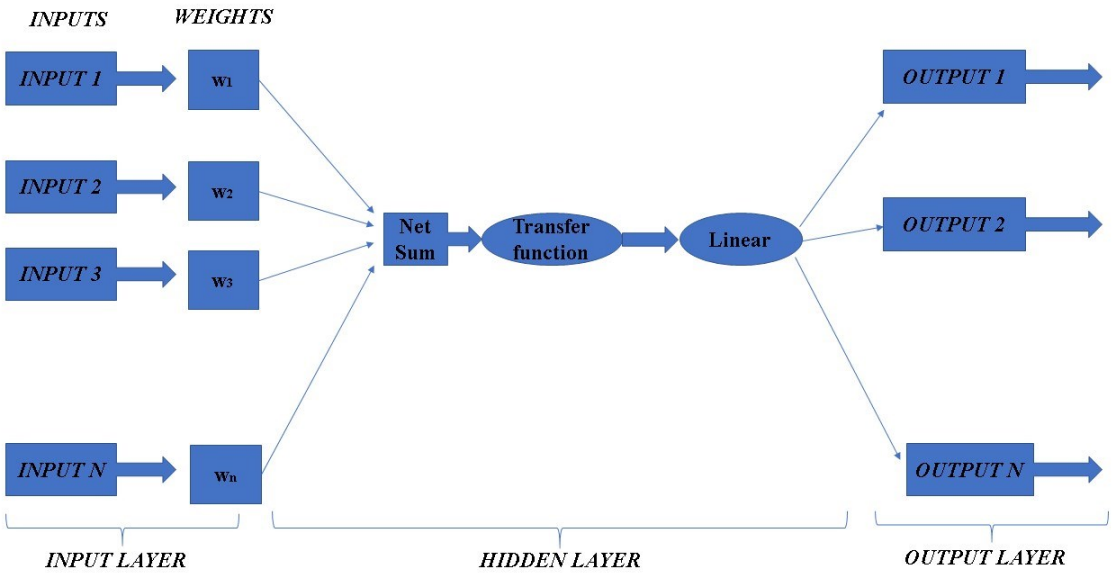

Figure 14 General diagram of a typical ANN with input, hidden and output layers

1.2. Types of ANN

ANN can be classified into two main types that embed many other classes as can be seen in in Figure 15.

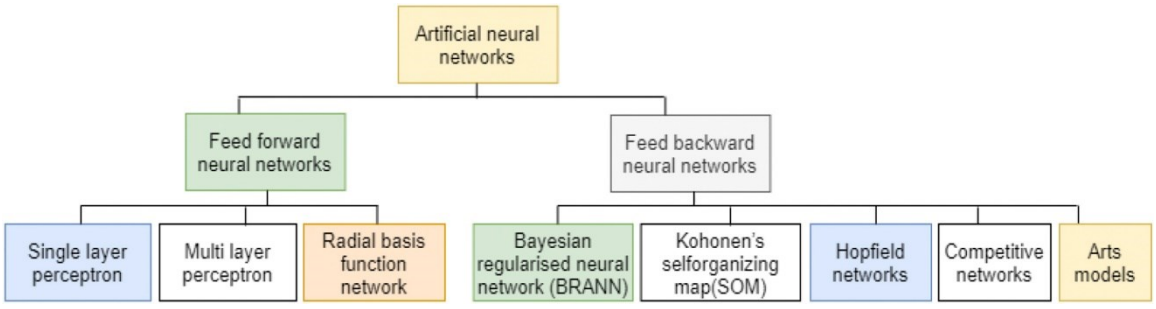

Figure 15 Framework for ANNs types [44]

(a) Feedforward neural networks (FFNN):

This type of ANN is the oldest and most used in numerous supervised applications such as speech recognition. FFNN are known to handle tasks according to first come first serve [44]. The flow of information through FFNN is forward, owing it its name. All nodes in the FFNN are connected and the data entry from each input node flows through the hidden layers in one direction until reaching the output nodes. FFNN can be either single-layered or multilayered depending on the number of layers in the network. Single-layered networks have two layers of neurons and no hidden layers in between. Multilayered perceptron also referred to as deep networks have input and output layers and multiple hidden layers in the midst of them.

(b) Feed backward neural networks (FBNN):

Unlike FFNN, information in FBNN can be transmitted through loops. This particular type of NNs can be used in applications that require use of internal state "memory" such as pattern and sequence recognition [44].

In this work two FFNNs type of algorithms are used: radial-basis function (RBFN) and extreme learning machine (ELM).

A continuous function f(x) can be estimated by FFNNs with hidden neurons in the hidden layers. For FFNNs with sufficient number of neurons (L), given any small positive value ε, we have $||f_L(x)-f(x)||< \varepsilon$.

In real applications, target function f is usually unknown. The goal is for the unknown f to be approximated by FFNNs appropriately.

With all that being said, ANN cannot function exclusive of human intervention and researchers should be involved in making data sources available to all user ends. A major

issue in the progress of this work was the insufficient experimental small cracks data that was retrieved. In some cases, data-cleaning may be needed; however, ANN is still an excellent mean to tackle many complex issues without the need of making big changes to data sets.

1.3. Radial-basis function RBFN

Radial basis function network is a simple 3-layered type of FFNN that uses radial basis functions as activation functions instead of a logistic function. Logistic functions map values to a range between 0 and 1 (yes or no) which is beneficial to classification problems and cannot be applied to problems with continuous values. RBFN are the perfect fit for function approximation since values are constantly optimized. In RBFN, the input layer is only used to transfer information without variation in weights [40]. An input vector with 'm' number of input neurons is fed as an input to the radial basis functions. The output of the network with 'n' number of neurons is a linear grouping of radial basis functions. In between these two layers lies the hidden layer which comprises N cells defined by the radial function equation below:

$$\phi(x, c) = \phi(\|x - c\|) \tag{5}$$

The radial basis function value depends only on the real function of the distance from the origin, namely Φ (x) = Φ (‖x‖) with x being the input signal, or the distance to any point c being the center of the radial function Φ (x,c) = Φ (‖x-c‖). The Gaussian function is the main radial function used in many applications and the cells of the hidden layers can expressed as:

$$\phi_J(x) = \phi\left(x - x_j\right) = e^{-\left(\frac{1}{2\,\sigma j^2}\right)|x-cj|^2} \qquad \text{j=1, 2,…,N} \tag{6}$$

Where cj being the center of the basis function in the j^{th} point and σj the width of the cj centered Gaussian function [39].

As shown in the figure below, the RBF network is a multi-layer forward network. More specifically the RBF network is a three-layer forward network. The scheme shows that each input corresponds to a predictor variable (x_1,x_2,..,x_n). The input layer is composed of signal source nodes. The second layer is defined as the hidden layer. In the hidden layer, the number of hidden neurons depends on the specific type of problem. Each neuron in the hidden layer consists of a gaussian RBF (μ) which is a positive nonlinear function with radial symmetry and attenuation to the center point (c). The RBFN places RBF neurons in the space described by the input variables. When presented x vector of inputs, the Euclidean distance is calculated from a data point to the center of each neuron. The RBF function is applied to the Euclidean distance. The third and final layer is the output layer, which responds to the input pattern [46]. The output Y(x) is simply the weighted sum of outputs from the hidden layer.

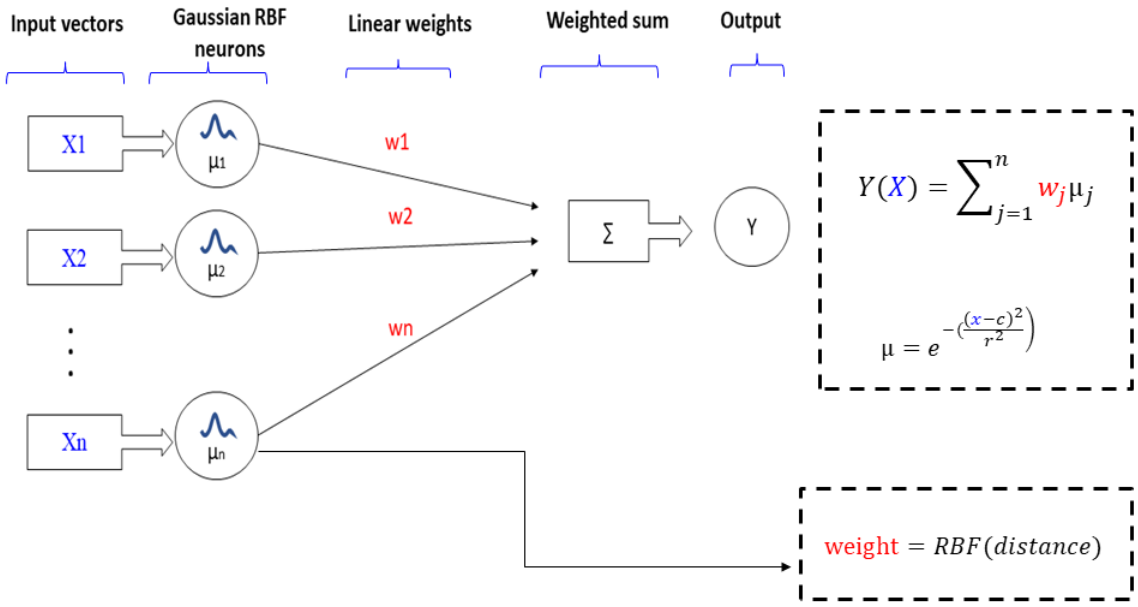

Figure 16 Structure of a radial basis function network.

Some radial functions typically use an approximation to a given function, which can be interpreted as a simple neural network. Radial basis functions are also used as kernel functions in support vector machine classification. In 1971, Hardy [47] used a radial basis function multi-quadric to solve the problem of aircraft contour design surface fitting, and achieved very good results. Since then, radial basis function networks were used for many different fields, including function approximation, classification, and system control.

In RBFN, the hidden layer uses a nonlinear approach to optimize the number of neurons of the RBFN, while a linear approach is used in the output layer to optimize the weights. Consequently, the RBFN can properly solve nonlinear problems. In this thesis, the RBFN is used because it has been demonstrated previously that this method is suited for fatigue crack growth under constant and variable amplitude loading [40].

1.4. Extreme learning machine ELM

Extreme learning machine (ELM) is a machine learning system or method based on the FFNN, which is a single-hidden layer feed-forward neural network (SLFN). It is both appropriate for supervised learning and unsupervised learning [48].

Its characteristic is that the weights of the hidden layer nodes are randomly or artificially given and are independent of training data and each other [48], and no update is needed. In the learning process, only the output weights are calculated. Unlike conventional learning methods, ELM generates the hidden node parameters before learning the training data. Compared with other shallow layer learning systems, such as Single-layer Perceptron, ELM is considered to have advantages in learning rate and generalization ability [49]. The applications of ELM include computer vision and bioinformatics, as well as regression problems in some earth sciences and environmental sciences.

The structure of extreme learning machine is very similar to the three layers FFNN as seen in Figure 17. The layers in the ELM method are fully connected and ELM can randomly produce the weights and the thresholds from the input layer to the hidden layer before training. The training parameters do not need to be iteratively adjusted during the training phase. The training parameters that needs to be learned is the connecting weights between the hidden layer and the output layer. In addition, an infinitely differentiable function must be selected as the activation function (The differentiability of activation functions allows for the optimization of the model's error). The activation function is responsible for activating each neuron attached to it and normalizes the output of each neuron between a specific range. By setting the neuron number in the hidden layer, the ELM can reach an optimal generalization bound.

The output function of the ELM is represented as follows:

For L number of hidden nodes and $h_i(x) = G_i(a_i, b_i, x)$ being the output function of the i^{th} hidden layer

$$fL(x) = \sum_{i=1}^{L} (\beta i G(a_i, b_i, x)) \quad (7)$$

β refers to the weights linking the hidden layer neurons and the output layer and β_i is the output weight of the i^{th} hidden node.

The output functions of hidden nodes can be: sigmoid, RBF, cosine/Fourier basis functions, hard limit, etc.

In a matrix form, the hidden layer output H is:

$$H = \begin{pmatrix} h(x_1) \\ \cdot \\ \vdots \\ h(x_N) \end{pmatrix} = \begin{pmatrix} G(a_1, b_1, x_1) & \cdots & G(a_L, b_L, x_L) \\ \cdot & \cdot & \cdot \\ \cdot & \cdot & \cdot \\ G(a_1, b_1, x_N) & \ldots & G(a_L, b_L, x_N) \end{pmatrix} \quad (8)$$

Where $h(x) = [G(h_i(x), \ldots, h_L(x)]$ is the hidden layer of the output mapping of ELM and

$$H = \beta T \quad (9)$$

With T being the training data target matrix.

During the prediction process, the output weights for both classification and regression problems can be calculated as:

$$\beta = H^T T \quad (10)$$

With H^T being the pseudo inverse of the hidden layer output matrix H.

The objective function of ELM is solving for the output weight β and minimizing: $||H\beta - T||_p$ and $||\beta||_q$, where p, q = 0, 1/2, 1, 2, …, +∞.

Generally, ELM methods are more advantageous than other neural network methods because their learning speed is much faster and the training error is very small [34].

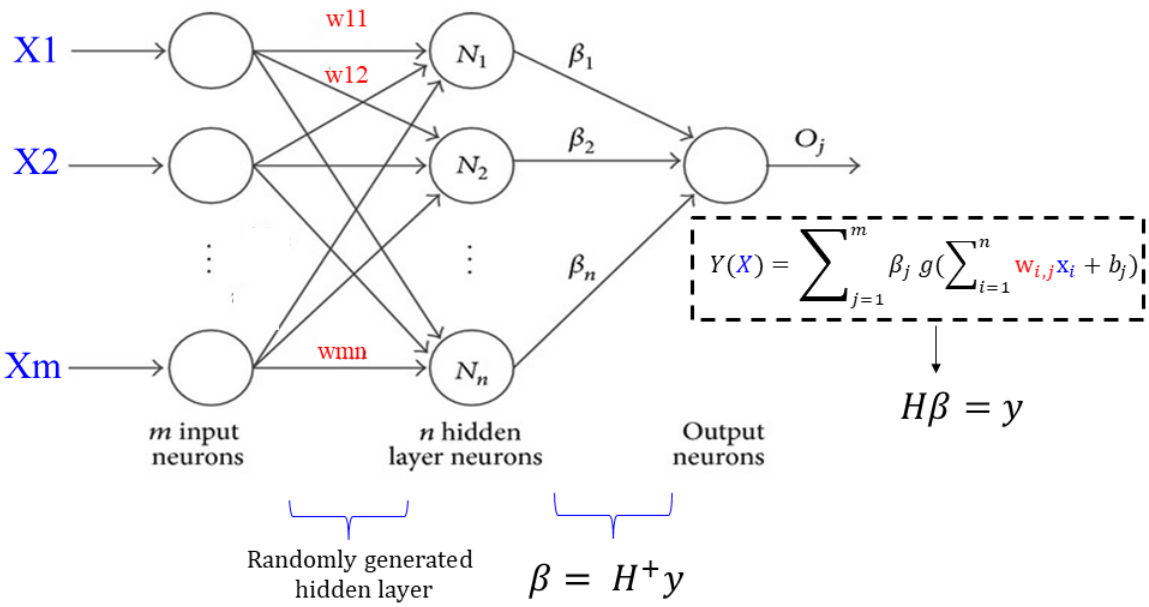

Figure 17 Structure of an extreme learning machine network.

1.5. Design and training of ANN

Both ANNs: RBFN and ELM predictive models where designed and trained using Neural Network toolbox of MATLAB R2018b software is used for RBFN. The toolbox has a function called “newrb” meant to create the radial basis network. The “newrb” is a function of the input and output vectors, the network mean squared error (MSE) goal, and the spread of the RBFN. The function adds neurons to the network one at a time until the MSE is less than the goal specified by the user (usually 0) or until the maximum number of neurons is reached. For ELM, the source codes published by Huang et al. [49] were modified and used for training the model and a MATLAB R2018b software code was written for simulating the network based on the existing equations for ELM. In ELM, the parameters that need tuning were the activation function and the number of neurons. These optimal parameters were the same used for all the materials. The first step to develop the models is to designate the stress intensity range, ΔK, stress range, ΔS, and stress-ratio, R

as inputs since they are the driving parameters and the crack growth rate, *da/dN* as the output as can be seen in Figure 18. The next strep to develop the three-input/ single output algorithms is to extract the raw experimental data from corresponding sources by digitizing and saving them into data files with a set of vectors that can be manipulated. For more accurate results while running the ANN model, the crack growth data sets obtained from the literature had to be normalized because the stress intensity range, ΔK, the stress range, ΔS, and the stress-ratio, R, have different ranges and this step generally speeds up the learning process and leads to faster convergence.

As can be seen in Figure 18, the ANN models learn the relationships from the input and output experimental data and establish a continuous function shown below:

$$\frac{da}{dN} = f(\Delta K, S_{max}, R) \tag{11}$$

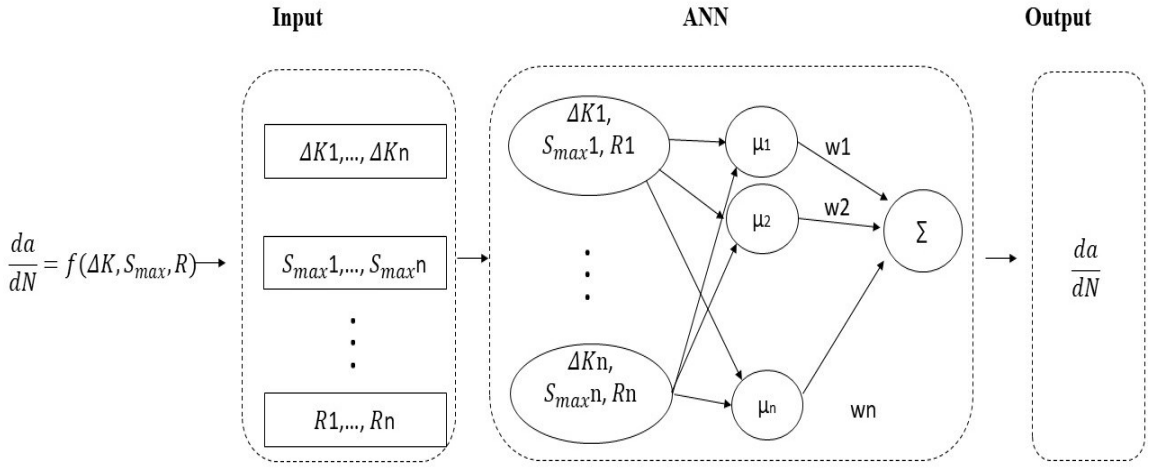

Figure 18 Schematic presentation of the three-layer ANN used in this work

Training RBFN necessitates randomly selecting parameters such as the maximum number of neurons and the mean squared error (MSE) goal (set as 0) and the spread. The

training runs until the network's MSE is below the goal. The spread stands for the number of Gaussian neurons required to smoothly fit a function and is advised to be set as the distance between the data points of a data set. The RBFN training function generates a two-layer network with radial basis neurons and weighted inputs. Neurons are then added to the hidden layer of the RBFN until the mean squared error goal (MSE) which controls the fitting accuracy is attained. The function takes parameters such as the maximum number of neurons and the MSE goal and trains based on the input and output data. To identify the optimal parameters to achieve a smooth function approximation, many attempts were made until the network's MSE was the closest to the goal. Another function is then used to simulate the neural network by using its properties to output the predicted results.

Data were divided into training data using around 70% of the experimental data and the rest was testing data, this dividing selection was done based on the implemented data division of the RBFN MATLAB function “newrb”. This step was done automatically and randomly using the MATLAB function for RBFN and manually for ELM. The best accuracy is attained after an optimization procedure by comparing the training outputs to the experimental data as well as when the mean squared error (MSE) is the closest to the goal. The last step is to simulate the networks on a set of testing data that was taken as 30% of the initial test data set for each material. The predicted results were then compared to the experimental data. The same number of neurons was used for all materials. Figure 19 illustrates a simplified flowchart of the proposed methodology.

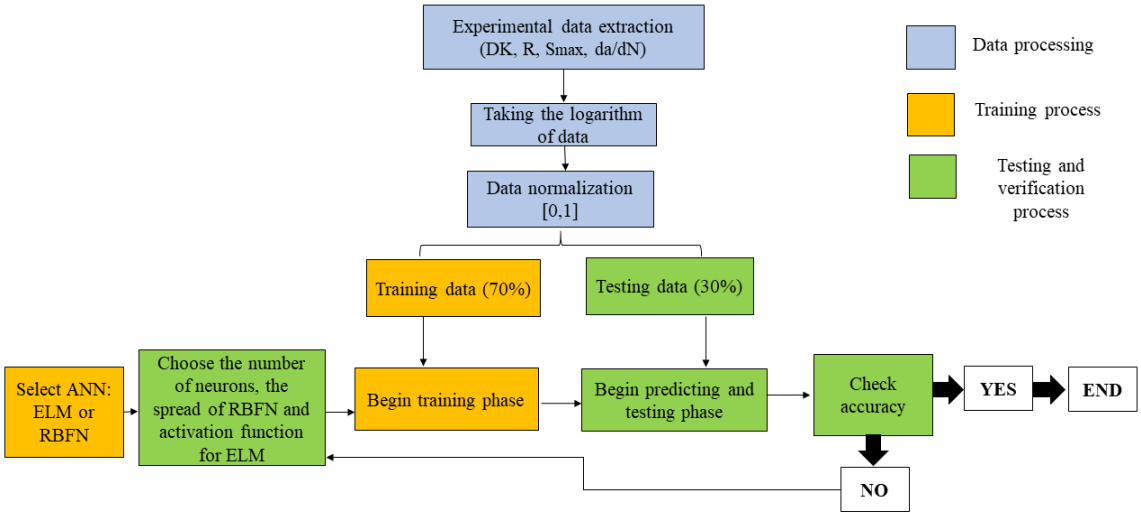

Figure 19 Flow chart for designing a well-trained ANN

CHAPTER IV

FATIGUE LIFE PREDICTION SIMULATIONS

1. Aluminum alloy 2024-T3

Experimental test data of 2024-T3 aluminum alloy at four stress ratios (R=0.5, R=0, R=-1, and R= -2) and a wide range of stress levels (50 MPa to 225 MPa) were used to conduct FCG analyses. As previously discussed, two ANNs were used to be compared: RBFN and ELM. The experimental data [9] was divided randomly by the RBFN model into 70% training and 30 % testing data. The same data division was performed manually for the ELM model. Many attempts were made to find the training parameters that would fit the experimental data for both ANNs. The maximum number of neurons used were n_n=15 for both RBFN and ELM. A "sigmoid" type of activation function was used for ELM since the range of data after normalization is between 0 and 1. These parameters will be used for all materials in order to provide a single model for all materials.

Figures 20 shows the experimental data with the ANN predictions by both methods. For the data set, 3D plots of the three variables *da/dN*, ΔK, S_{max} are presented and the color scale represents the stress ratio, R. The training and testing data are represented in Figure 20 by filled circles symbols, whereas the ANNs predictions are represented by empty circles symbols. In Figure 20 (b), the training data symbols are slightly bigger than the symbols for the testing data for the sake of differentiation. Both figures show that the ANNs (empty circles symbols) generally follow the trend of the experimental data.

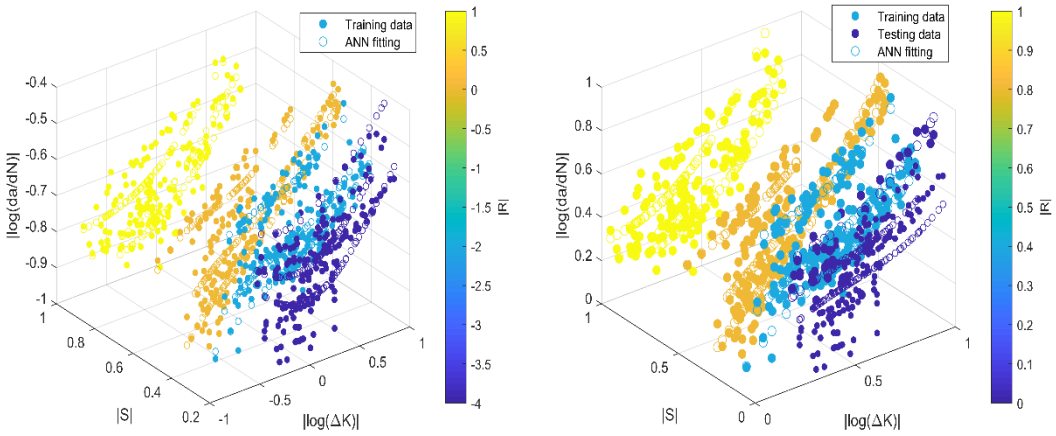

a b

Figure 20 3D representation of ANN fitting the experimental data of 2024-T3 aluminum alloy at different R ratios: (a) RBFN (b) ELM

Figure 21 and 22 exhibit the 3D predicted surfaces by both ANNs for this material. The two ANNs display smooth surfaces that show a reasonable behavior that agrees with the experimental data trend.

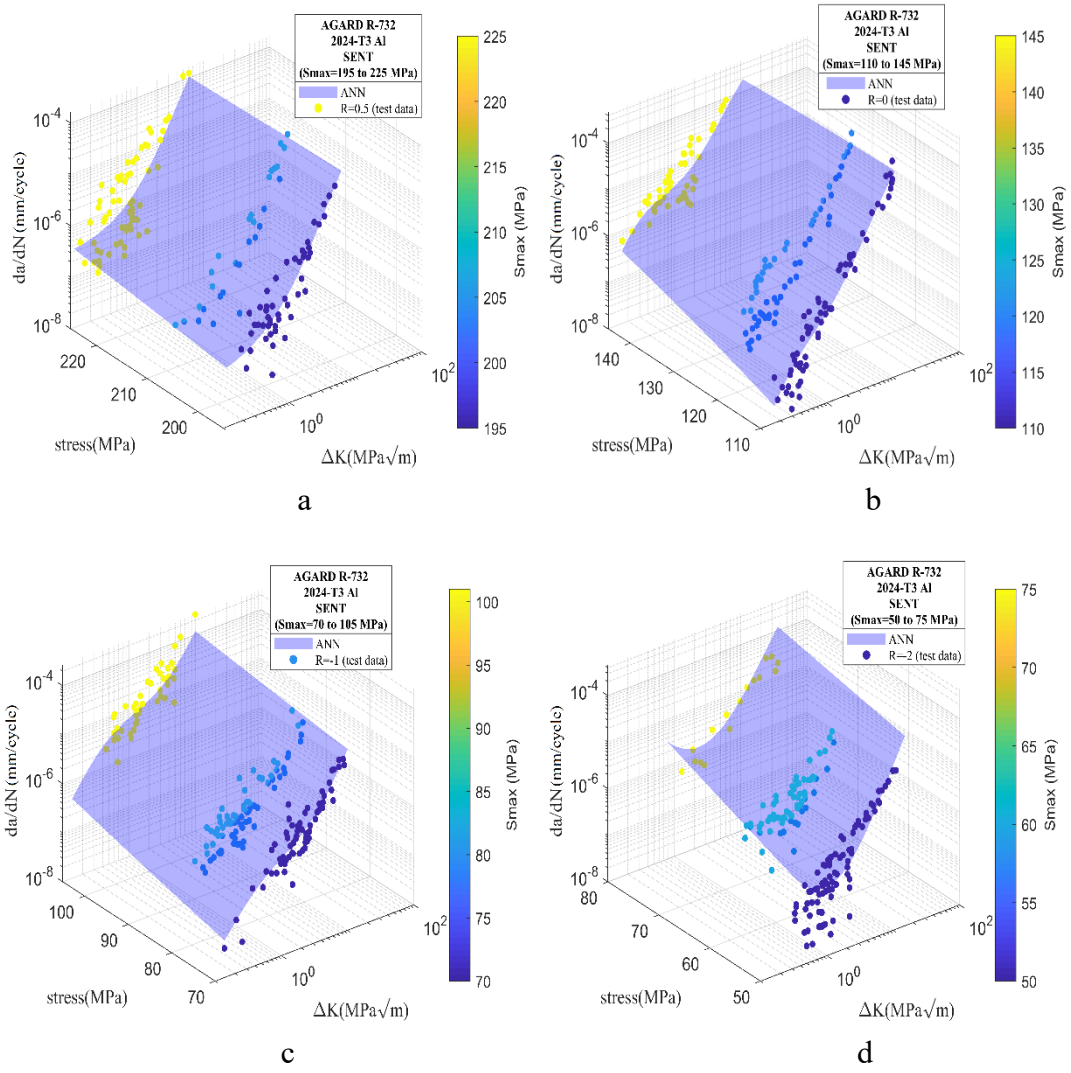

Figure 21 The predicted 3D surfaces by RBFN of 2024-T3 aluminum alloy: (a) R=0.5; (b) R=0; (c) R=-1; and (d) R=-2

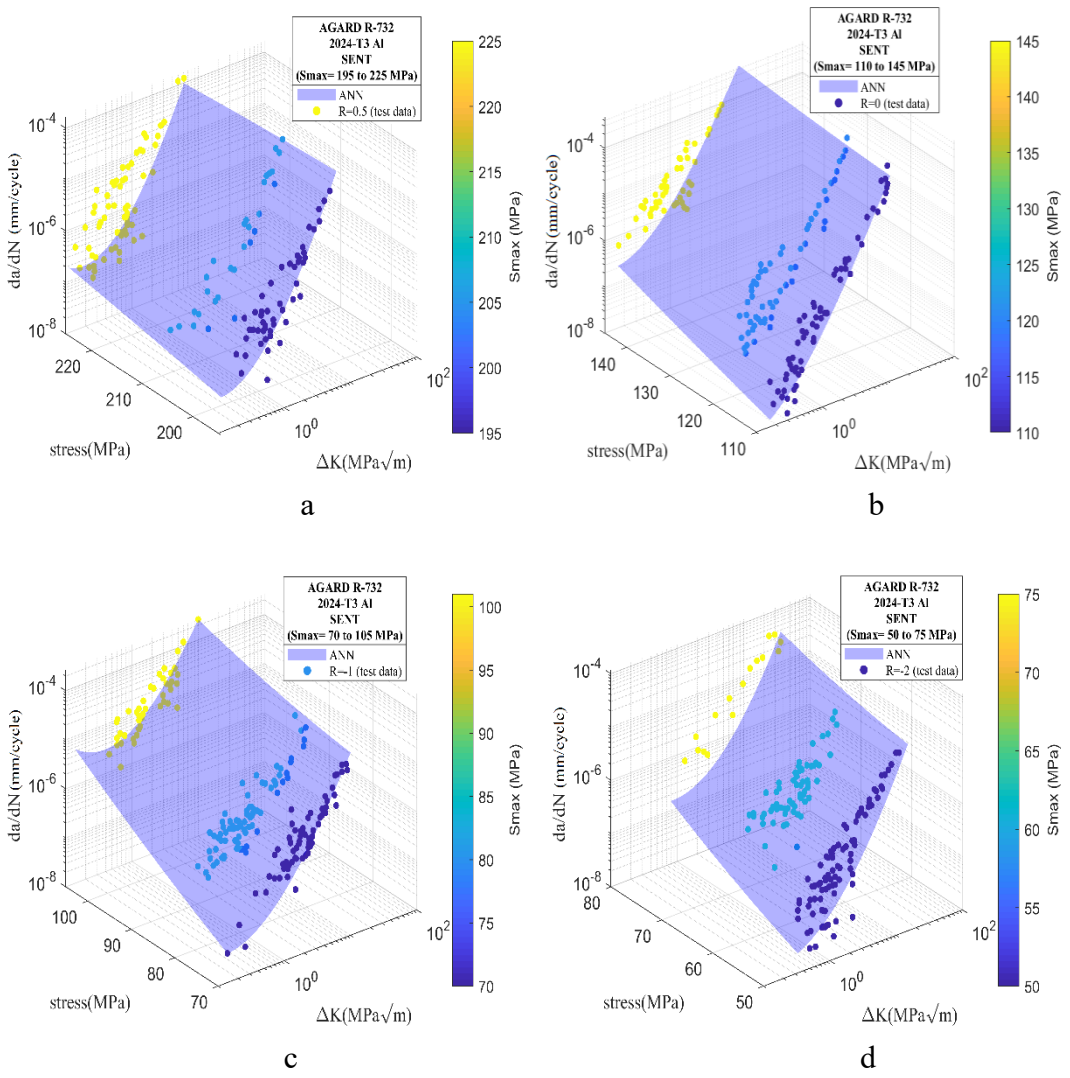

Figure 22 The predicted 3D surfaces by ELM of 2024-T3 aluminum alloy: (a) R=0.5; (b) R=0; (c) R=-1; and (d) R=-2

Figure 21 (a) and Figure 22 (a) show that ELM predicted FCG values are displaying a more downward tendency in the highest stress level 225 MPA, whereas for this latter stress level, RBFN fit the experimental data better. ELM fit well the data for the lowest stress levels. Figure 21 (b) and 22 (b) display similar predicted surfaces for both ANNs, nevertheless, RBFN seems to fit well the trend of the experimental data. For figures 21 (c) and 22 (c) the results are similar with a downward tendency for RBFN towards the highest

stress level of 105 MPa, which agrees better with the experimental data. Finally, Figures 21 (D) and 22 (D) show that ELM has a downward tendency which agrees with the experimental data and an upward tendency for RBFN. As seen from Figures 21 and 22, both ANN methods show good predictions of small FCG rate for all stress ratios. As noticed before, RBFN matches the experimental data better than ELM for a fairly wide range of stress levels. However, the differences between the predictions and the experimental data are very small and both methods seem to be generally accurate.

The corresponding 2D graphs of 2024-T3 aluminum alloy at different stress ratios and a wide range of stress levels (50 MPa to 225 MPa) for both RBFN and ELM are plotted in Figure 23 and 24 respectively.

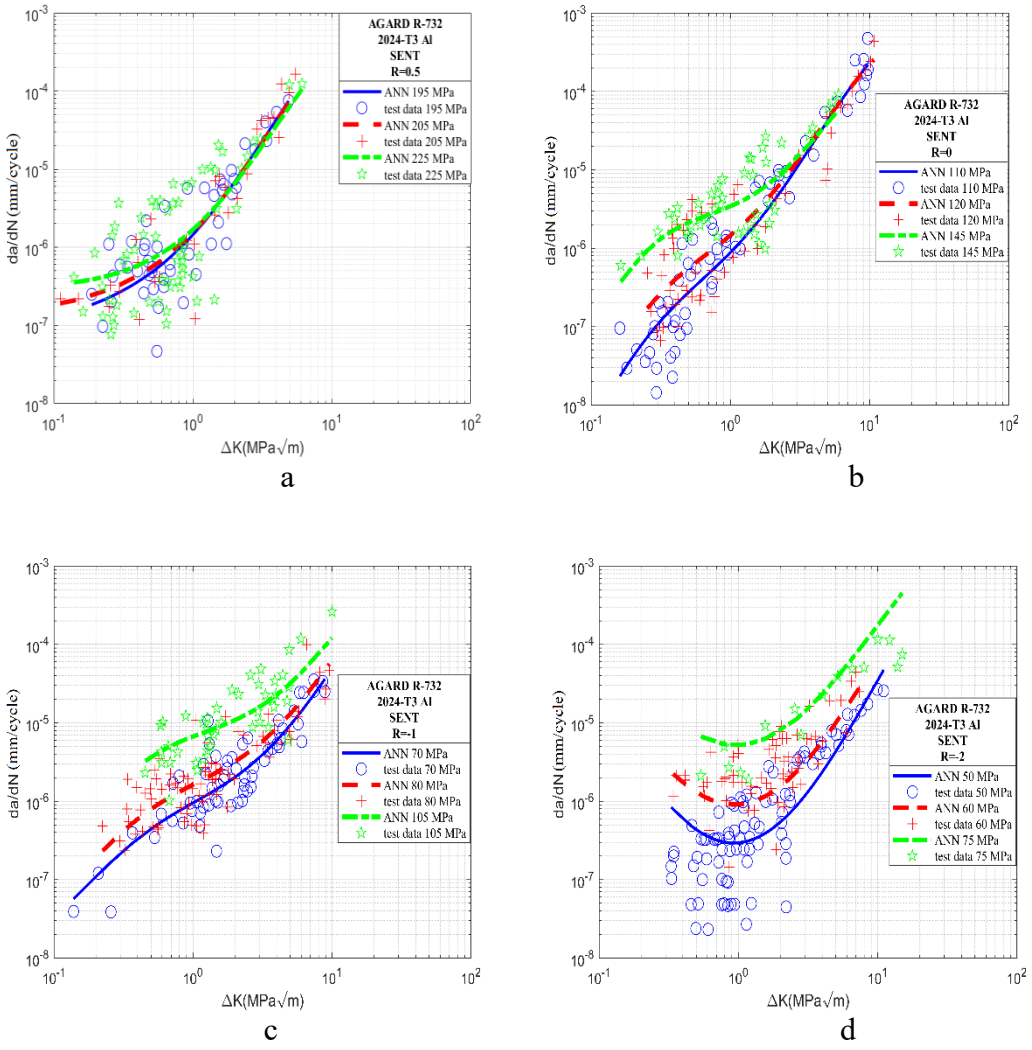

Figure 23 The predicted curves by RBFN with experimental data of 2024-T3 aluminum alloy: (a) R=0.5; (b) R=0; (c) R=-1; and (d) R=-2

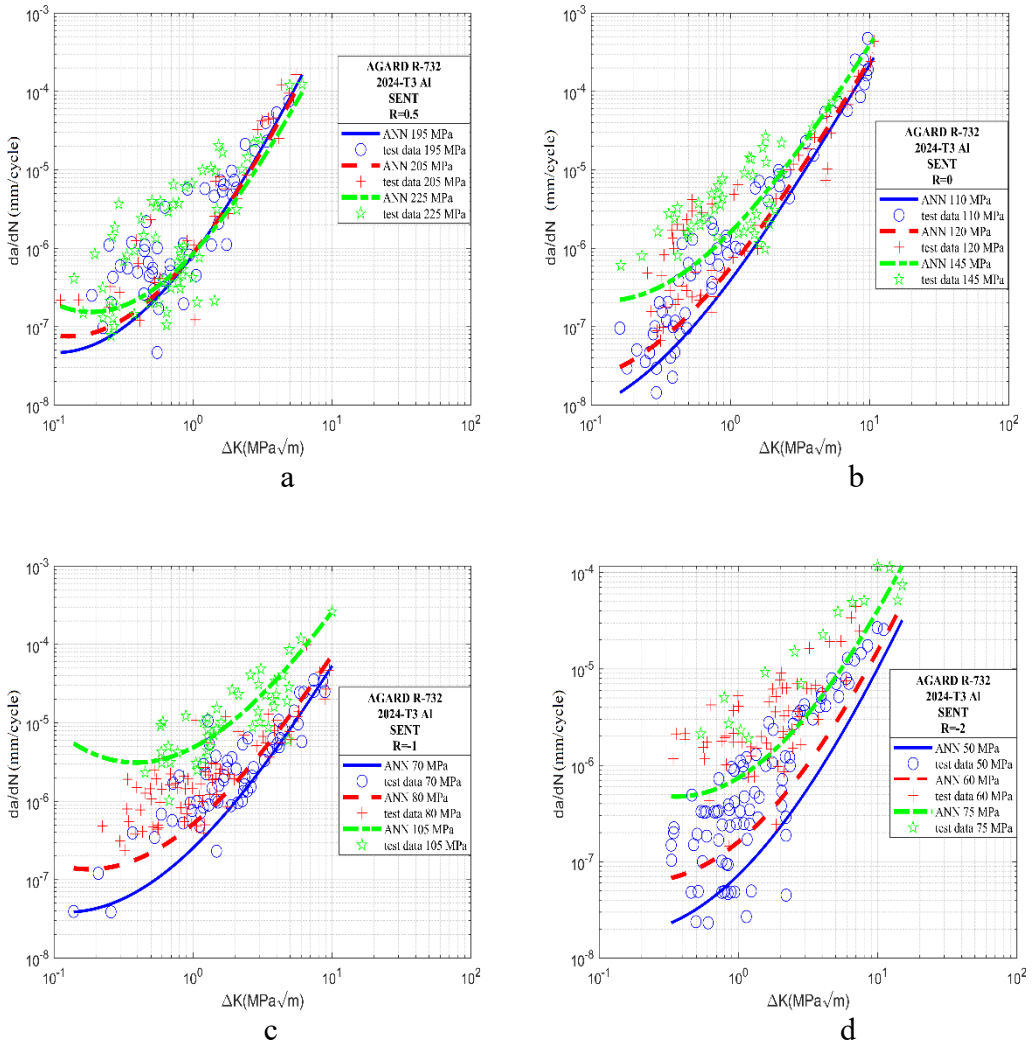

Figure 24 The predicted curves by ELM with experimental data of 2024-T3 aluminum alloy: (a) R=0.5; (b) R=0; (c) R=-1; and (d) R=-2

The predicted curves of both ANNs match the experimental data of each stress ratio and results are very similar in figures 23 (a) and 24 (a) and figures 23 (b) and 24 (b). Figures 23 (c) and 24 (c) are also similar, however, it can be noticed that ELM FCG predictions are beyond the experimental ΔK range. This illustrates the extrapolation ability of ELM compared to RBFN. In Figure 24 (d), which presents ELM results for R=-2, it can be seen

that the predictions do not accurately fit the experimental data especially for the lowest stress levels (50 MPa and 60 MPa). The reason for this is the fact that the ELM algorithm was not trained for R=-2 data, since only 70% of the experimental data was used for training and the rest was used for testing without prior knowledge of the output. Though the discrepancies between the ELM predictions and the experimental data, the ELM predictions still follow the trend of experimental data on the testing part.

Overall, results from ANNs on 2024-T3 aluminum alloy for different stress levels agreed well with the experimental data. The use of ANNs for small fatigue crack growth is validated for 2024-T3 aluminum alloy for different stress ratios and stress levels although the lack of experimental data to feed to ANNs. However, relying on these plots is not sufficient for any conclusions regarding the comparison between the two methods. The following section will present an error analysis that will allow a proper comparison between ELM and RBFN methods.

2. Aluminum-lithium alloy 2090-TBE41

Test data of 2090-TBE41 aluminum-lithium alloy at three stress ratios (R=0, R=-1, and R=-2) and a fairly widespread range of stress ratios (ranging from 55 MPa to 170 MPa) were employed for FCG analyses. Both RBFN and ELM methods were used for this purpose. As previously mentioned, the experimental data was divided into 70% training and 30% testing data for both models. The same parameters used for 2024-T3 aluminum alloy were used for 2090-TBE41aluminum alloy and all the other materials in this work.

Figures 25 shows the experimental data with the ANN predictions by both methods in a 3D plot. Both figures show that both ANN predictions represented by empty circles symbols follow the behavior of the experimental data.

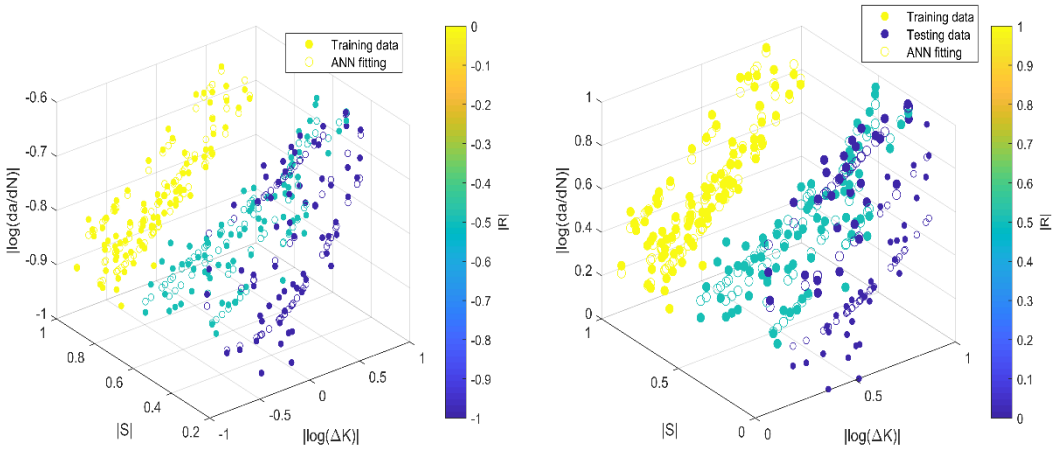

a b

Figure 25 3D representation of ANN fitting the experimental data of 2090-TBE41aluminum alloy at different R ratios: (a) RBFN (b) ELM

3D predicted surfaces by both ANNs for 2090-TBE41aluminum alloy are presented in Figure 26 and 27.

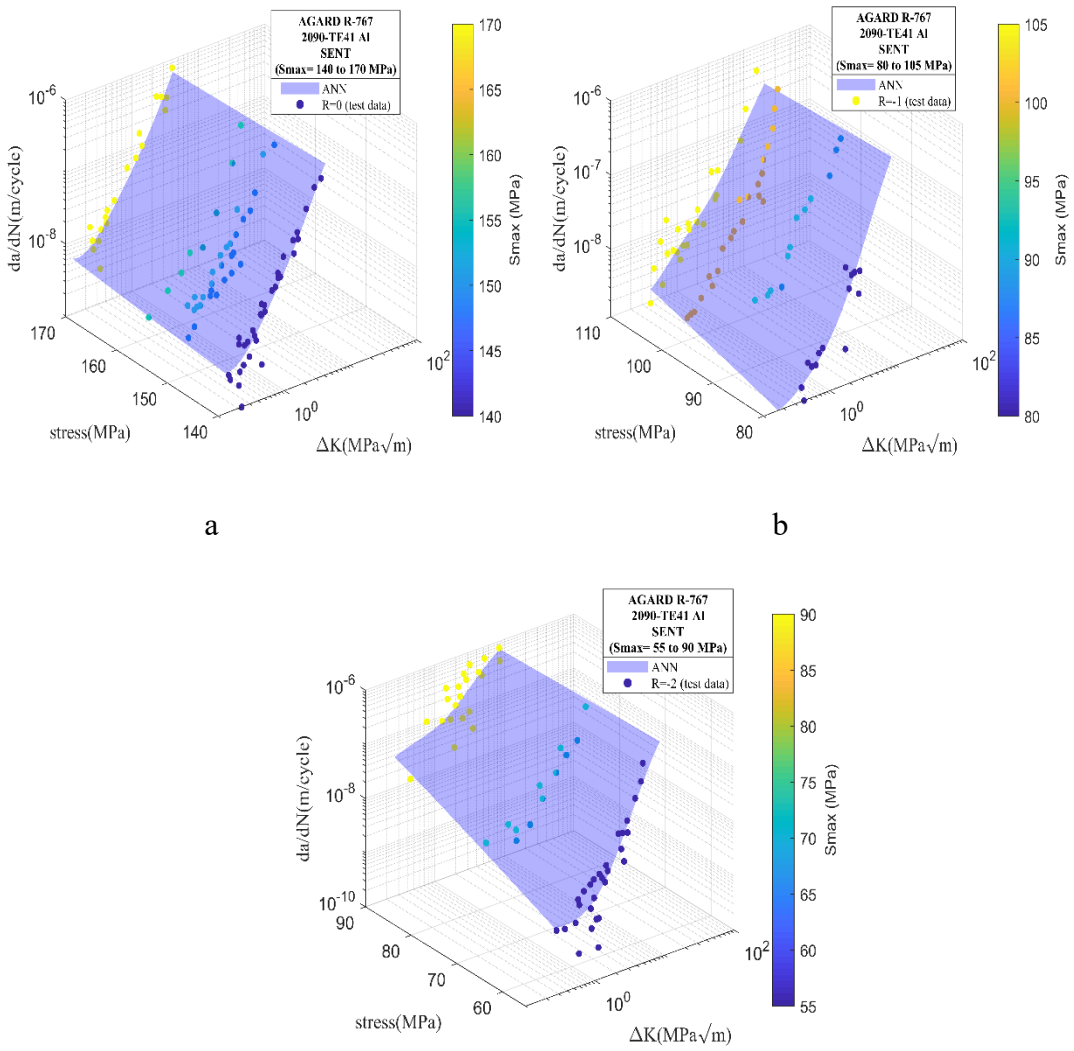

Figure 26 The predicted 3D surfaces by RBFN of 2090-TBE41aluminum alloy: (a) R=0; (b) R=-1; and (c) R=-2

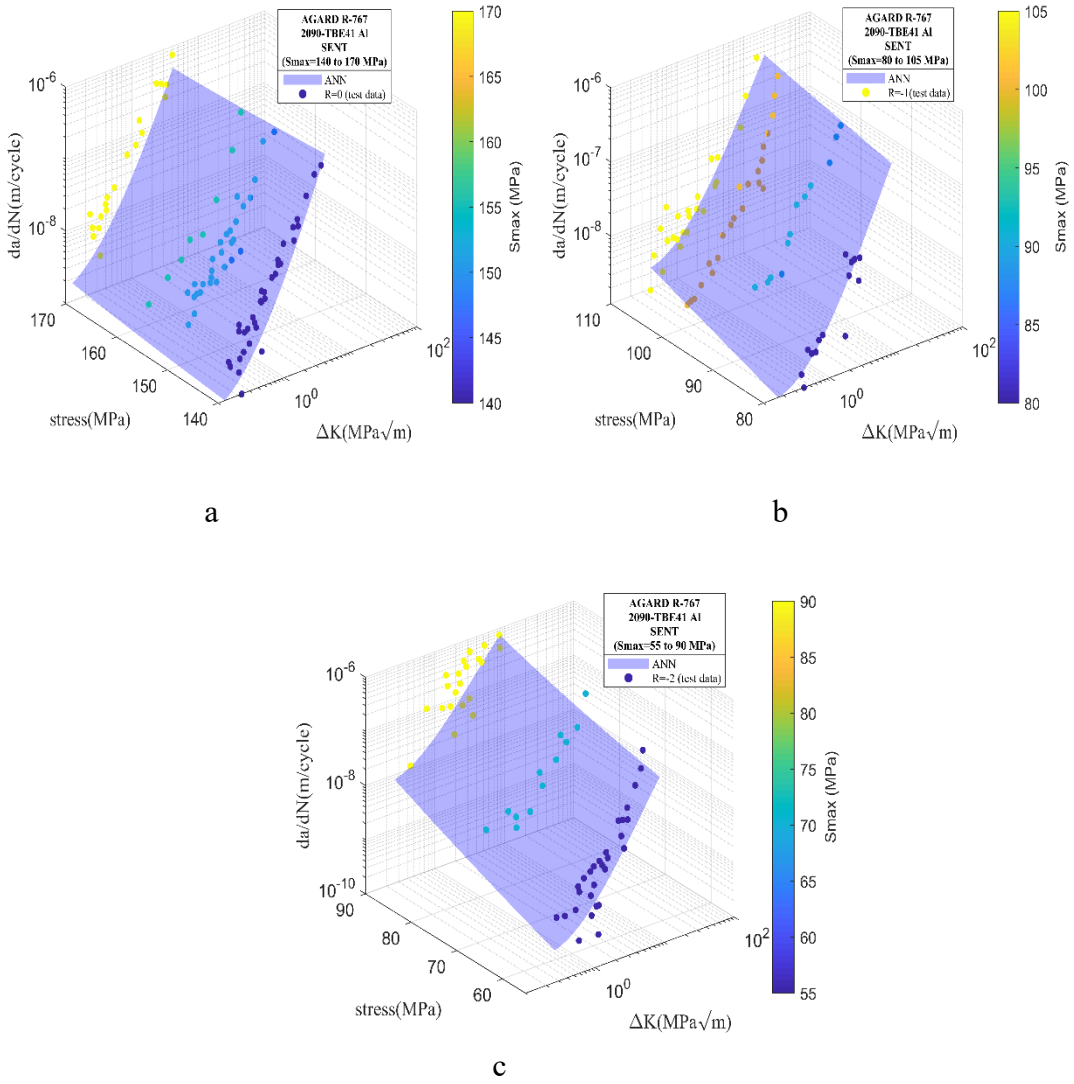

Figure 27 The predicted 3D surfaces by ELM of 2090-TBE41 aluminum alloy: (a) R=0; (b) R=-1; and (c) R=-2

Figure 26 (a) and Figure 27 (a) show that both ELM and RBFN predicted surfaces are smooth and follow the trend of the experimental data, however, RBFN shows an upward tendency that does not agree with the experimental data. It is also noticed that for the highest stress level 170 MPa, RBFN predictions agree better with experimental data. Results shown in Figure 26 (b) and 27 (b) display similar predicted surfaces for both ANNs.

The last stress ratio results shown in Figures 26 (c) and 27 (c) that RBFN has an exaggerated upward tendency contrary to ELM. This latter agrees more with the experimental data and shows some extrapolation capacities beyond the ΔK range. The predicted surface for the last stress ratio R=-2 is an extrapolation of the algorithm since it was not used during the training phase. Generally, both ANNs presented good small fatigue crack growth rate predictions for all of the stress ratios (R=0, R=-1, and R=-2) for this material.

The equivalent 2D graphs of 2090-TBE41aluminum alloy with different stress ratios for both RBFN and ELM are presented in Figure 28 and 29.

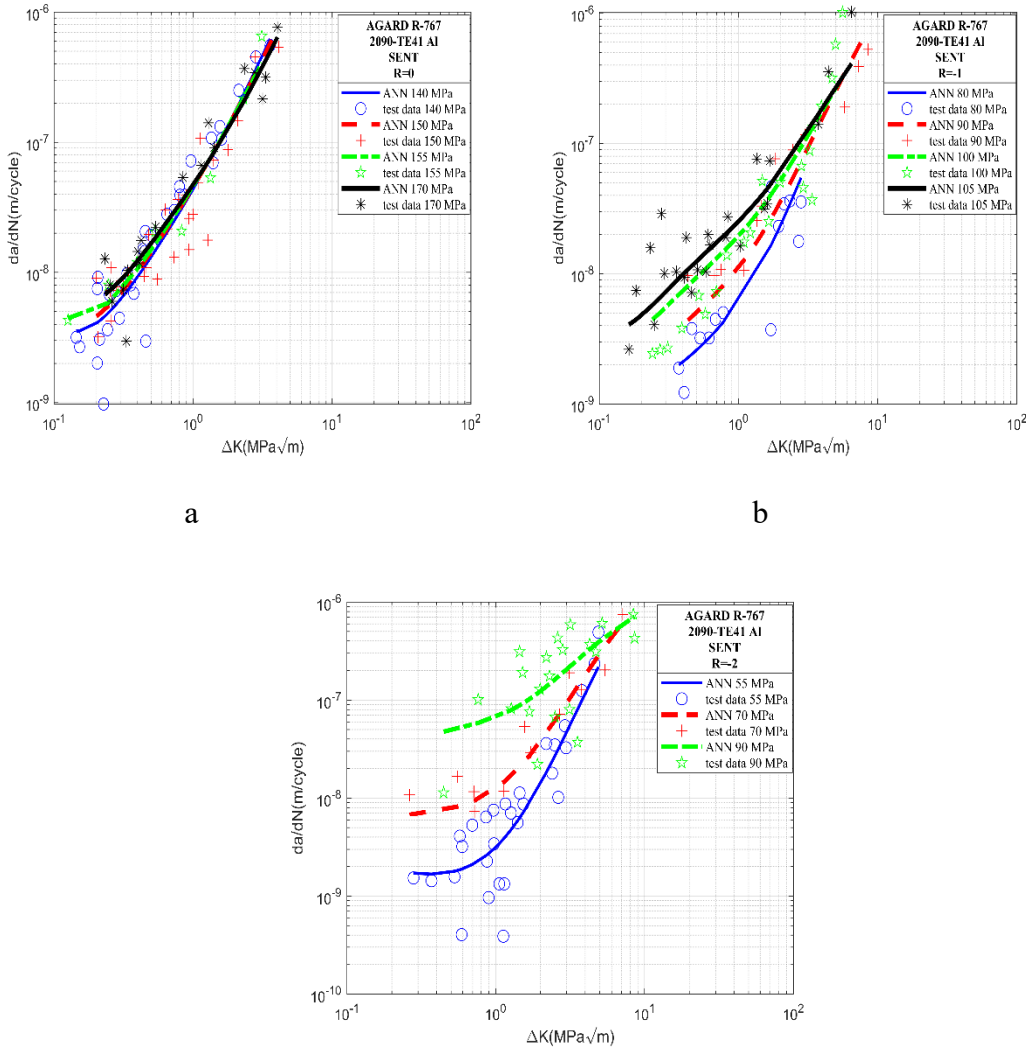

Figure 28 The predicted curves by RBFN with experimental data of 2090-TBE41aluminum alloy: (a) R=0; (b) R=-1; and (c) R=-2

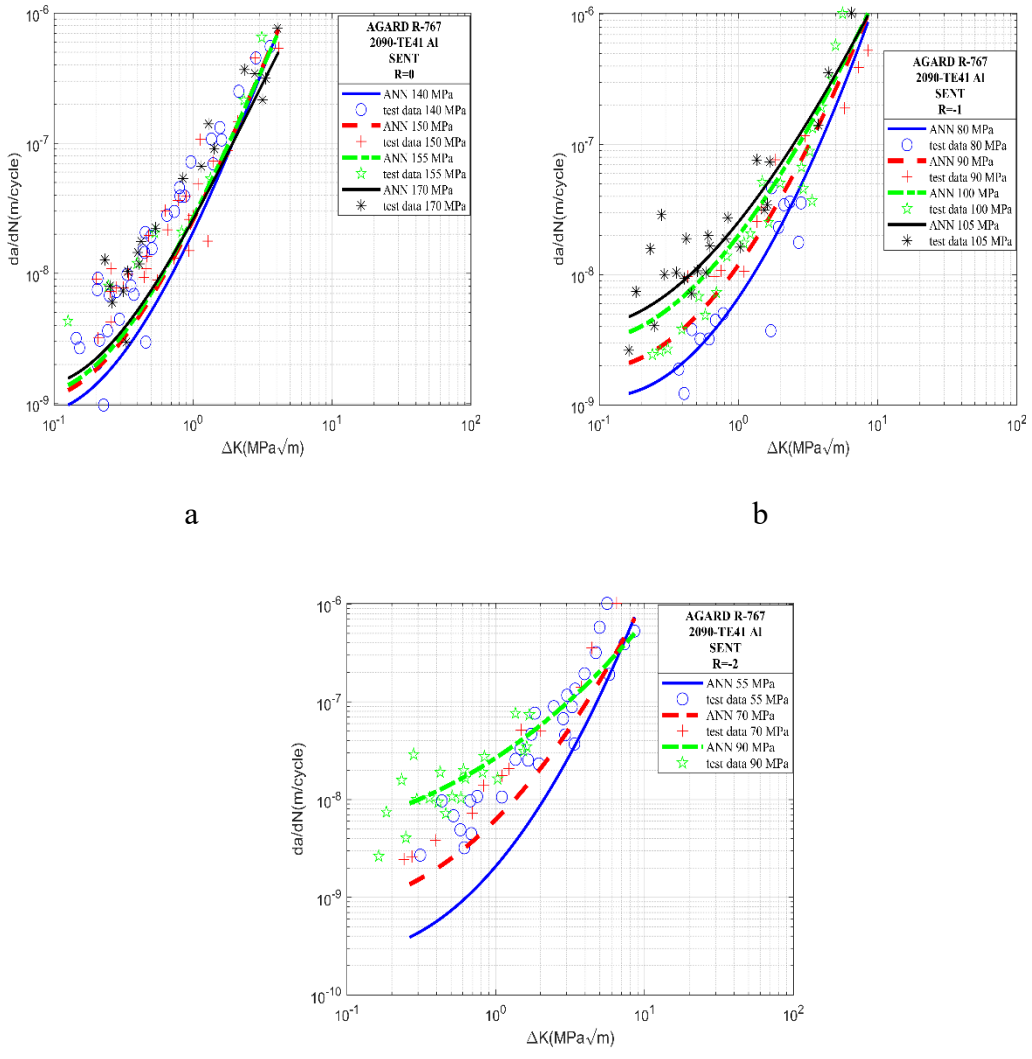

Figure 29 The predicted curves by ELM with experimental data of 2090-TBE41aluminum alloy: (a) R=0; (b) R=-1; and (c) R=-2

The RBFN predicted curves in Figure 28 (a) fit well the experimental data as was shown previously in the 3D surface. Figure 29 (b) displays that ELM matches the experimental data more accurately while going slightly beyond the ΔK range for R=-1 for each stress level (80 MPa, 90 MPa, 100 MPa, and 105 MPa). For the last stress ratio R=- 2, Figure 28 (c) shows that RBFN provides very accurate predictions contrary to ELM results

shown in Figure 29 (c). This was attributed to the fact that the algorithm was not trained for the stress ratio of R=-2. The predictions however do have a coherent behavior which shows that ELM predictions are still acceptable. As mentioned before, it can be concluded from these plots that ELM extrapolates based on the trend of the experimental data better than the RBFN when the predicted curves are beyond the ΔK ranges of experimental data.

Results from both ANNs on 2090-TBE41aluminum alloy at different stress ratios (R=0, R=-1, and R=-2) and stress levels (S_{max}=50 to 170 MPa) fit well the experimental data which demonstrates that ANNs use for small fatigue crack growth is valid.

3. Aluminum alloy LC9cs

LC9cs aluminum alloy test data were used to conduct FCG analyses. Three stress ratios (R=0.5, R=0, and R=-1) and few stress levels were applied. The experimental data was divided into 70% training data and 30% testing data. The same parameters used for previous materials were used for LC9cs aluminum alloy.

Figures 30 displays two 3D plots representing the experimental data with the ANN predictions for each ANN method. This Figure shows that ELM and RBFN predictions (empty circles symbols) follow the behavior of the test data's small crack growth rate.

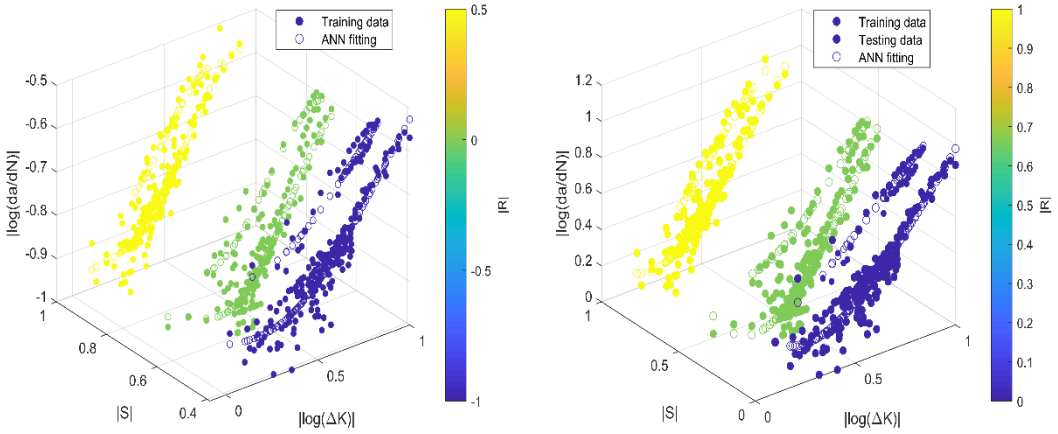

a b

Figure 30 3D representation of ANN fitting the experimental data of LC9cs aluminum alloy at different R ratios: (a) RBFN (b) ELM

Figure 31 and 32 exhibit the 3D predicted surfaces by both ANNs for LC9cs aluminum alloy at different R ratios using a limited experimental data set.

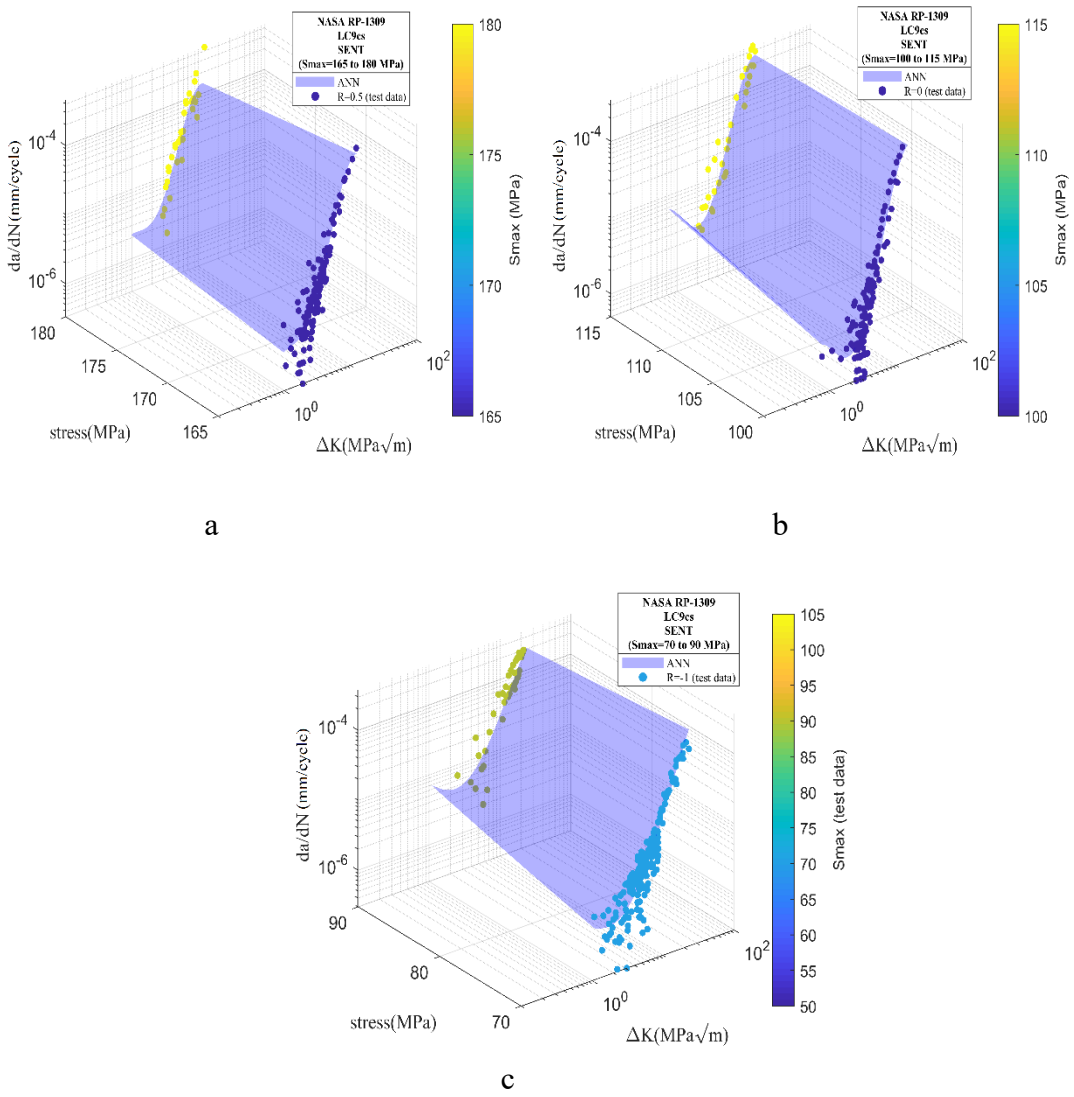

Figure 31 The predicted 3D surfaces by RBFN of LC9cs aluminum alloy: (a) R=0.5; (b) R=0; and (c) R=-1

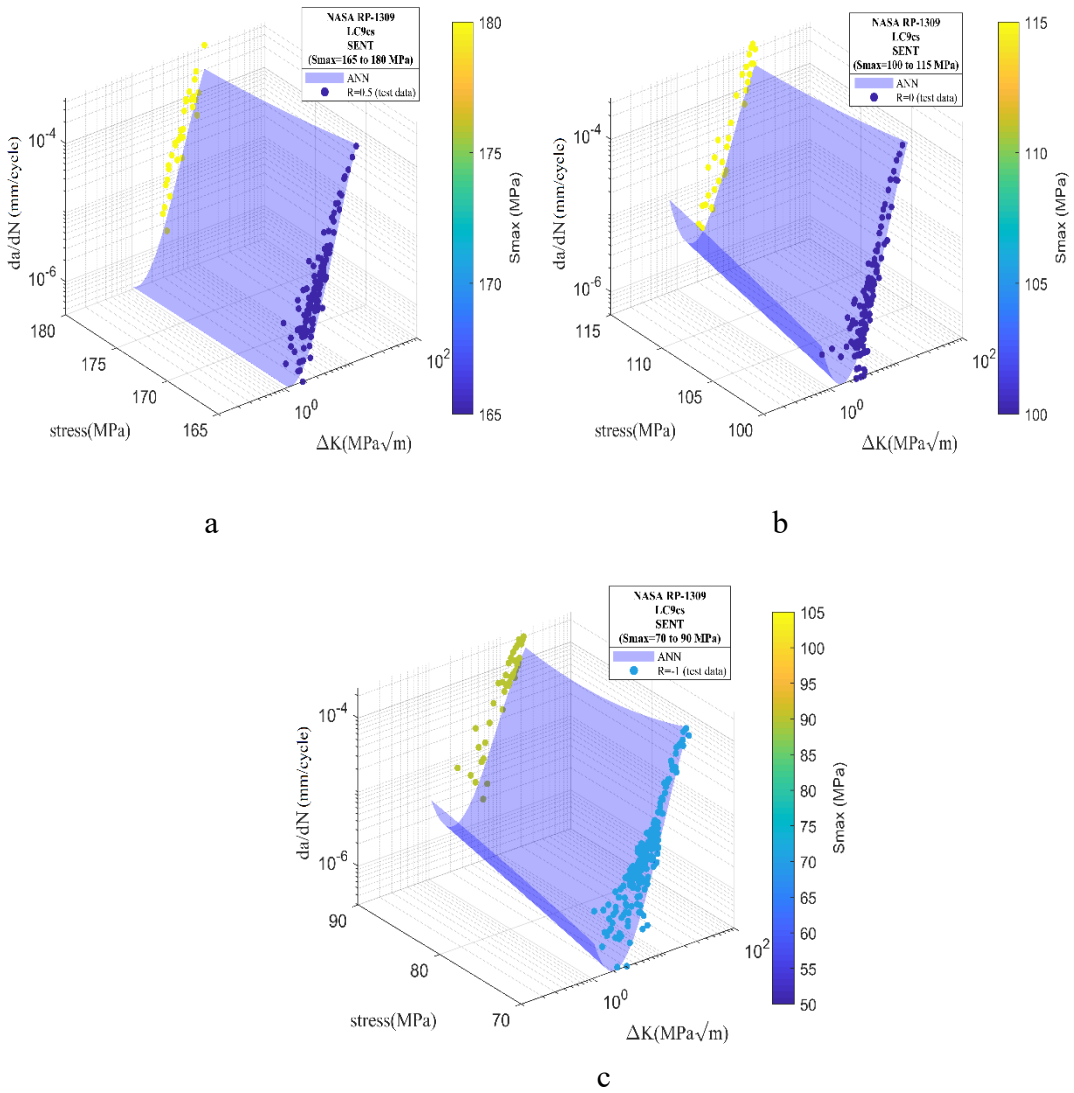

Figure 32 The predicted 3D surfaces by ELM of LC9cs aluminum alloy: (a) R=0.5; (b) R=0; and (c) R=-1

Figure 31 (a) and Figure 32 (a) show that ELM predicted surface agrees better than RBFN with the tendency of the experimental data for R=0.5. It is also noticed that ELM can slightly extrapolate beyond the range of data for the highest stress level. Figure 32 (b) show that ELM predicted surface has an exaggerated upward tendency which does not agrees with the test data trend, whereas Figure 31 (b) displays a more reasonable surface

for R= 0. The last plot for R=-1 represented in Figure 31 (c) and Figure 32 (c) show that both ELM and RBFN yield similar and reasonable results.

Figure 33 and 34 represent 2D plots s of LC9cs aluminum alloy at different stress ratios (R=0.5, R=0, and R=-1) for both RBFN and ELM methods.

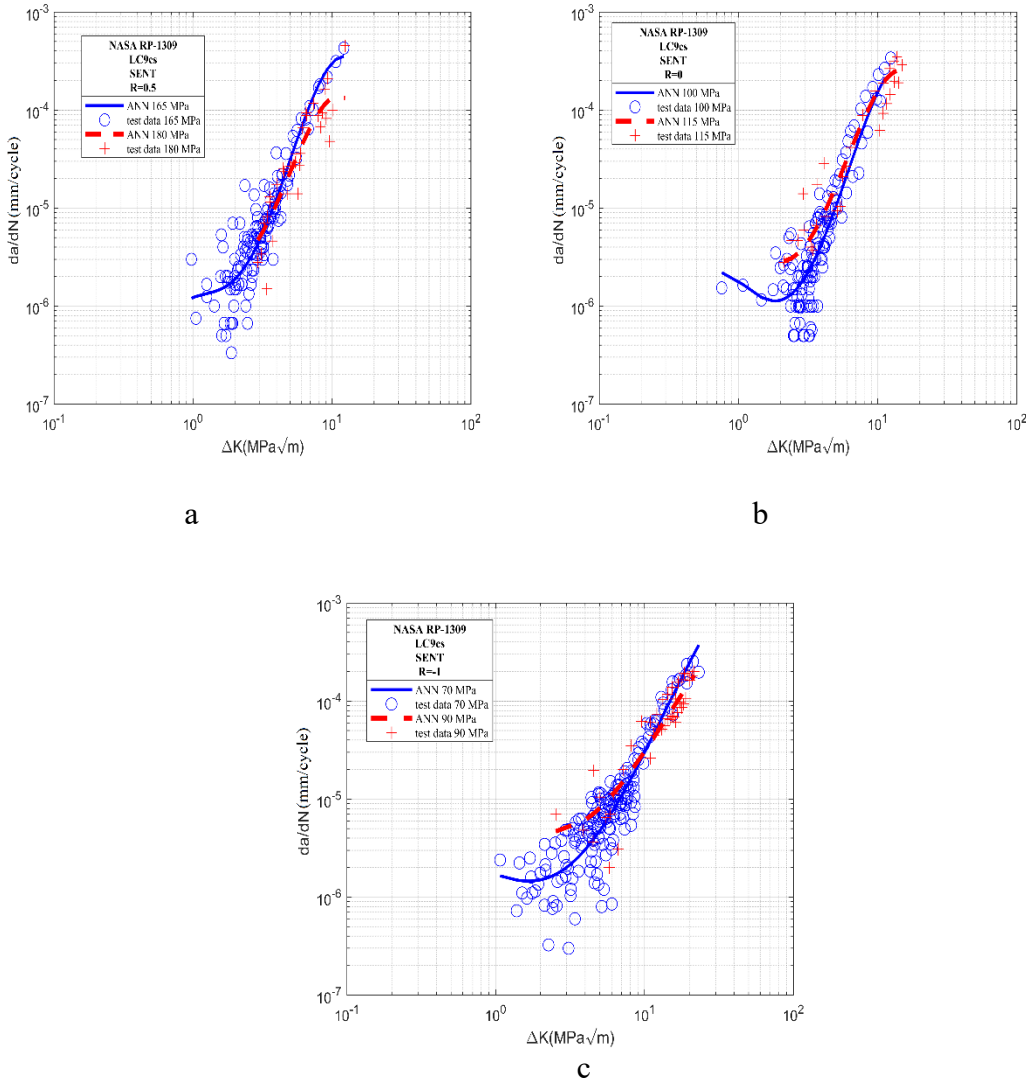

Figure 33 The predicted curves by RBFN with experimental data of LC9cs aluminum alloy: (a) R=0.5; (b) R=0; and (c) R=-1

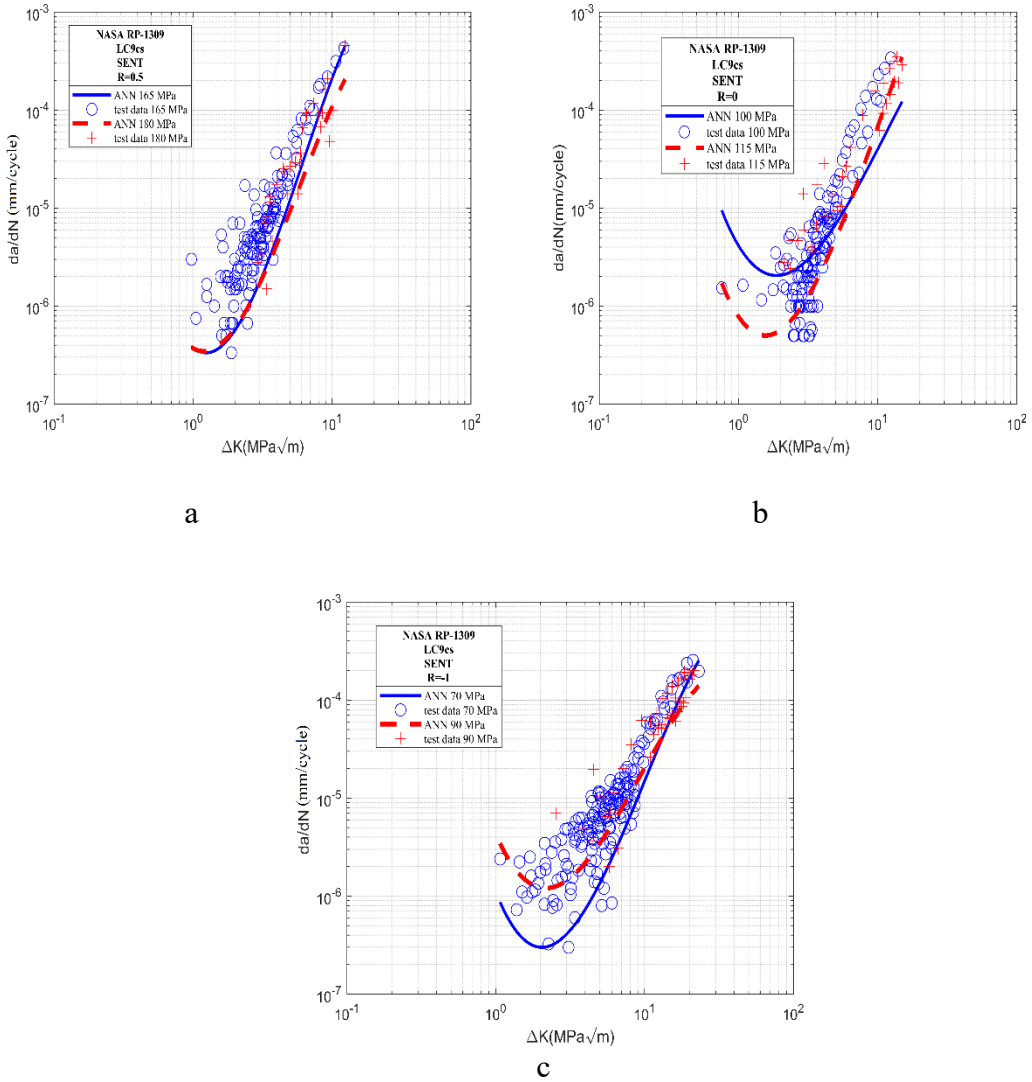

Figure 34 The predicted curves by ELM with experimental data of LC9cs aluminum alloy: (a) R=0.5; (b) R=0; and (c) R=-1

The precited 2D curves for both RBFN and ELM fit well the experimental data with a higher ability of extrapolation for ELM at R=0. Results from both ANNs on LC9cs aluminum alloy for different stress levels ranging from 50 MPa to 180 MPa fit well the experimental data even with a limited experimental data set provided to train the ANNs.

Large amount of training data is important in making the ANN models work efficiently. The lack of data was behind the choice of feeding the ANNs models with three variables and hence accomplishing a 3 input 1 output system. Unavailable small crack data bases such as the case for LC9cs aluminum alloy reduces the predictive accuracy of the ANN models which was the case for ELM, as can be observed from the 2D plots. The abnormal upward behavior of ELM could be explained by the lack of FCG data for this material. The ELM method must have been influenced by the previous results and previous trainings. In the future, more research needs to be performed to fix this issue.

4. Aluminum alloy 7075-T6

Experimental test data of 7075-T6 aluminum alloy at three stress ratios (R=0.5, R=0, and R=-1) and a small range of stress levels were used to conduct FCG analyses.

3D plots displaying the experimental data with the ANN predictions for ELM and RBFN methods are shown in Figure 35.

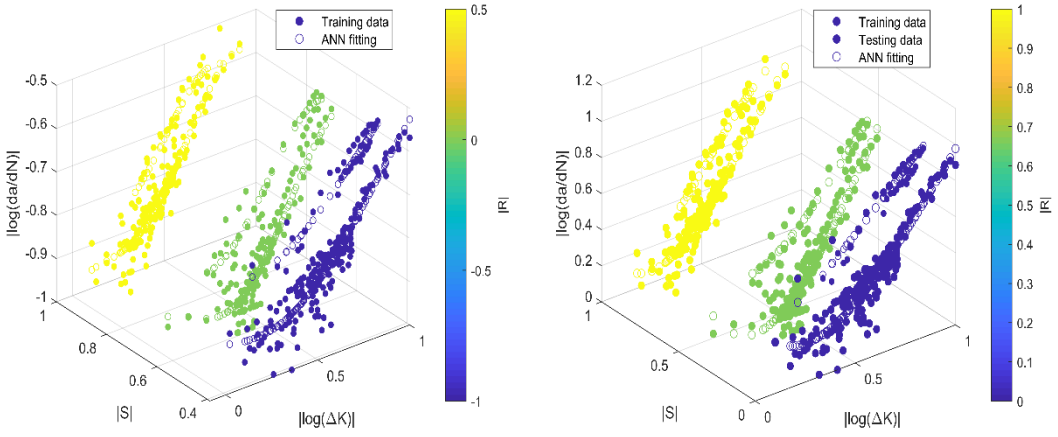

a b

Figure 35 3D representation of ANN fitting the experimental data of 7075-T6 aluminum alloy at different R ratios: (a) RBFN (b) ELM

Figure 35 shows that RBFN and ELM suit the trend of the experimental data's small crack growth rate. Figure 36 and 37 show the 3D predicted surfaces by both ANNs for 7075-T6 aluminum alloy at different R ratios (R=0.5, R=0, and R=-1).

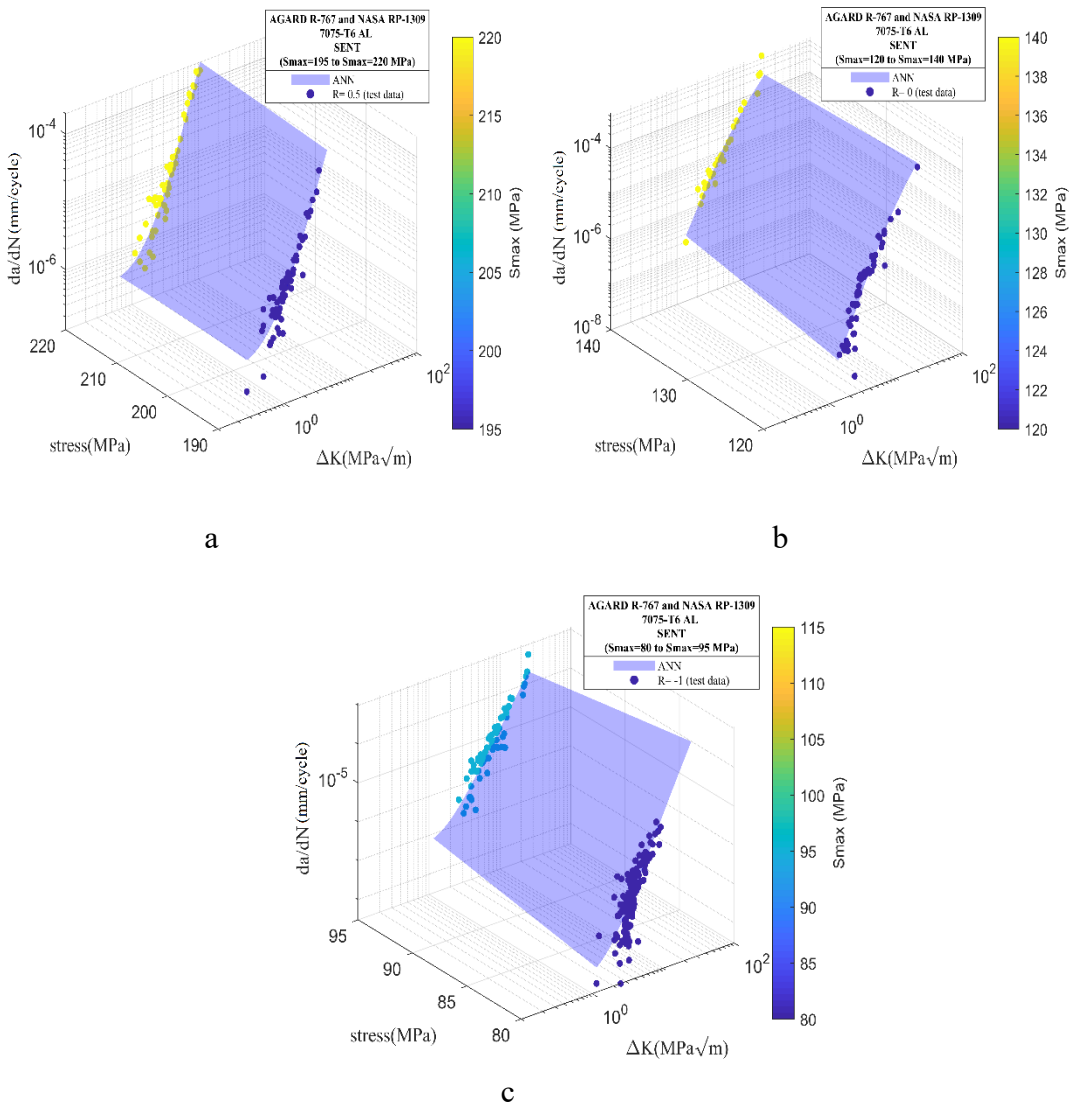

Figure 36 The predicted 3D surfaces by RBFN of 7075-T6 aluminum alloy: (a) R=0.5; (b) R=0; and (c) R=-1

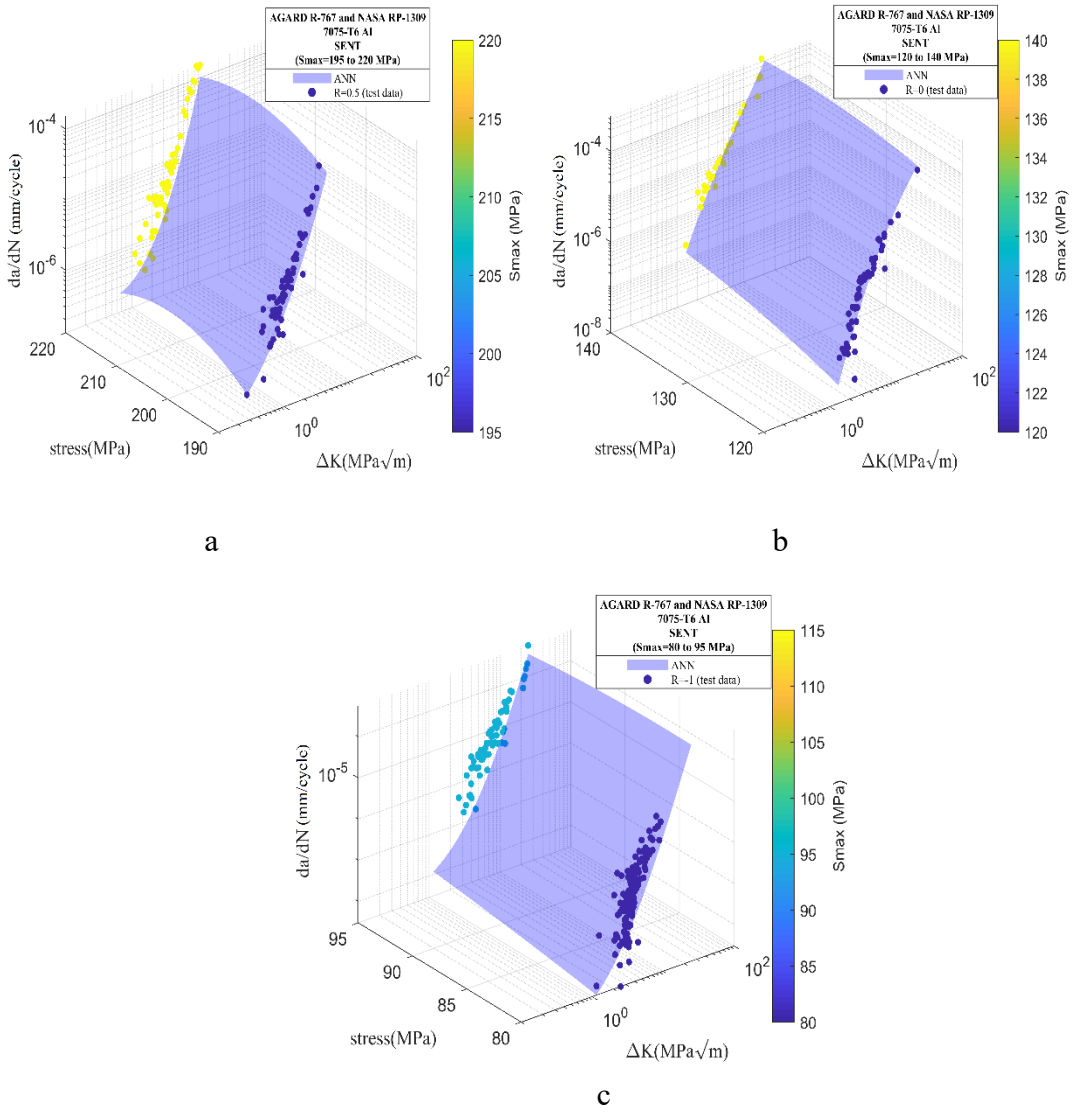

Figure 37 The predicted 3D surfaces by ELM of 7075-T6 aluminum alloy: (a) R=0.5; (b) R=0; and (c) R=-1

Figure 36 (a) and Figure 37 (a) show that ELM predicted surface fits the experimental data better than RBFN. The same observation can be seen for R=0.5 and R = - 1 represented by Figures 36 (b) and 37 (b) and Figures 36 (c) and 37 (c)

respectively. RBFN and ELM predicted surfaces show that both methods fit the experimental data well and give reasonable interpolations predictions with slightly better results for ELM.

Figure 38 and 39 display the corresponding 2D graphs of 7075-T6 aluminum alloy at different stress ratios (R=0.5, R=0, and R=-1) for the two methods: RBFN and ELM.

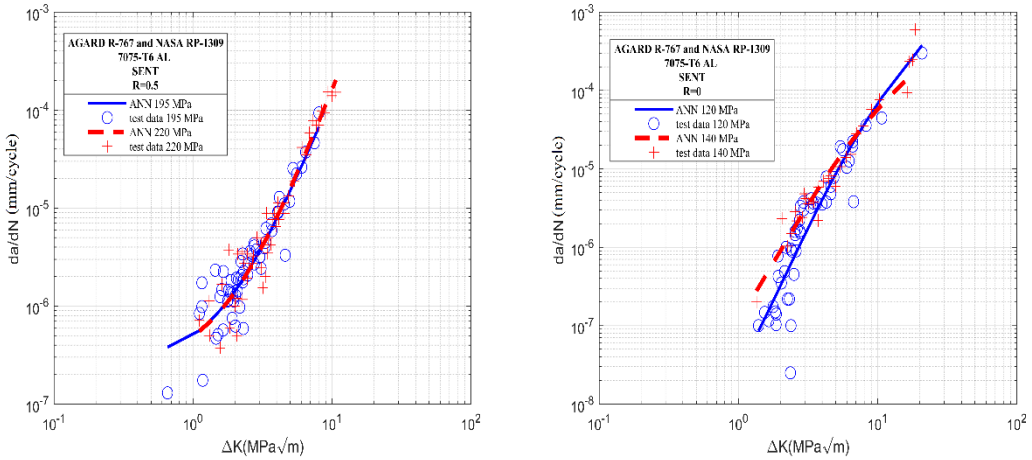

a b

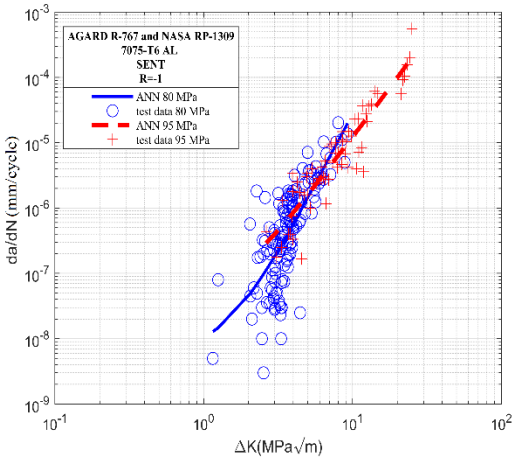

c

Figure 38 The predicted curves by RBFN with experimental data of 7075-T6 aluminum alloy: (a) R=0.5; (b) R=0; and (c) R=-1

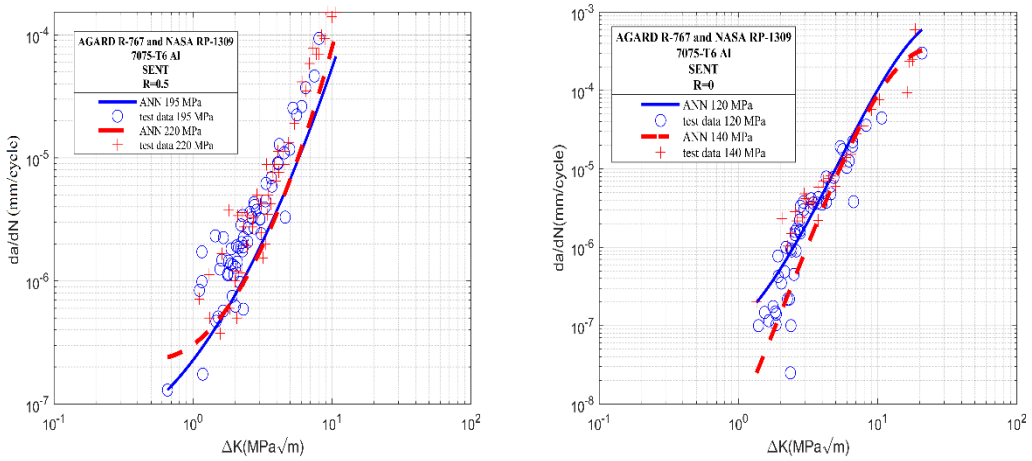

Figure 39 The predicted curves by ELM with experimental data of 7075-T6 aluminum alloy: (a) R=0.5; (b) R=0; and (c) R=-1

The precited 2D curves for both RBFN and ELM show overall similar results. The predicted FCG ratios fits the experimental FCG data with a higher ability of extrapolation for ELM.

5. Titanium alloy Ti-6Al-4V

Ti-6Al-4V titanium alloy experimental test data at two stress ratios R=0.1 and R=-1, and a varied range of stress levels ranging from 210 to 690 MPa were used to conduct FCG analyses based on ANNs.

Figures 40 shows the experimental data along with the ANN predictions for ELM and RBFN methods. Both 3D plots render anew that both ANNs (empty circles symbols) output good results that fit the experimental data.

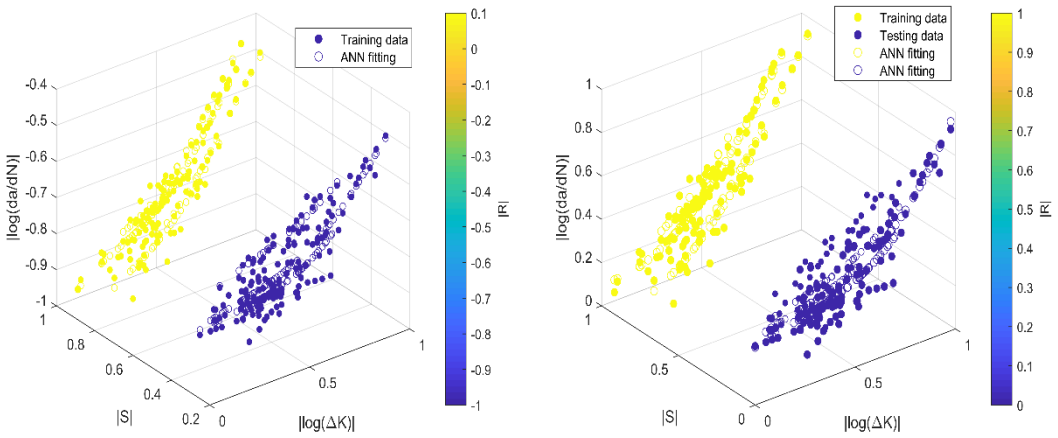

a b

Figure 40 3D representation of ANN fitting the experimental data of Ti-6Al-4V titanium alloy for two R ratios: (a) RBFN (b) ELM

Figure 41 and 42 display the 3D predicted surfaces by both RBFN and ELM for Ti-6Al-4V titanium alloy at the two ratios R=0.1and R=-1. The two ANNs produced smooth surfaces that fit the experimental data well although the limited data set. Surfaces for R=0.1 for both ANNs shown in Figures 41 (b) and 42 (b) show the predictions for the ELM were not accurate near the threshold region for the highest stress level. Generally,

similar results are noticed for both ELM and RBFN for both stress ratios. In order to increase the predictions accuracy for both methods, a larger set of experimental data is needed.

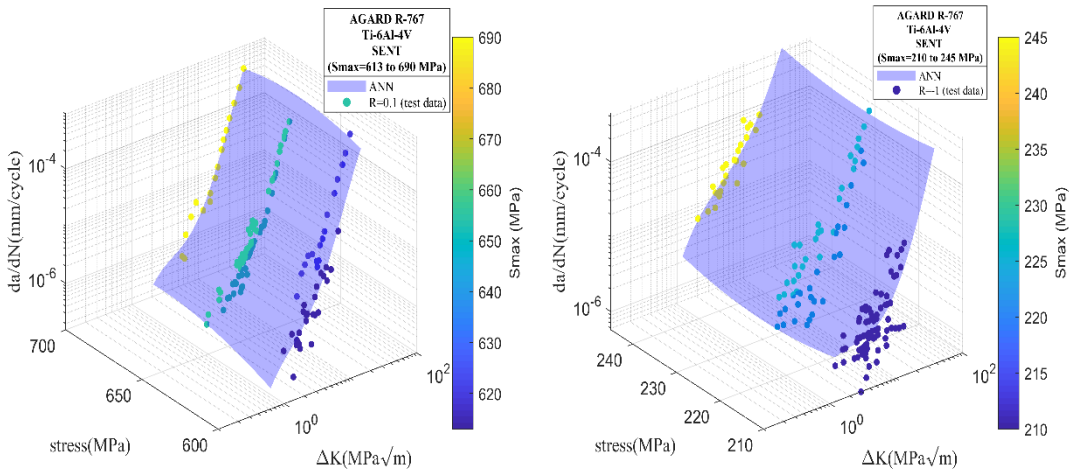

a b

Figure 41 The predicted 3D surfaces by RBFN of Ti-6Al-4V titanium alloy: (a) R=0.1; (b) R=-1

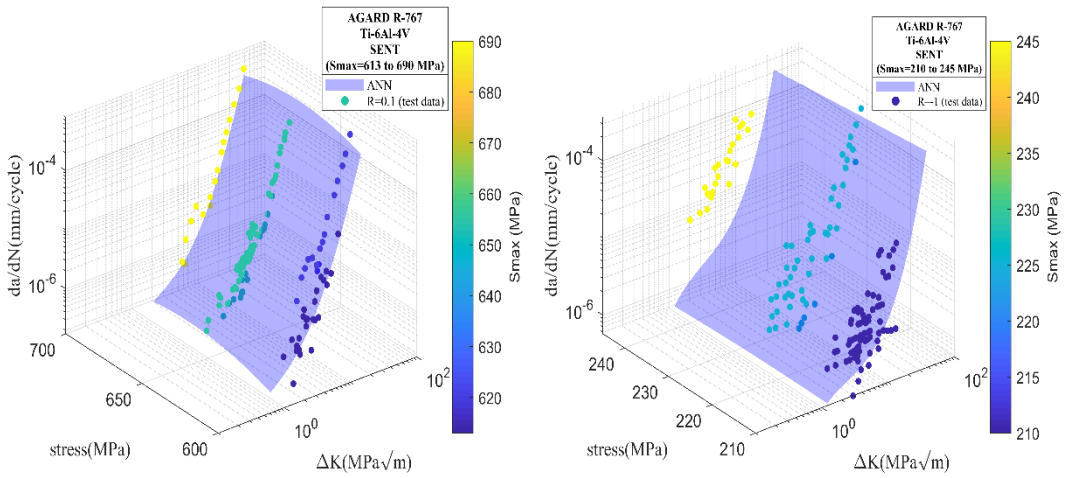

a b

Figure 42 The predicted 3D surfaces by ELM of Ti-6Al-4V titanium alloy: (a) R=0.1; (b) R=-1

Figure 43 and 44 show the 2D plots that corresponds to the previous ELM and RBFN 3D plots of Ti-6Al-4V titanium alloy at R=0.1 and R=-1.

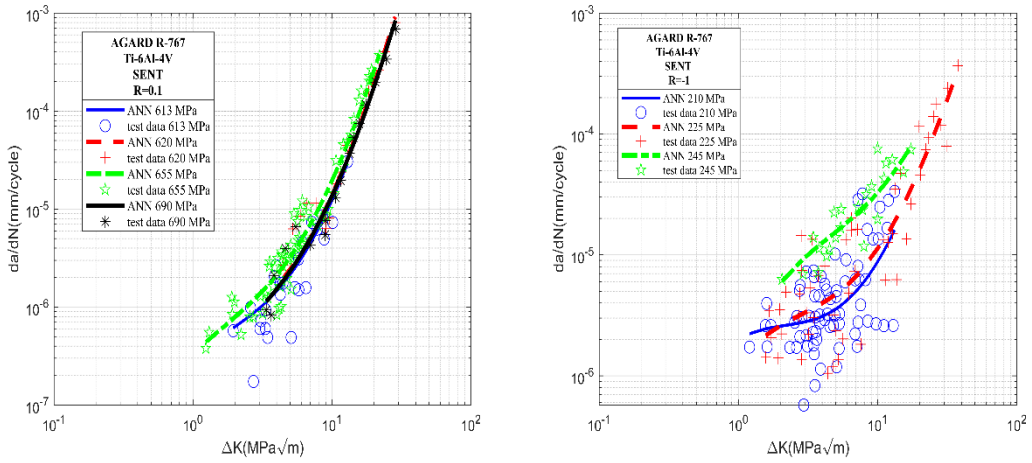

a b

Figure 43 The predicted curves by RBFN with experimental data of Ti-6Al-4V titanium alloy: (a) R=0.1; (b) R=-1

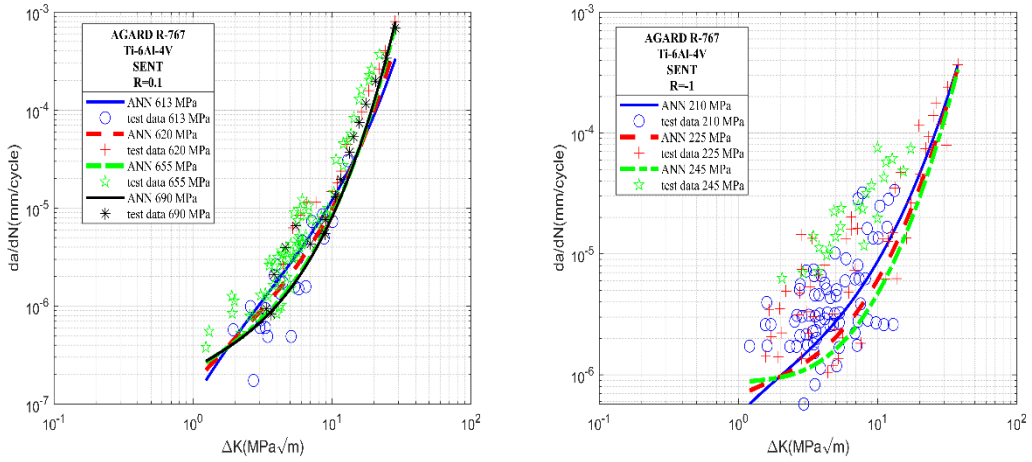

a b

Figure 44 The predicted curves by ELM with experimental data of Ti-6Al-4V titanium alloy: (a) R=0.1; (b) R=-1

Figures 43 (a) and Figure 44 (a) show that RBFN fit the experimental data better than ELM. ELM does however extrapolate beyond the ΔK range for the highest stress levels at both R ratios. For the stress ratio R=-1, shown in Figures 43 (b) and 44 (b) RBFN results were more accurate than those of ELM and that is due to the fact that ELM has not trained for these last stress levels: 210 MPa, 225 MPa, and 245 MPa.

CHAPTER V

RESULTS AND DISCUSSION

In small crack problem, a full understanding of how various factors can influence the crack growth is an issue and a simple mathematical model that can give good predictions is hard to find. The ANNs using few parameters are capable of generalizing a function inside a subspace spanned by the training samples and with some methods like ELM even outside the subspace. The results for all materials show that the built model not only fits the training data well but also generalizes on test data. Results also showed that the ELM is capable of extrapolating beyond the experimental data range. Both ANNs are capable of predicting FCG rate using experimental data sets of the small crack regime.

The three-input/one-output model makes the lack of data less problematic since ANNs are capable of learning information from different R ratios, ΔK range, and stress levels. Numerous materials (2024-T3, 7075-T6, 2090-TBE41, LC9cs aluminum alloys, and Ti-6Al-4V titanium alloy) were used in this work to validate the models and support the use of ANNs as accurate methods to correlate and to predict fatigue small crack growth. Results for both RBFN and ELM clearly showed excellent fitting abilities and predictions fell very close to experimental data. However, for materials with few experimental data available, such Ti-6Al-4V titanium alloy further study is required to develop a model capable of giving more accurate predictions. The lack of experimental data and material databases was a key issue encountered during this study.

Although there were discrepancies between both methods in some materials, the predictions were overall similar, making both methods good candidates for use in fatigue crack growth predictions. ELM, however, remains faster than RBFN and only has few training parameters that do not need to be tuned iteratively. Overall, ELM was shown to have excellent global optimization and extrapolation ability. This study demonstrates that although the ANN method fits well the fatigue small crack growth rates and gave good predictions even beyond the experimental range, the performance of these methods is still dependent on the sufficiency of the experimental data. In fact, the results were more accurate for materials where there was a higher data density. Consequently, a larger database for small cracks needs to be publicly available for future studies to improve the reliability and effectiveness of ANNs methods.

All results in the previous chapter established that ANNs can be utilized to predict the fatigue crack growth behavior of many materials with one single model even for a difficult problem such as small cracks. Predictions relying on a wide set of experimental data are reliable without resorting to further experimental analyzes for each material individually. ANNs are hence simple methodologies that proved to be very consistent and efficient in predicting fatigue crack growth of small cracks.

In regression problems plotting helps in viewing the overall trend of the data, but it is not an accurate way to assess the performance of models and compare their efficiency.

In order to compare the performance of each ANN and assess the model prediction capabilities, the mean squared error MSE is calculated for both RBFN and ELM. The MSE measures the average squared difference between the predicted FCG rate and the

experimental FCG rate to assess the quality of estimation of methods as described in equation 12.

$$MSE = \frac{1}{n}\sum_{i=1}^{n}(y_i - Y_i)^2 \quad (12)$$

With n being the number of data points, y_i the experimental data point and Y_i the predicted value. The difference is squared so that negative and positive values do not cancel out. The MSE decreases as the algorithm is learning, the goal is to minimize the error to provide the best predictions. This method is used as a default metric to evaluate the performance of regression algorithms in artificial neural networks.

The cumulative MSE was calculated for both methods and each material. The results are summarized in Table 6.

Table 6 Mean squared error analysis of RBFN and ELM for each material

MSE	2024-T3 Al	2090-TBE41 Al	LC9cs Al	7075-T6 Al	Ti-6Al-4V
MSE_{RBFN}	7.44e-10	8.94e-15	5.81e-10	8.54e-10	1.62e-10
MSE_{ELM}	3.22e-10	1.28e-14	4.95e-10	2.55e-9	1.31e-10

For a maximum number of fifteen neurons and an MSE goal of 0 for RBFN and ELM methods, the MSE was calculated and values closer to zero are optimal. Table 6 shows that ELM has smaller MSE values for three materials: 2024-T3 aluminum alloy and Ti-6Al-4V titanium alloy. RBFN has a lower MSE compared to ELM for: 2090-TBE41 aluminum-lithium alloy, 7075-T6 aluminum alloy, and LC9cs aluminum alloy. This agrees with the observations from the plots presented in the previous section. The MSE was used as a metric to find the optimal number of neurons that fits the data. Minimizing the MSE being the ultimate goal, many trials were performed to reach these low values.

The MSE was used as a part of the error analysis part of this work to minimize the scatter of the FCG data and determine the appropriate ANN parameters to fit the experimental data precisely. To better visualize and compare the prediction accuracy of both RBFN and ELM methods, a fitted probability density function (PDF) is used. The PDF is a visual tool that can reveal the prediction accuracy of ELM and RBFN. This probability analysis will permit a good comparison of both ANN methods by revealing their prediction accuracy. The PDF is a statistical method that identifies the probability distribution for a variable (i.e., error). The graph is typically a normal bell curve where the area under the curve indicates the interval in which the variable will occur. The interval lies around the mean value μ and defined in terms of the standard deviation σ.

In this study, the PDF is used to determine prediction errors of the two ANNs: RBFN and ELM. The PDF measures the prediction error by performing the difference between the predicted crack growth rate $(da/dN)_p$ and the experimental crack growth rate $(da/dN)_e$ for a given data point as expressed in equation 13.

$$error_i = \frac{da}{dN}_i^p - \frac{da}{dN}_i^e \tag{13}$$

If the error is positive, the prediction is conservative and if the error is negative the prediction is non-conservative [31].

To study the effect of stress level on small crack growth, the PDF is plotted for all materials: 2024-T3 aluminum alloy, 2090-TBE41 aluminum-lithium alloy, LC9cs aluminum alloy, 7075-T6 aluminum alloy, Ti-6Al-4V titanium alloy. The PDF plots show prediction errors of the FCG rate for the two ANN methods (i.e. RBFN and ELM) for different stress levels and stress ratios: The PDF curves for ELM are represented by the

blue color marker while the PDF curves for RBFN are represented by the red color marker throughout the probability analysis.

Figure 45 shows the PDF prediction errors at the two different ANNs for 2024-T3 aluminum alloy at the four stress ratios (R=0.5, R=0, R=-1, and R= -2) and a wide range of stress levels (50 MPa to 225 MPa).

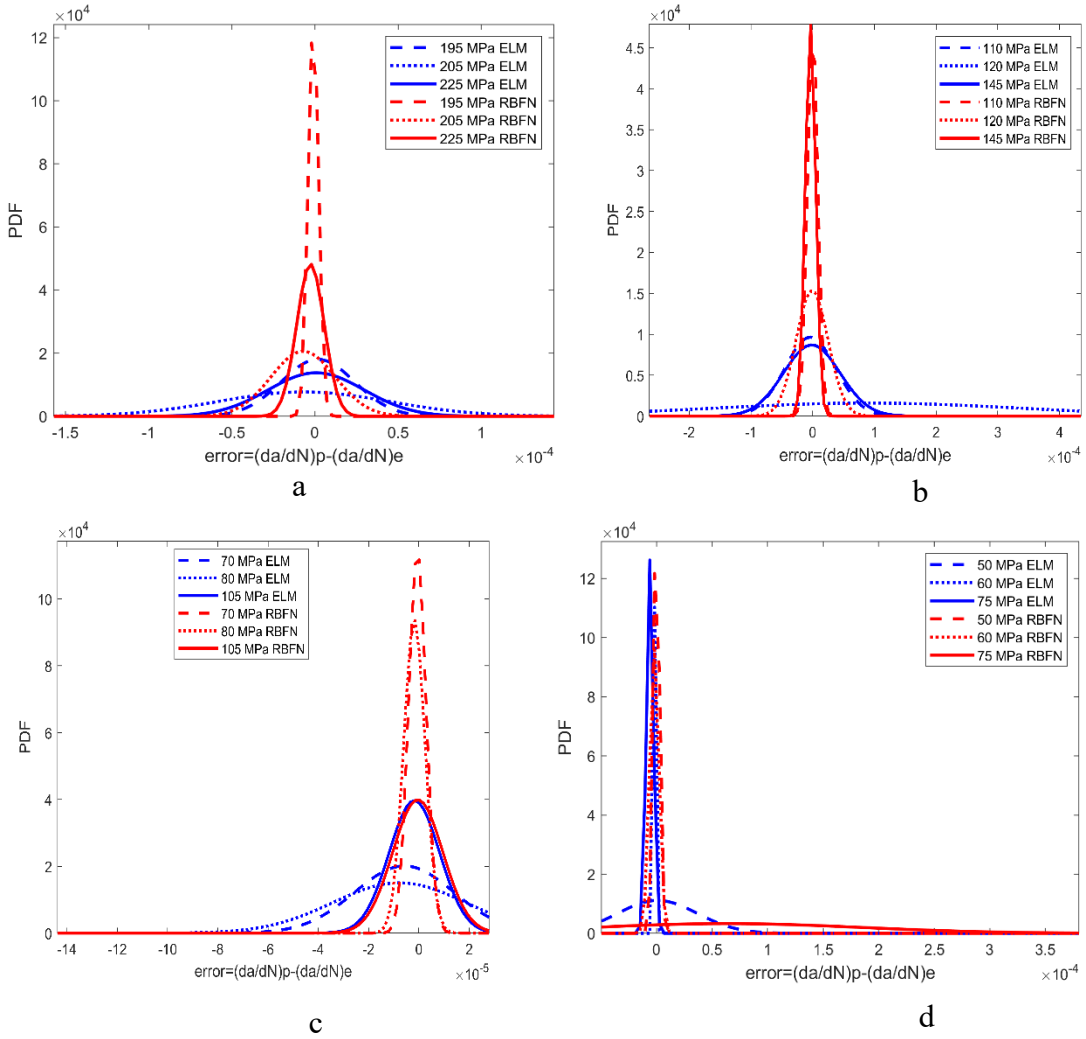

Figure 45 Probability density function of prediction errors for 2024-T3 aluminum alloy: (a) R=0.5; (b) R=0; (c) R=-1; and (d) R=-2

Figure 45 (a) shows the PDF curves for different stress levels (195 MPa, 205 MPa, 225 MPa) for each ANN method at R=0.5. For the stress level of 195 MPa represented by a dashed line, it can be seen that RBFN has less scatter compared to ELM. The area under the ELM curve is greater than that of the RBFN curve indicating that the probability of an error occurring is greater. For the next stress level of 205 MPa represented by a dotted line, it is noticed that both ELM and RBFN are not centered around zero but rather to its left, which means that they are underpredicting the FCG rate. However, the area under the RBFN curve is anew tighter and has a smaller distribution than that of ELM. As for the last stress level of 225 MPa shown as a strong line, it appears that the ELM curve is centered on zero, while RBFN curve center is slightly towards the left meaning that RBFN is underpredicting the FCG rate. Nonetheless, RBFN has slightly less scatter as opposed to ELM.

PDF curves for another set of stress levels (110 MPa, 120 MPa, 145 MPa) for each ANN method at R=0 is depicted in Figure 45 (b). The stress level 110 MPa is indicated by a dashed line, and it can be noticed that the PDF curve for RBFN has less scatter compared to that of RBFN. The dotted line presents the stress level 120 MPa and shows that the PDF curves for RBFN are superior to ELM as well. RBFN's curve is centered around zero and ELM's curve is off-centered. Hence, the ELM method is to some extent underpredicting the FCG rate. The solid line indicates the last stress level 145 MPa and shows that RBFN bell curve has less scatter of the prediction errors compared to ELM.

Figure 45 (c) depicts the PDF curves for three different stress levels (70 MPa, 80 MPa, 150 MPa) at R=-1 of each ANN method. For the stress level of 70 MPa shown by a dashed line, RBFN has less scatter compared to ELM and this latter is slightly

underpredicting the FCG rate. The stress level of 80 MPa represented by a dotted line shows that both PDF curves for RBFN is superior to ELM. The last stress level of 150 MPa represented as a strong line depicts that the ELM curve is centered on zero and has less scatter compared to RBFN but both methods are very similar.

Lastly, the PDF curves for R=-2 with three stress levels (50 MPa, 60 MPa, 75 MPa) are presented in Figure 45 (d). The first stress level of 50 MPa is represented by a dashed line and displays that RBFN has a tighter and less scattered bell curve compared to ELM. It can be noticed that the RBFN curve is not a smooth bell curve and that is due to the fact that there is not a sufficient number of data points for this stress level. The next stress level of 60 MPa curves show that both methods have small scatter with ELM being slightly superior. The final stress level of 75 MPa depicts that ELM's PDF curve has a smaller area and therefore is superior to RBFN.

The PDF allows the determination of statistical characteristics that are the mean and standard deviation also referred to as variance. The mean and standard deviation values for both methods derived from the previous PDF plots are shown in Table 7.

Table 7 Prediction error analysis of RBFN and ELM for 2024-T3 aluminum alloy

	R=0.5			R=0			R=-1		
2024-T3 Al	195 MPa	205 MPa	225MPa	110 MPa	120 MPa	145 MPa	70 MPa	80 MPa	105 MPa
Mean value μ_{ELM}	1.8e-06	-6.7e-06	7.3e-07	-3.8e-06	8.9e-05	-3.4e-06	-5.8e-06	-7.8e-06	-4.2e-07
Standard deviation σ_{ELM}	2.2e-05	5.2e-05	2.9e-05	4.1e-05	2.5e-05	8.3e-06	1.9e-05	2.6e-05	9.9e-06
Mean value μ_{RBFN}	-9.5e-07	-7.1e-06	-2.7e-06	1.8e-07	-8.9e-07	-1.3e-06	-6.1e-07	-1.9e-06	-1.8e-06
Standard deviation σ_{RBFN}	3.2e-06	1.9e-05	8.3e-06	8.3e-06	2.6e-05	4.6e-05	3.5e-06	4.3e-06	1.0e-05

	R=-2		
2024-T3 Al	50 MPa	60 MPa	75 MPa
Mean value μ_{ELM}	9.1e-07	-2.8e-07	-5.9-06
Standard deviation σ_{ELM}	3.6e-05	8.3e-07	3.2e-06
Mean value μ_{RBFN}	-9.7e-08	-1.9e-06	6.3e-05
Standard deviation σ_{RBFN}	2.8e-06	4.2e-06	0.00012

Table 7 shows an agreement with previous observations from the PDF plots, where the FCG predictions of the RBFN approach are superior to the ELM approach with the lower values of mean and standard deviation for S_{max}= 195 MPa, S_{max}= 205 MPa and S_{max}= 225 MPa at R=0.5 and for S_{max}= 70 MPa, S_{max}=80 MPa and S_{max}= 105 MPa at R=-

1 and for S_{max}= 50 and 60 MPa at R=-2. The FCG predictions of the ELM approach are superior to the RBFN approach with the lower values of mean and standard deviation for that for S_{max}= 75 MPa at R=-2.

Figure 46 shows the PDF for 2090-TBE41 aluminum-lithium alloy for three stress ratios (R=0, R=-1, and R= -2) and a wide range of stress levels (55 MPa to 170 MPa).

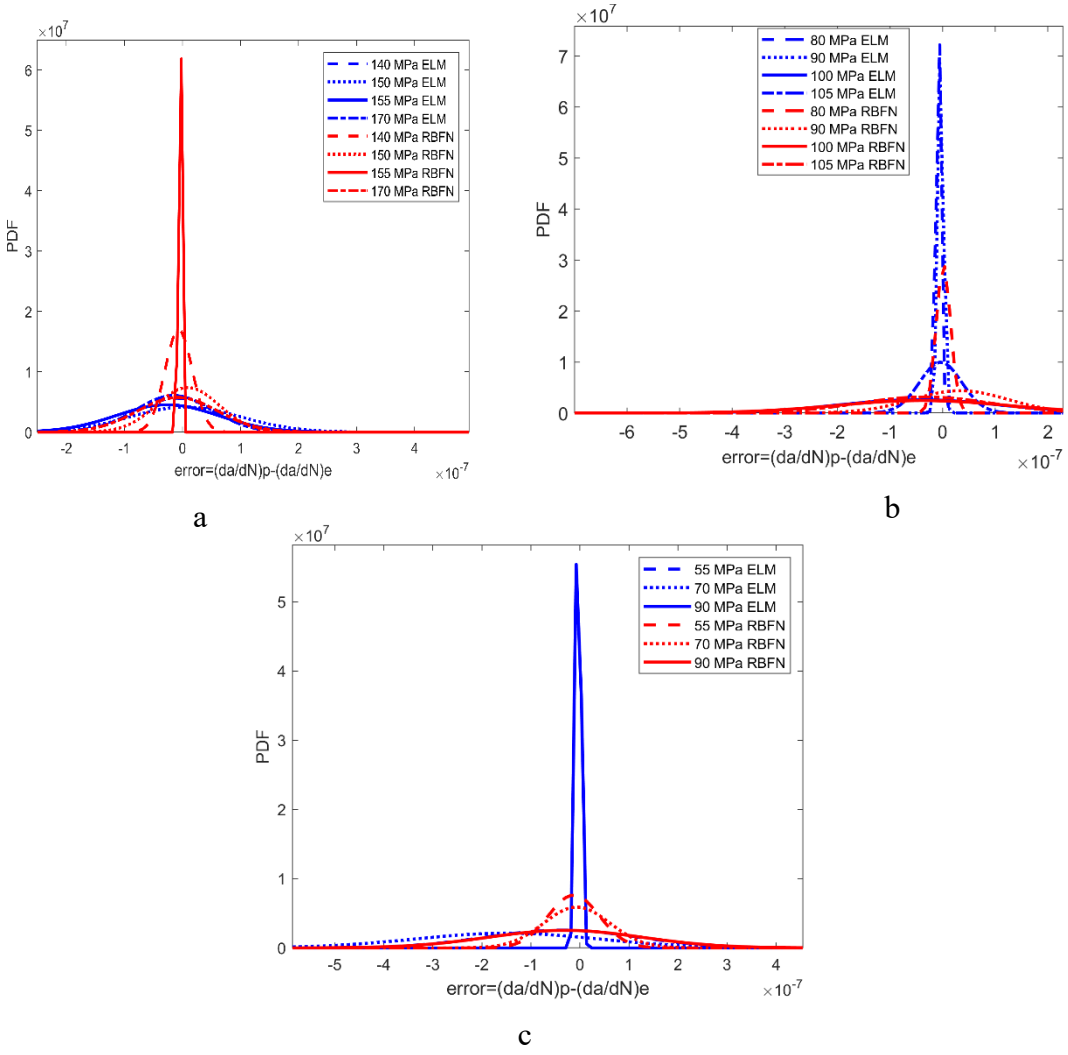

Figure 46 Probability density function of prediction errors for 2090-TBE41 aluminum-lithium alloy: (a) R=0; (b) R=-1; and (c) R=-2

Different PDF curves for numerous stress levels (140 MPa, 150 MPa, 155 MPa, and 170 MPa) at R=0 of each ANN method are presented in Figure 46 (a). For S_{max}= 140 MPa represented by a dashed line, RBFN has less scatter compared to ELM. The dotted line represents S_{max}= 150 MPa and shows that RBFN is producing better FCG rates. The RBFN PDF has less scatter compared to ELM for S_{max}=155 MPa shown by a strong line. Finally, for the last stress level of S_{max}= 170 MPa represented by a dash-dot line, RBFN and ELM are similar with RBFN being more centered towards zero and ELM being slightly to the left (i.e., ELM is underpredicting the FCG rate).

Figure 46 (b) shows different stress level PDF curves (80 MPa, 90 MPa, 100 MPa, 105 MPa) for each ANN method at R=-1. The ELM approach shows less scatter of prediction errors compared to RBFN for S_{max}= 80 MPa, S_{max}= 90 MPa, and S_{max}= 105 MPa represented by a dashed line, a dotted line, and a dash-dot line respectively. The PDF for the stress level of 100 MPa is indicating that both methods have similar largely distributed prediction errors.

Three different stress levels PDF curves (55 MPa, 70 MPa, 90 MPa) for each ANN method at R=-2 are presented in Figure 46 (c). The RBFN approach is superior to the ELM approach with a smaller scatter of the prediction errors for S_{max}= 55 MPa and S_{max}= 70 MPa. It can be seen that for this latter stress level, the ELM is not centered on zero but rather to the left which indicates that ELM is underpredicting. The last stress level of 90 MPa characterized by a strong line shows that the ELM is superior to the RBFN.

The mean and standard deviation values for both methods are listed in Table 8 below.

Table 8 Prediction error analysis of RBFN and ELM for 2090-TBE41 aluminum-lithium alloy

	R=0				R=-1				R=-2		
2090-TBE41 Al	140 MPa	150 MPa	155MPa	170 MPa	80 MPa	90 MPa	100 MPa	105 MPa	55 MPa	70 MPa	90 MPa
Mean value μ_{ELM}	-9.9e-09	5.0e-09	-2.6e-08	-1.0e08	-7.9e-09	-3.7e-09	-4.6e-08	-3.8e-09	-3.6e-08	-1.5e-07	-3.7e-09
Standard deviation σ_{ELM}	7.1e-08	9.6e-08	8.8e-08	6.6e-08	4.9e-09	5.5e-09	1.5e-07	4e-08	1.5e-07	1.9e-07	5.5e-09
Mean value μ_{RBFN}	-6.5e-09	9.1e-09	-4.9e-09	-8.2e-09	1.5e-09	3.3e-08	-3.9e-08	-3.3e-08	-1.3e-08	-6.4e-09	-3e-08
Standard deviation σ_{RBFN}	2.4e-08	5.4e-08	1.9e-09	6.95e-08	1.4e-08	9.1e-08	1.6e-07	1.3e-07	5.2e-08	6.7e-08	1.6e-07

Table 8 demonstrates that the FCG predictions of the RBFN approach are superior to the ELM approach with the lower values of mean and standard deviation at R=0, and for S_{max}= 55 MPa and S_{max}= 70 MPa at R=-2. The values of mean and standard deviation for R=-1 show that ELM approach is superior to RBFN for all stress levels: S_{max}= 80 MPa, S_{max}= 90 MPa, S_{max}= 100 MPa, and S_{max}= 105 MPa. These observations agree with the fitted probability density functions for the prediction errors.

The PDF for RBFN and ELM for LC9cs aluminum alloy for three stress ratios (R=0.5, R=0, and R= -1) with each two stress levels is displayed in Figure 47.

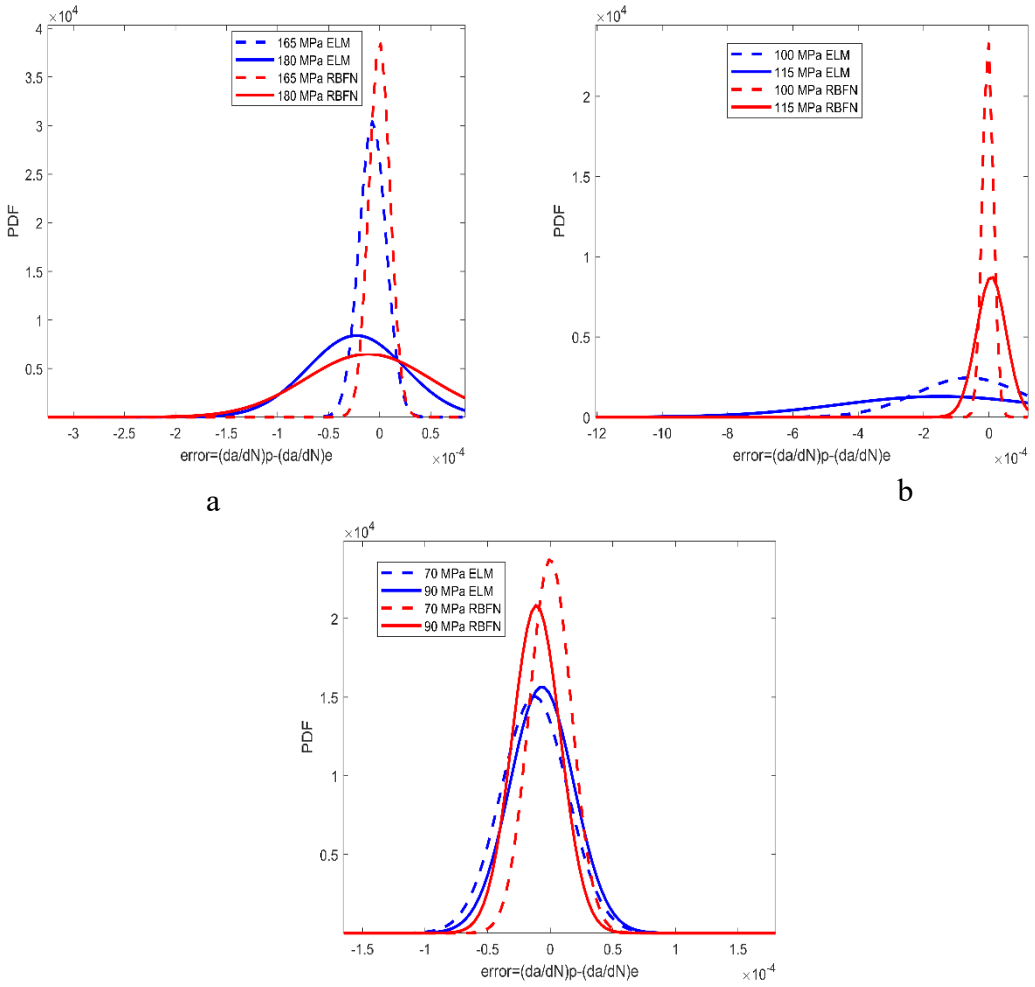

Figure 47 Probability density function of prediction errors for LC9cs aluminum alloy: (a) R=0.5; (b) R=0; and (c) R=-1

Figure 47 (a) presents two stress level PDFs (165 MPa and 180 MPa) for both RBFN and ELM methods at R=0.5. For the stress level of S_{max}= 165 MPa represented by dashed lines, RBFN has less scatter of the prediction errors compared to ELM. However, ELM curve is centered towards the left which means that the method is underpredicting the FCG rates. For the last stress level S_{max}= 180 MPa represented by solid lines, ELM is superior to RBFN with less scatter of the prediction error. Moreover, both methods are slightly underpredicting the FCG rate.

Figure 47 (b) shows two stress level PDF curves (100 MPa and 115 MPa) for each ANN method at R=0. The RBFN is superior to ELM with smaller scatter of prediction errors for both stress levels. Moreover, both methods are slightly underpredicting the FCG rates.

Lately, two stress levels PDF bell curves (70 MPa and 90 MPa) for each ANN method at R=-1 are presented in Figure 47 (c). The RBFN approach is superior to the ELM approach with a smaller scatter of the prediction errors.

Table 9 displays the mean and standard deviation values for both methods for LC9cs aluminum alloy.

Table 9 Prediction error analysis of RBFN and ELM for LC9cs aluminum alloy

	R=0.5		R=0		R=-1	
LC9cs Al	165 MPa	180MPa	100 MPa	115 MPa	70 MPa	90 MPa
Mean value μ_{ELM}	-6.8e-06	-2.3e-05	-6e-05	-1.5e-05	-1.3e-05	-6.6e-06
Standard deviation σ_{ELM}	1.3e-05	4.7e-05	1.e-05	3.1e-05	2.6e-05	2.5e-05
Mean value μ_{RBFN}	-7.3e-08	-1.1e-05	-3.5e-06	7.1e-06	5.4e-08	-1.1e-05
Standard deviation σ_{RBFN}	1e-05	6.1e-05	1.7e-05	4.5e-05	1.7e-05	1.9e-05

Table 9 demonstrates that the RBFN method is superior to the ELM approach with lower values of mean and standard deviation for S_{max}= 165 MPa at R=0.5, for S_{max}= 100 MPa and S_{max}= 115 MPa at R=0, as well as for S_{max}= 70 MPa and S_{max}= 90 MPa at R= -1. The values of mean and standard deviation for S_{max}= 180 MPa at R=0 show that ELM approach is superior to RBFN.

Figure 48 shows the PDFs for the prediction errors for both RBFN and ELM methods for 7075-T6 aluminum alloy for three stress ratios (R=0.5, R=0, and R= -1) and stress levels.

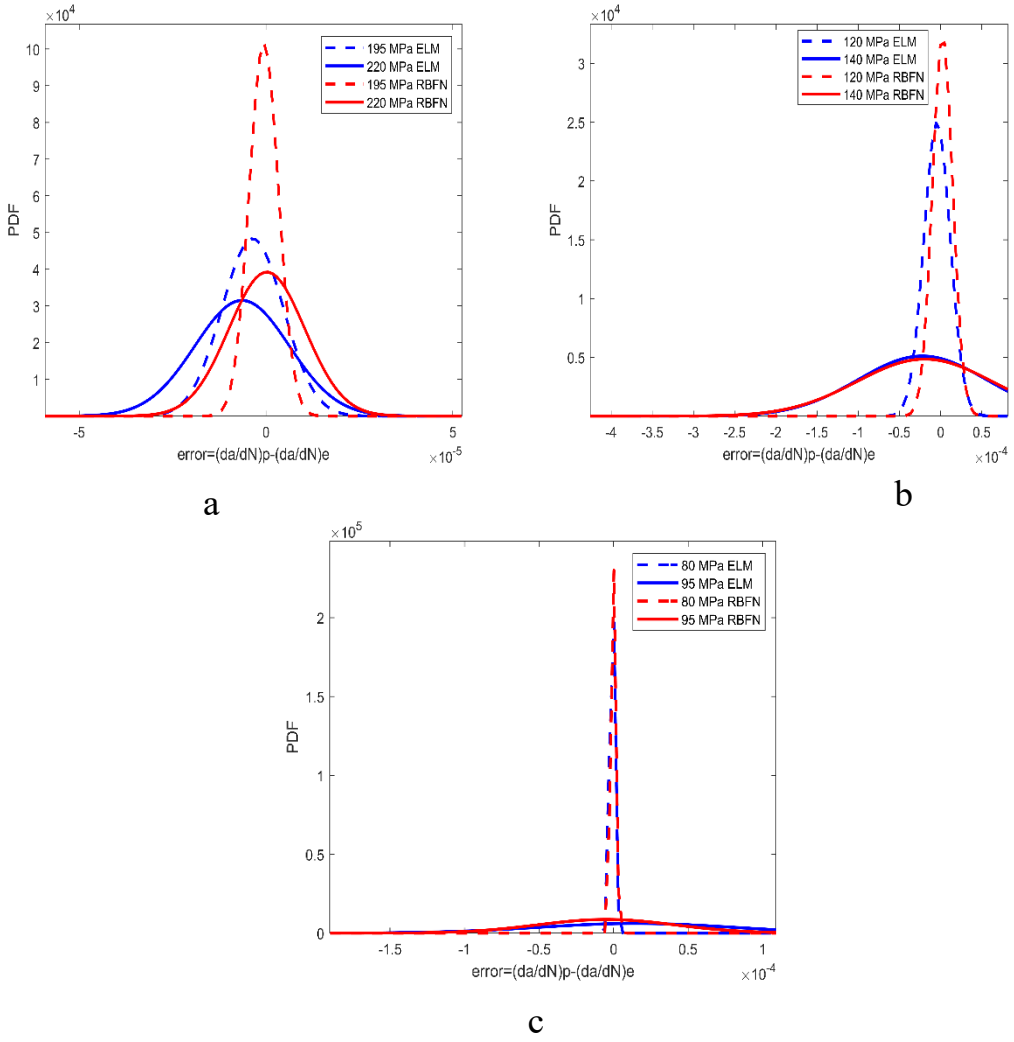

Figure 48 Probability density function of prediction errors for 7075-T6 aluminum alloy: (a) R=0.5; (b) R=0; and (c) R=-1

Two different stress level PDFs (195 MPa and 220 MPa) for both RBFN and ELM methods at R=0.5 are presented in Figure 48 (a). Both of S_{max}= 195 MPa and

S_{max}= 220 MPa reveal that RBFN has less scatter of the prediction errors compared to ELM.

Figure 48 (b) shows two stress level PDF curves (120 MPa, 140 MPa) for each ANN method for R=0. The ELM is superior to RBFN with smaller scatter of prediction errors for both S_{max}= 120 MPa and S_{max}= 140 MPa.

For the two stress levels PDF bell curves (80 MPa and 95 MPa) at R=-1 presented in Figure 48 (c), it can be seen that both methods are very similar.

Table 10 presents the mean and standard deviation values obtained from the PDF of prediction errors for both methods for 7075-T6 aluminum alloy.

Table 10 Prediction error analysis of RBFN and ELM for 7075-T6 aluminum alloy

	R=0.5		R=0		R=-1	
7075-T6 Al	195 MPa	220MPa	120 MPa	140 MPa	80 MPa	95 MPa
Mean value μ_{ELM}	-3.5e-06	-6.4e-06	-4.3e-06	-2.2e-05	-7.6e-07	1.5-05
Standard deviation σ_{ELM}	8.2e-06	1.3e-05	1.6e-05	7.8e-05	1.7e-06	6.5e-05
Mean value μ_{RBFN}	-5.7e-07	2.4e-07	2.4e-06	-1.9e-05	-2.1e-07	-4.9e-06
Standard deviation σ_{RBFN}	3.9e-06	1e-05	1.2e-05	8.2e-05	1.7e-06	4.6e-05

It can be noticeable from Table 10 that the RBFN method is superior to the ELM approach with lower values of mean and standard deviation for S_{max}= 195 MPa and S_{max}= 220 MPa at R=0.5, and S_{max}= 95 MPa at R=-1. The values of mean and standard deviation for S_{max}= 120 MPa and S_{max}= 140 MPa at R=0, and for S_{max}= 80 MPa at R=-1, show that ELM approach is superior to RBFN.

Figure 49 shows the PDFs for the prediction errors for the two selected methods (RBFN and ELM) of Ti-6Al-4V titanium alloy for two stress ratios (R=0.1 and R= -1) and different stress levels (210 MPa to 690 MPa).

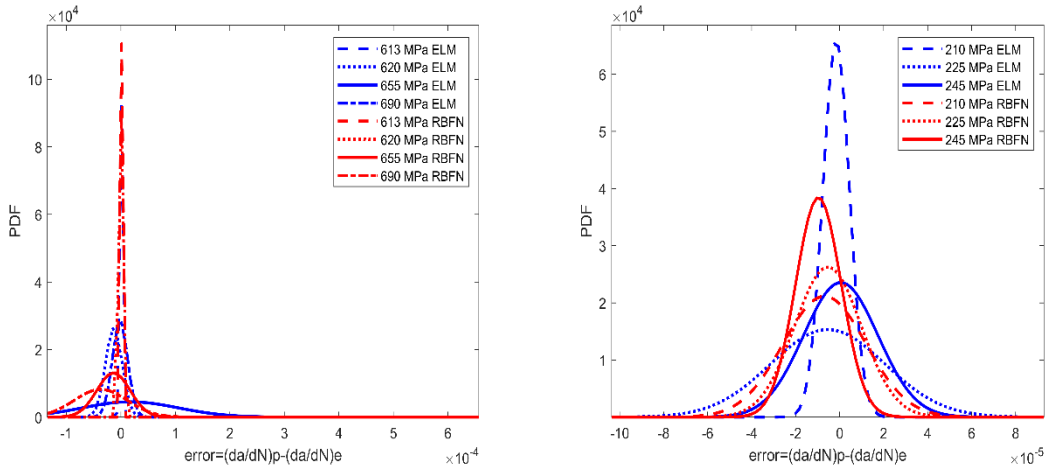

Figure 49 Probability density function of prediction errors for Ti-6Al-4V titanium alloy: (a) R=0.1; (b) R=-1

Stress level PDFs (613 MPa, 620 MPa, 655 MPa, 690 MPa) for both RBFN and ELM methods for R=0.1 are plotted in Figure 49 (a). The stress level of S_{max}= 613 MPa represented by dashed lines shows that ELM has less scatter of the prediction errors compared to RBFN. For the next stress level S_{max}= 620 MPa it can be seen that RBFN is superior to ELM. Lastly, for both stress levels S_{max}= 655 MPa and S_{max}= 690 MPa represented by a solid line and a dash-dotted line respectively shows that again RBFN is superior to ELM with less scatter of the prediction error.

Figure 49 (b) shows three different stress levels PDF bell curves (210 MPa, 225 MPa, 245 MPa) for each ANN method for R=-1. The ELM approach is superior to the RBFN approach for S_{max}= 210 MPa. The RBFN approach is superior to the ELM approach

for both S_{max}= 225 MPa and S_{max}= 245 MPa. However, it is noticed that ELM is slightly underpredicting the FCG rate.

Table 11 displays both the mean and standard deviation values attained from the PDF of prediction errors for both RBFN and ELM methods for Ti-6Al-4V titanium alloy.

Table 11 Prediction error analysis of RBFN and ELM for Ti-6Al-4V titanium alloy

	R=0.1				R=-1		
Ti-6Al-4V	613 MPa	620 MPa	655 MPa	690 MPa	210 MPa	225 MPa	245 MPa
Mean value μ_{ELM}	-1e-06	-1.3e-05	1.7e-05	-1.6e-06	-1.6e-06	-5.4e-06	5.1e-07
Standard deviation σ_{ELM}	1.7e-06	1.5e-05	8.8e-05	1.4e-05	6e-06	2.6e-05	1.7e-05
Mean value μ_{RBFN}	1.4e-08	-9.2e-08	-1e-05	-3.7e-05	-6.9e-06	-5.3e-06	-9.6e-06
Standard deviation σ_{RBFN}	7.1e-07	4.2e-06	3e-05	4.8e-05	1.9e-05	1.5e-05	1e-05

Table 11 shows that the RBFN method is superior to the ELM approach with lower values of mean and standard deviation for S_{max}= 620 MPa, S_{max}= 613 MPa, and S_{max}= 690 MPa at R=0.1, and S_{max}= 225 and 245 MPa at R=-1. Alternately, ELM approach is superior to RBFN with lower values of mean and standard deviation for S_{max}= 655 MPa, at R=0.1, and for S_{max}= 210 at R=-1.

To study the effect of the stress ratio on the prediction errors of the two ANN methods and draw a conclusion, the stress level PDF curves were combined for each stress ratio. This allows a more accurate comparison of the efficiency of each method. The PDF

curves of RBFN and ELM along with their corresponding mean and standard deviation values are compared based on the stress ratio R for all materials: 2024-T3, 7075-T6, 2090-TBE41, LC9cs aluminum, and Ti-6Al-4V titanium.

Figure 50 shows the 2024-T3 aluminum alloy PDFs for the prediction errors corresponding the stress ratio: R=0.5, R=0, R=-1, and R=-2. The PDFs are plotted for both the RBFN and ELM approaches represented by the blue color marker and the red color marker respectively.

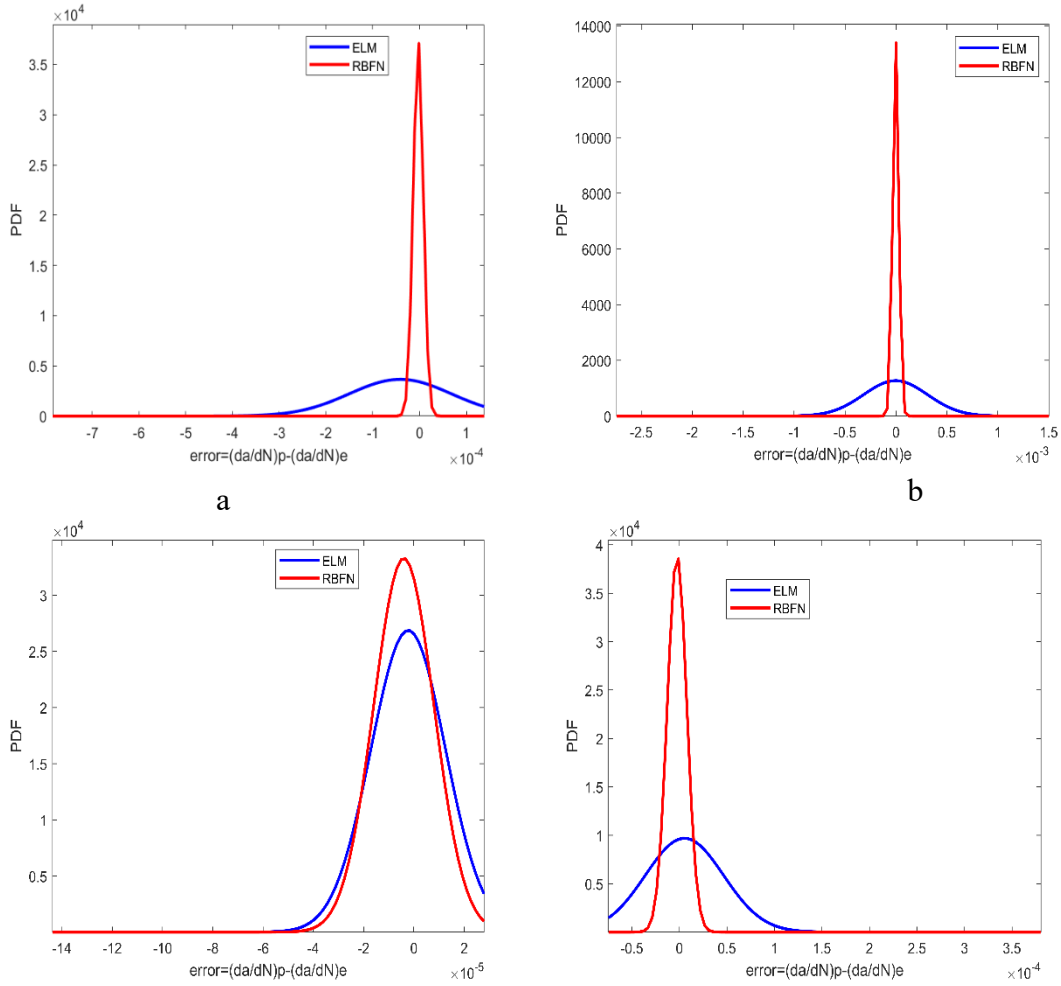

Figure 50 Probability density function of prediction errors of combined stress levels for 2024-T3 aluminum alloy: (a) R=0.5; (b) R=0; (c) R=-1; and (d) R=-2

Figure 50 (a) and Figure 50 (b) display similar PDF curves for both RBFN and ELM for R=0.5 and R=0 and combined stress levels. The RBFN approach is superior to the ELM approach with smaller scatter of the prediction errors. The ELM method is to some degree underpredicting the FCG rates. Both Figures 50 (c) and (d) show that the RBFN method surpasses the ELM method again in terms of smaller scatter of the prediction errors.

Table 12 summarizes the mean and standard deviation values for the 2024-T3 aluminum alloy for both RBFN and ELM approaches.

Table 12 Prediction error analysis of RBFN and ELM at different R-ratios for 2024-T3 aluminum alloy

	2024-T3 aluminum alloy			
	R=0.5	R=0	R=-1	R=-2
Mean value μ_{ELM}	-4.14e-05	-4.4e-06	-2.2e-06	5.3e-06
Standard deviation σ_{ELM}	1.2e-08	9.8e-08	1.5e-05	4.1e-05
Mean value μ_{RBFN}	-2.9e-06	-2.6e-06	-3.9e-06	-2.5e-06
Standard deviation σ_{RBFN}	1.1e-05	2.9e-05	1.2e-05	1e-05

In agreement with Figure 50 observations, Table 12 shows that RBFN is superior to ELM with lower values of standard deviation for all R ratios. ELM has lower mean values than RBFN which means that this last is underpredicting the FCG rates.

The PDFs of the prediction errors for 2090-TBE41 aluminum-lithium alloy of three stress ratios (R=0, R=-1, and R= -2) and the two ANN methods is shown in Figure 51.

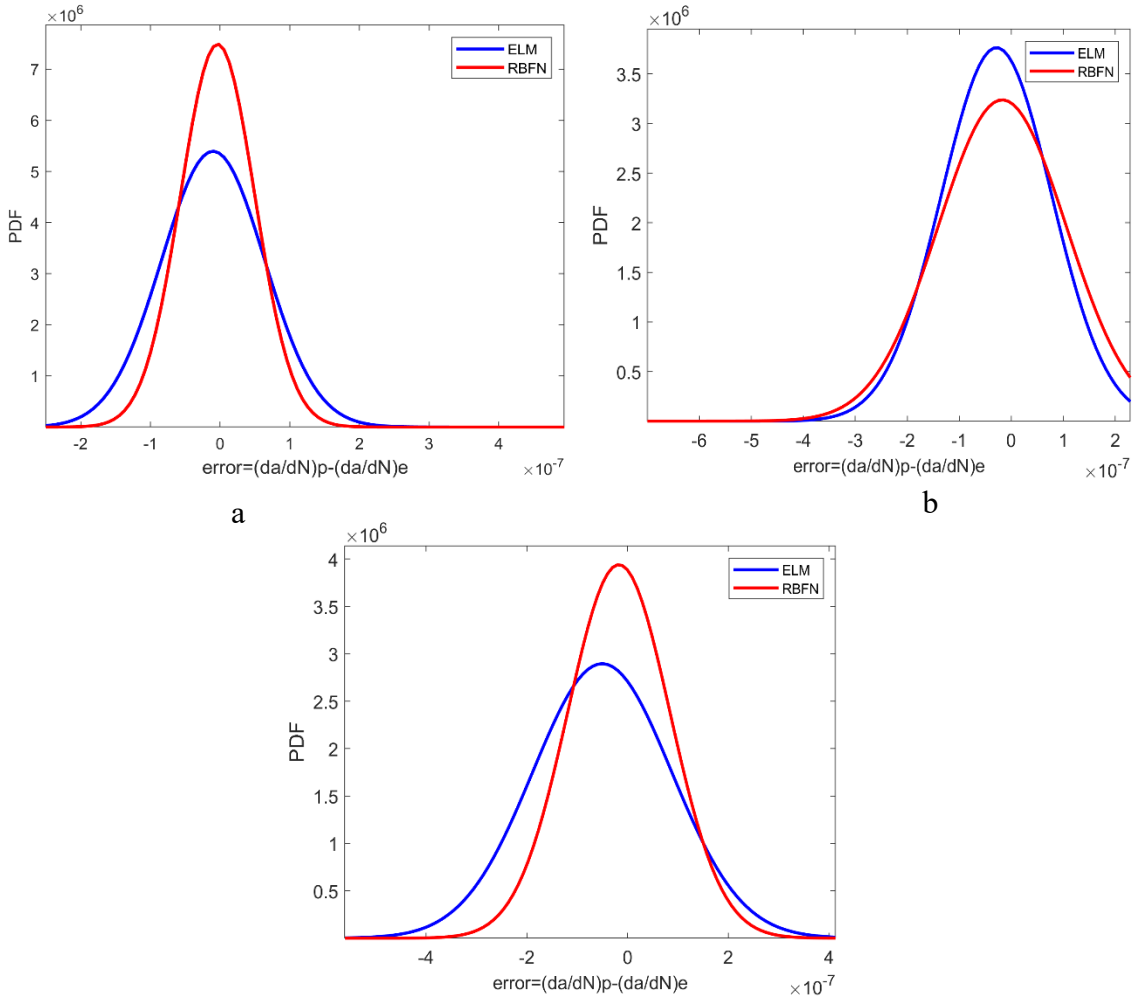

Figure 51 Probability density function of prediction errors of combined stress levels for 2090-TBE41 aluminum-lithium alloy: (a) R=0; (b) R=-1; and (c) R=-2

Figure 51 (a) and Figure 51 (c) shows that the RBFN approach is superior to the ELM approach with smaller scatter of the prediction errors. Both methods are to some degree underpredicting the FCG rates. Figures 51 (b) shows that the ELM method is superior to the RBFN with lesser scatter of the prediction errors. It is observed that ELM is slightly underpredicting the FCG rates.

Table 13 is recapitulation of the mean and standard deviation values for 2090-TBE41 aluminum-lithium alloy for both RBFN and ELM and different stress ratios (R=0, R=-1, and R=- 2).

Table 13 Prediction error analysis of RBFN and ELM at different R-ratios for 2090-TBE41 aluminum-lithium alloy

	2090-TBE41 aluminum-lithium alloy		
	R=0	R=-1	R=-2
Mean value μ_{ELM}	-1.0e-08	-2.8e-08	-5.0e-08
Standard deviation σ_{ELM}	7.4e-08	1.1e-07	1.4e-07
Mean value μ_{RBFN}	-3.6e-09	-1.7e-08	-1.7e-08
Standard deviation σ_{RBFN}	5.3e-08	1.2e-07	1e-07

Table 13 shows that RBFN is superior to ELM with lower values of standard deviation at R=0 and R=-2. For R=0.5, the ELM method is superior to the RBFN method with lower mean and standard deviation values.

Figure 52 presents the PDFs of the prediction errors for LC9cs aluminum alloy for the two methods: RBFN and ELM, at three stress ratios (R=0.5, R=0, and R=- 1).

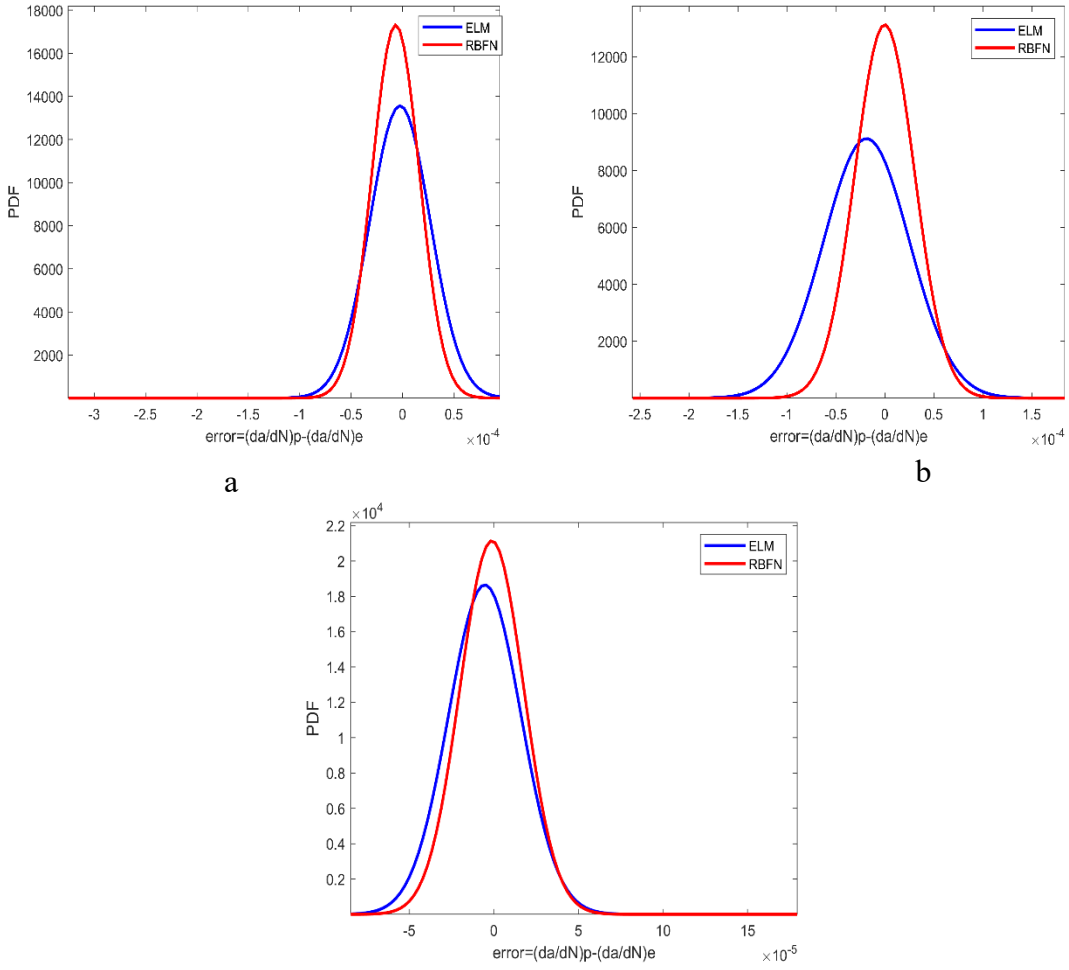

Figure 52 Probability density function of prediction errors of combined stress levels for LC9cs aluminum alloy: (a) R=0.5; (b) R=0; and (c) R=-1

Figure 52 shows the RBFN approach is superior to the ELM approach with smaller scatter of the prediction errors at all R ratios.

Table 14 shows the mean and standard deviation values derived from the PDF plots for LC9cs aluminum alloy for both RBFN and ELM and different stress ratios.

Table 14 Prediction error analysis of RBFN and ELM at different R-ratios for LC9cs aluminum alloy

	LC9cs aluminum alloy		
	R=0.5	R=0	R=-1
Mean value μ_{ELM}	-2.3e-06	-1.9e-05	-5.4e-06
Standard deviation σ_{ELM}	2.9e-05	1.9e-09	2.1e-05
Mean value μ_{RBFN}	-6.6e-06	-9.1e-08	-1.2e-06
Standard deviation σ_{RBFN}	2.3e-05	9.2e-10	1.8e-05

Table 14 illustrates furthermore that RBFN is superior to ELM at R=0.5, R=0, and R=-1 with lower values of standard deviation.

The PDFs of the prediction errors for 7075-T6 aluminum alloy for both the RBFN and ELM approaches at R=0.5, R=0, and R=- 1 are shown in Figure 53.

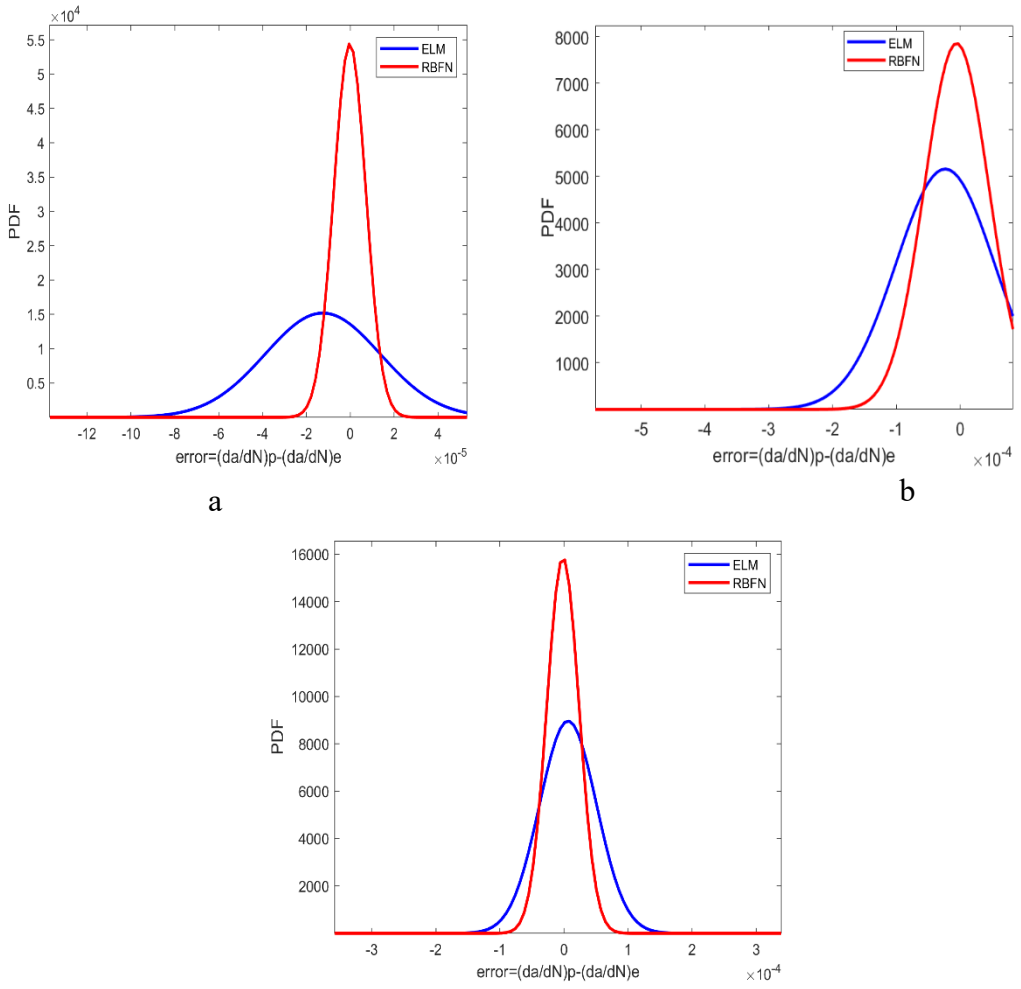

Figure 53 Probability density function of prediction errors of combined stress levels for 7075-T6 aluminum alloy: (a) R=0.5; (b) R=0; and (c) R=-1

Figure 53 shows that the RBFN approach is superior to the ELM approach with smaller scatter of the prediction errors at R=0, R=0.5 and R=- 1.

Table 15 displays the mean and standard deviation values for 7075-T6 aluminum alloy for both RBFN and ELM and three different stress ratios.

Table 15 Prediction error analysis of RBFN and ELM at different R-ratios for 7075-T6 aluminum alloy

	7075-T6 aluminum alloy		
	R=0.5	R=0	R=-1
Mean value μ_{ELM}	6.3e-12	-2.3e-05	6.3e-06
Standard deviation σ_{ELM}	5.2e-28	7.7e-05	4.4e-05
Mean value μ_{RBFN}	-2.1e-07	-5.4e-06	-1.6e-06
Standard deviation σ_{RBFN}	7.3e-06	5.1e-05	2.5e-05

It can be noted from Table 15 that RBFN is superior to ELM with lower values of mean and standard deviation values at R=0.5, R=0 and R=- 1.

Figure 54 displays the PDF curves of the prediction errors for Ti-6Al-4V titanium alloy for the RBFN and ELM methods at R=0.1 and R=- 1.

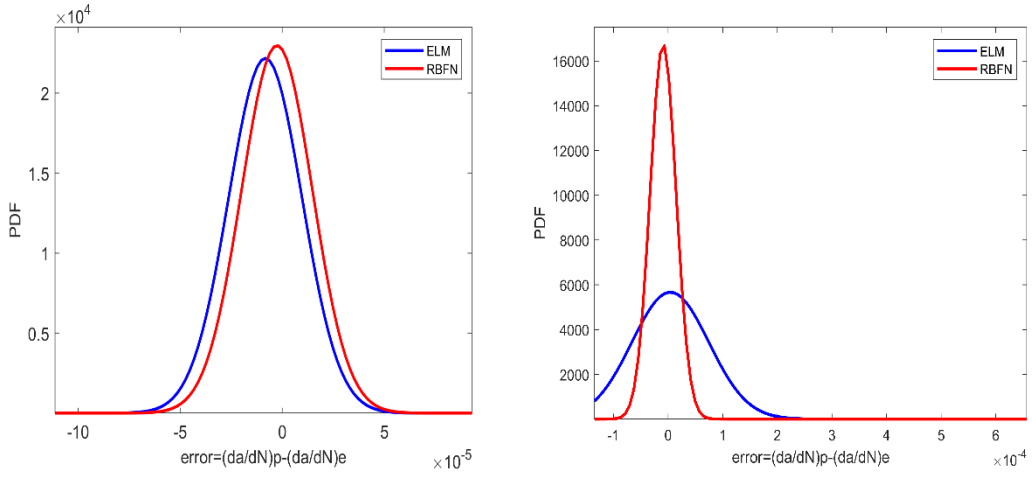

a b

Figure 54 Probability density function of prediction errors of combined stress levels for Ti-6Al-4V titanium alloy: (a) R=0.1; (b) R=-1

Figure 54 (a) displays that for R=0.1 the RBFN approach is superior to the ELM approach with smaller scatter of the prediction errors. Both methods are however similar. For R=-1 presented in Figure 54 (b), the PDF curves show that the RBFN has less scatter of the prediction errors than ELM.

Lastly, Table 16 exhibits the mean and standard deviation values for Ti-6Al-4V titanium alloy for both RBFN and ELM and two stress ratios: R=0.1 and R=-1.

Table 16 Prediction error analysis of RBFN and ELM at different R-ratios for Ti-6Al-4V titanium alloy

	Ti-6Al-4V titanium alloy	
	R=0.1	R=-1
Mean value μ_{ELM}	-2.6e-06	4.1e-06
Standard deviation σ_{ELM}	1.7e-05	7.1e-05
Mean value μ_{RBFN}	-8.3e-06	-9.2e-06
Standard deviation σ_{RBFN}	1.8e-05	2.4e-05

Table 16 shows that RBFN has fewer prediction errors than ELM for R=-1 based on the lower values of mean and standard deviation. For R=0.1, it can be seen that both methods have similar mean and standard deviation values, which agrees with Figure 54 (b) observations. However, the RBFN approach is superior to the ELM approach.

It can be noticed from the error analysis above that both methods seem to predict the small crack FCG rate well. Another observation is that RBFN is in most cases superior to ELM with less scatter of the prediction errors and lower mean and standard deviation values for compressive loads. According to Newman and Edwards [9] and Zocher [50],

small cracks behavior have been more dominant in compressive loads tests. The RBFN method could be a more suitable method to study the FCG rate at negative R-ratios.

CHAPTER VI

CONCLUSIONS AND FUTUTRE RECOMMENDATRIONS

Conclusions

Fatigue crack growth modeling was performed based on two kinds of artificial neural networks: extreme learning machine (ELM) and radial basis function network (RBFN). The objective of this study was to use both ANNs to validate their use to predict fatigue crack growth rate of small cracks for different materials and compare their performance.

The same neural network parameters were used for both RBFN and ELM. The neural network methods were validated using fatigue crack growth data sets for five different given materials: 2024-T3 aluminum alloy, 2090-TBE41 aluminum-lithium alloy, LC9cs aluminum alloy, 7075-T6 aluminum alloy, Ti-6Al-4V titanium alloy.

Based on all the findings in this work, the most important conclusions are summarized as follow:

- The novel ANN models provide accurate FCG rates predictions for a number of different materials beyond the range of the original R-ratios and completely address the small fatigue behavior.

- The results showed that both ANNs can fit the experimental data accurately. Both models show high performance for predicting the fatigue crack growth

rates for different R ratios and beyond the given stress intensity range as shown in the 3D prediction surfaces.

- By comparing the 2D and 3D plots for both methods, ELM and RBFN provide fairly similar results with minor deviations.

- Based on the predicted FCG rates and the error analysis, RBFN method performs better by fitting more accurately with the training set of the experimental data for most materials, especially under compressive loading. Thus, it shows excellent global optimization and extrapolation ability.

- When training data is sufficient, both RBFN and ELM methods predict the experimental data very well. When fewer data are available, RBFN matches the experimental data best and extrapolate beyond the given range.

- The MSEs of RBFN and ELM indicates that both methods can predict the experimental data very well, and RBFN is superior to ELM.

- The use of ANNs as effective methods to predict small crack behavior of different materials based on one model was validated.

- This study demonstrates that although the ANN methods provide excellent results, the performance of these methods still depends on the sufficiency of

the experimental data as the results were better for materials where there was a higher data density. However, when dealing with limited fatigue crack growth data, RBFN remains the best method.

- The efficiency of ANNs is not affected by materials and the same parameters can be used for all materials.

Summary of Contributions

The small crack modeling has always been a challenging issue in the fatigue and fracture mechanics community due to the complex behavior of small cracks. The current study showed that it is feasible to apply ANNs to describe the complex behavior of small cracks without being limited by material parameters such is the case for some classical fracture mechanics methods. ANNs can be applied to different materials and can extrapolate beyond the R-ratios ranges which will lessen the cost and time constraints of fatigue crack growth simulations and experiments. Based on the presented results, RBFN remains the best method used for fatigue crack growth calculation. However, ELM is more convenient because of the fewer parameters that need to be tuned contrary to RBFN that has more parameters which make it harder to find out the ideal combination.

The major contribution of this thesis is the development of ANNs as a potential modeling approach for fatigue crack growth predictions which will be helpful for several applications. The current study shows that the ANN-based approaches correlate well with experimental data. However, the performance of these methods highly depends on the sufficiency of the experimental data.

Recommendations for Future Work

The proposed ANNs were shown to be favorable and sophisticated methods to predict FCG rate for small cracks. Both methods however have some limitations in terms of insufficient experimental data that need further investigation since accurate predictions are strongly related to the size of the training data. This is a promising solution to address one of the most complex problems in the Fatigue and Fracture community that is the small crack problem. There might be a need of conducting more experiments to store data and make them available for researchers.

CHAPTER VII

REFERENCES

[1] Homeland Security: Science and Technology, “Aging Infrastructure: Issues, Research, and Technology,” *Build. Infrastruct. Prot. Ser.*, vol. 1, no. December, 2010.

[2] A. I. R. Transportation and S. Issue, *Raising the Bar on Safety : Reducing the Risks Associated with Air-taxi Operations in Canada*, no. November. 2019.

[3] S. Suresh and R. O. Ritchie, “Propagation of short fatigue cracks,” *Int. Met. Rev.*, vol. 29, no. 1, pp. 445–473, 1984.

[4] S. Ahn and M. B. Mendel, “A Fatigue Life Model For Crack Propagation Under A Variable Amplitude Load,” vol. 22, no. I, 1994.

[5] H. J. C. Voorwald, M. A. S. Torres, and C. C. E. Pinto Júnior, “Modelling of fatigue crack growth following overloads,” *Int. J. Fatigue*, vol. 13, no. 5, pp. 423–427, 1991.

[6] J. C. Newman, “Fatigue and crack-growth analyses under Giga-cycle loading on aluminum alloys,” *Procedia Eng.*, vol. 101, no. C, pp. 339–346, 2015.

[7] K. Hussain, “Short fatigue crack behaviour and analytical models: A review,” *Eng. Fract. Mech.*, vol. 58, no. 4, pp. 327–354, 1997.

[8] J. J.C.Newman, X.R.Wu, S. L. Venneri, and C.G.Li, “Small-Crack Effects in High-Strength Aluminum Alloys,” 1994.

[9] J. J.C.Newman and P.R.Edwards, “Short-Crack Growth Nehaviour in an Aluminum Alloy-an AGARD Cooperative Test Programme (AGARD Report No.732),” 1988.

[10] J. C. Newman, “a Review of Modelling Small-Crack Behavior and Fatigue-Life Predictions for Aluminum Alloys,” *Fatigue Fract. Eng. Mater. Struct.*, vol. 17, no. 4, pp. 429–439, 1994.

[11] K. Wang, F. Wang, W. Cui, T. Hayat, and B. Ahmad, “Prediction of short fatigue crack growth of Ti-6Al-4V,” *Fatigue Fract. Eng. Mater. Struct.*, vol. 37, no. 10, pp. 1075–1086, 2014.

[12] C. Kaynak, A. Ankara, and T. J. Baker, “A comparison of short and long fatigue crack growth in steel,” *Int. J. Fatigue*, vol. 18, no. 1, pp. 17–23, 1996.

[13] K. Tokaji, T. Ogawa, Y. Harada, and Z. Ando, “Limitations of Linear Elastic Fracture Mechanics in Respect of Small Fatigue Cracks and Microstructure,” *Fatigue Fract. Eng. Mater. Struct.*, vol. 9, no. 1, pp. 1–14, 1986.

[14] L. Edwards and Y. H. Zhang, “Investigation of small fatigue cracks-I. Plastic deformation associated with small fatigue cracks,” *Acta Metall. Mater.*, vol. 42, no. 4, pp. 1413–1421, 1994.

[15] J. Lankford, “The growth of small fatigue cracks in 7975-T6 Aluminum,” *Fatigue Eng. Mater. Struct.*, vol. 5, 1982.

[16] J. C. Newman, “Small-Crack Alloys Effects in High-Strength Aluminum Cooperative,” *Spectrum*, no. May, 1994.

[17] R. O. Ritchie and J. Lankford, “Small fatigue cracks: A statement of the problem and potential solutions,” *Mater. Sci. Eng.*, vol. 84, no. C, pp. 11–16, 1986.

[18] ELBER W, “the Significance of Fatigue Crack Closure,” *ASTM Spec. Tech. Publ.*, pp. 230–242, 1971.

[19] J. C. Newman, E. P. Phillips, and M. H. Swain, “Fatigue-life prediction methodology using small-crack theory,” *Int. J. Fatigue*, vol. 21, no. 2, pp. 109–119, 1999.

[20] R. Pippan and A. Hohenwarter, “Fatigue crack closure: a review of the physical phenomena,” *Fatigue Fract. Eng. Mater. Struct.*, vol. 40, no. 4, pp. 471–495, 2017.

[21] S. Suresh, G. F. Zamiski, and D. R. O. Ritchie, “Oxide-Induced Crack Closure: An Explanation for Near-Threshold Corrosion Fatigue Crack Growth Behavior,” *Metall. Trans. A*, vol. 12, no. 8, pp. 1435–1443, 1981.

[22] J. C. Newman, “A crack opening stress equation for fatigue crack growth,” *Int. J. Fract.*, vol. 24, no. 4, pp. 131–135, 1984.

[23] M.H.Swain, R.A.Everett, and J. J.C.Newman, “The growth of short cracks in 4340 steel and aluminum-lithium 2090,” *AGARD Suppl. Test Progr.*, no. June, 2015.

[24] J. C. Newman and Y. Yamada, “Compression precracking methods to generate near-threshold fatigue-crack-growth-rate data,” *Int. J. Fatigue*, vol. 32, no. 6, pp. 879–885, 2010.

[25] T. C. Lindley and C. E. Richards, “The relevance of crack closure to fatigue crack propagation,” *Mater. Sci. Eng.*, vol. 14, no. 3, pp. 281–293, 1974.

[26] K. Sadananda, M. Nani Babu, and A. K. Vasudevan, “A review of fatigue crack growth resistance in the short crack growth regime,” *Mater. Sci. Eng. A*, vol. 754, no. November 2018, pp. 674–701, 2019.

[27] A. K. Vasudeven, K. Sadananda, and N. Louat, “A review of crack closure, fatigue crack threshold and related phenomena,” *Mater. Sci. Eng. A*, vol. 188, no. 1–2, pp. 1–22, 1994.

[28] A. J. McEvily and K. Minakawa, “On Crack Closure in Fatigue Crack Growth,” pp. 763–768, 1984.

[29] M. H. El Haddad, N. E. Dowling, T. H. Topper, and K. N. Smith, “J integral applications for short fatigue cracks at notches,” *Int. J. Fract.*, vol. 16, no. 1, pp.

15–30, 1980.

[30] A. J. MCEVILY, “the Growth of Short Fatigue Cracks,” *J. Soc. Mater. Sci. Japan*, vol. 47, no. 3Appendix, pp. 3–11, 1998.

[31] D. J. Bang, A. Ince, and M. Noban, “Modeling approach for a unified crack growth model in short and long fatigue crack regimes,” *Int. J. Fatigue*, vol. 128, no. November 2018, p. 105182, 2019.

[32] D. J. Bang, A. Ince, and L. Q. Tang, “A modification of UniGrow 2-parameter driving force model for short fatigue crack growth,” *Fatigue Fract. Eng. Mater. Struct.*, vol. 42, no. 1, pp. 45–60, 2019.

[33] J. Newman, J. Schneider, A. Daniel, and D. McKnight, “Compression pre-cracking to generate near threshold fatigue-crack-growth rates in two aluminum alloys,” *Int. J. Fatigue*, vol. 27, no. 10–12, pp. 1432–1440, 2005.

[34] S. Baraha and P. K. Biswal, “Implementation of activation functions for ELM based classifiers,” *Proc. 2017 Int. Conf. Wirel. Commun. Signal Process. Networking, WiSPNET 2017*, vol. 2018-Janua, no. August 2018, pp. 1038–1042, 2018.

[35] J. R. Mohanty, B. B. Verma, D. R. K. Parhi, and P. K. Ray, “Application of artificial neural network for predicting fatigue crack propagation life of aluminum alloys,” *Arch. Comput. Mater. Sci. Surf. Eng.*, vol. 1, no. 3, pp. 133–138, 2009.

[36] J. A. Rodríguez, Y. El Hamzaoui, J. A. Hernández, J. C. García, J. E. Flores, and A. L. Tejeda, “The use of artificial neural network (ANN) for modeling the useful life of the failure assessment in blades of steam turbines,” *Eng. Fail. Anal.*, vol. 35, pp. 562–575, 2013.

[37] M. Fahad, K. Kamal, T. Zafar, R. Qayyum, S. Tariq, and K. Khan, “Corrosion detection in industrial pipes using guided acoustics and radial basis function neural network,” *2017 Int. Conf. Robot. Autom. Sci. ICRAS 2017*, pp. 129–133, 2017.

[38] J. R. Mohanty, T. K. Mahanta, A. Mohanty, and D. N. Thatoi, “Prediction of constant amplitude fatigue crack growth life of 2024 T3 Al alloy with R-ratio effect by GP,” *Appl. Soft Comput. J.*, vol. 26, pp. 428–434, 2015.

[39] W. Zhang, Z. Bao, S. Jiang, and J. He, “An artificial neural network-based algorithm for evaluation of fatigue crack propagation considering nonlinear damage accumulation,” *Materials (Basel).*, vol. 9, no. 6, 2016.

[40] H. Wang, W. Zhang, F. Sun, and W. Zhang, “A comparison study of machine learning based algorithms for fatigue crack growth calculation,” *Materials (Basel).*, vol. 10, no. 5, 2017.

[41] H. Bin Younis, K. Kamal, M. F. Sheikh, A. Hamza, and T. Zafar, “Prediction of fatigue crack growth rate in aircraft aluminum alloys using radial basis function neural network,” *Proc. - 2018 10th Int. Conf. Adv. Comput. Intell. ICACI 2018*, pp. 825–830, 2018.

[42] S. N. S. Mortazavi and A. Ince, “An artificial neural network modeling approach for short and long fatigue crack propagation,” *Comput. Mater. Sci.*, vol. 185, no. June, p. 109962, 2020.

[43] P. R. . Edwards and J. C. Newman, “Short Crack Behavior in Various Aircraft Materials (AGARD-R-767).”

[44] O. I. Abiodun, A. Jantan, A. E. Omolara, K. V. Dada, N. A. E. Mohamed, and H. Arshad, “State-of-the-art in artificial neural network applications: A survey,” *Heliyon*, vol. 4, no. 11, p. e00938, 2018.

[45] P. G. Zhang, “Data Mining and Knowledge Discovery Handbook,” *Data Min. Knowl. Discov. Handb.*, no. June, 2010.

[46] T. Poggio and F. Girosi, “Network for Approximation and Learning,” *Proc. {IEEE}*, vol. 78, no. 9, pp. 1481–1497, 1990.

[47] R. J. Craddoc and K. Warwick, “Multi-layer radial basis function networks. An extension to the radial basis function,” *IEEE Int. Conf. Neural Networks - Conf. Proc.*, vol. 2, pp. 700–705, 1996.

[48] G. Bin Huang, Q. Y. Zhu, and C. K. Siew, “Extreme learning machine: A new learning scheme of feedforward neural networks,” *IEEE Int. Conf. Neural Networks - Conf. Proc.*, vol. 2, pp. 985–990, 2004.

[49] G. Bin Huang, Q. Y. Zhu, and C. K. Siew, “Extreme learning machine: Theory and applications,” *Neurocomputing*, vol. 70, no. 1–3, pp. 489–501, 2006.

[50] Z. H, “Behaviour of Short Cracks in Airframe Components,” in *AGARD CONFERENCE PROCEEDINGS No. 328*, 1983.